Diplomarbeit

Low Energy Ion Scattering (LEIS):
Basic Theory and Practical Application

ausgeführt zum Zwecke der Erlangung des akademischen Grades eines
Diplom-Ingenieurs

unter der Anleitung von

Univ.Prof. Dr.rer.nat. Günther Rupprechter

Univ.Ass. Dr.rer.nat. Christoph Rameshan

Institut für Materialchemie E165

eingereicht an der Technischen Universität Wien

Fakultät für Technische Chemie

von

Thomas HAUNOLD, BSc

Matrikelnummer: 00525527

Trubelgasse 16/7, 1030 Wien

Wien, am 07.11.2017   Unterschrift (Student):

Für Isabella, Walter, Janette und Sylke

Eidesstattliche Erklärung

Ich erkläre hiermit an Eides statt, dass ich die vorliegende Diplomarbeit selbstständig und ohne fremde Hilfe verfasst habe, andere als die angegebenen Quellen und Hilfsmittel nicht benutzt und die verwendeten Quellen wörtlich und inhaltlich als solche erkenntlich gemacht habe.

Statutory declaration

I declare herewith that I have authored the present master thesis independently, that I have not used other than the declared sources and resources, and that I have explicitly marked all material which has been quoted either literally or by content from the used sources.

Acknowledgements

Kurzfassung

Im Rahmen der vorliegenden Arbeit werden zunächst theoretische Aspekte zur Streuung niederenergetischer Ionen (*Low Energy Ion Scattering*, LEIS) anhand eines Billard-Spiels präsentiert. Dabei sollen die vermittelten Grundlagen die Interpretation von aufgenommenen Spektren für Anwender erleichtern und die besondere Oberflächenempfindlichkeit der Methode aufzeigen. Das Hauptaugenmerk liegt auf der Bestimmung der chemischen Zusammensetzung der obersten atomaren Lage fester Oberflächen, insbesondere jener von metallischen Legierungen oder intermetallischen Phasen, die als Substrat für die Herstellung von Modellkatalysatoren eingesetzt werden. Der Erhalt der chemischen und strukturellen Beschaffenheit der obersten atomaren Lage während einer Analyse ist eine große Herausforderung. Die Streuung niederenergetischer He^+-Ionen ermöglicht jedoch eine weitgehend zerstörungsfreie und zugleich hochempfindliche Messung, was diese Methode in der Oberflächenanalytik einzigartig macht.

Gegenstand der praktischen Anwendung war ein $Pt_3Zr(0001)$-Einkristall, der die Möglichkeit bietet, einen ultradünnen ZrO_2-Film aufwachsen zu lassen – ein Material, das zur Zeit von großem Interesse ist, vor allem in Forschungsbereichen, die sich mit der Festoxidbrennstoffzelle (*Solid Oxide Fuel Cell*, SOFC) und ihren katalytischen Eigenschaften auseinandersetzen. Die Herstellung dieses Oxidfilms durch Abscheiden von Zr im UHV mit Hilfe von herkömmlichen Methoden (z.B. Elektronenstoßverdampfung) wird dadurch erschwert, dass Zr einen hohen Schmelzpunkt aufweist und die Schmelze über einen niedrigen Dampfdruck verfügt. In der Literatur wird jedoch davon berichtet, dass der niedrige Zr-Gehalt der Pt_3Zr-Legierung unter erhöhten Temperaturen aus den obersten atomaren Lagen freigesetzt wird und dadurch für eine kontrollierte Oxidation zur Verfügung steht. Auf diese Weise ist es möglich, ein gleichmäßiges Wachstum von ultradünnen ZrO_2-Filmen mit hoher Reproduzierbarkeit zu erreichen. Allerdings ist das nur dann durchführbar, wenn die Oberfläche des Einkristalls sauber ist und die benötigte Stöchiometrie aufweist. Bisher wurden Methoden wie STM und LEED dazu eingesetzt, um die Oberflächenstruktur der Legierung vor Erzeugung des Oxidfilms zu untersuchen. LEIS-Experimente ergänzen chemische Oberflächeninformation, welche zum besseren Verständnis des entsprechenden Modellsystems beitragen kann. Außerdem wäre LEIS auch eine geeignete Methode zur Untersuchung der thermischen Stabilität von metallischen Nanopartikeln (z.B. Ni). Diese stellen katalytisch aktive Zentren von SOFC-Anoden dar.

Die Implementierung von LEIS setzt eine exakte geometrische Anordnung von Ionenquelle, Probe und Ionendetektor im jeweiligen UHV-Setup voraus. Dies beinhaltet, dass der Ionenstrahl, der für das menschliche Auge unsichtbar ist, auf die Probe fokussiert wird. Zu diesem Zweck wurde ein Au/Cu-Target entworfen, mit dem die Probenposition und Strahlgröße durch Optimierung des Au-Signals justiert werden konnte. Mittels Justage des Manipulators und der Ionenquelle wurde eine Treffsicherheit von 83,3 at-% Au erreicht.

Um die chemische Zusammensetzung der obersten atomaren Lage von $Pt_3Zr(0001)$ zu ermitteln, wurden polykristalline Metallfolien (Pt, Zr) als Elementstandards für die Quantifizierung eingesetzt. Zudem wurde eine Ni-Folie als weiterer Standard verwendet, um die Quantifizierung von Ni-Nanopartikeln auf $ZrO_2/Pt_3Zr(0001)$ zu ermöglichen. Im Anschluss an umfassende Reinigungsprozeduren wurden LEIS- und XPS-Überblicksspektren aufgenommen. Dabei konnte gezeigt werden, dass es während der Vorbehandlung aufgrund von Segregation von Elementen, die in den Metallfolien (im ppm-Bereich) gelöst vorlagen, zu einer Anreicherung an der Oberfläche kam.

Aufgrund von erheblichen Verunreinigungen des $Pt_3Zr(0001)$ Kristalls durch graphitischen Kohlenstoff konnte kein ultradünner ZrO_2-Film hergestellt werden – trotz wiederholter und optimierter Reinigungszyklen. LEIS-Spektren, welche nach kurzem Sputtern aufgenommen wurden, zeigten Abweichungen der Oberflächenstöchiometrie (Pt/Zr ≈ 5:1 statt 3:1). Tiefenprofile, welche über winkelaufgelöste XPS nach zwei unterschiedlichen Vorbehandlungen erhalten wurden, deuteten darauf hin, dass die erwünschte Stöchiometrie nur im Kristallinneren vorhanden war, während im Zuge des Temperns Kohlenstoff aus Zwischengitterplätzen immer wieder an die Oberfläche segregierte.

Abstract

Within this thesis, theoretical aspects of LEIS are presented, in analogy to a game of billiard. In doing so, fundamentals that should facilitate interpretation of spectra for users are discussed, as well as the origin of the method's ultimate surface sensitivity. The focus is on determining the chemical composition of the utmost atomic layer of solid surfaces, in particular that of metallic alloys or intermetallic compounds, which are important substrates for growing model catalysts. Preserving the chemical and structural integrity of the topmost atomic layer during analysis poses a great challenge. However, scattering of low-energetic He^+-ions keeps the investigated surface intact and also offers utmost surface sensitivity, which is a unique combination in surface analytics.

For this work a new $Pt_3Zr(0001)$ single crystal was used, which provides the opportunity to grow an ultrathin ZrO_2 film. ZrO_2 is a material of highest interest, especially concerning current research on solid oxide fuel cells (SOFC) and related catalytic properties. The synthesis of a ZrO_2 film through deposition of Zr under UHV by common techniques (e.g. electron beam evaporation) is difficult because Zr has a high melting point and a low vapour pressure at the melting point. Nevertheless, it has been reported in literature, that oxidation at elevated temperatures liberates the Zr from the top atomic layers and a thin ZrO_2 film is formed. In this way, continuous ZrO_2 thin films are accessible with uniform surface structure, and with a high reproducibility. However, this only works if the surface of the single crystal is clean and has the correct stoichiometry. Up to now, STM and LEED have been applied to study the surface structure of alloy and oxide film. LEIS experiments complement chemical information on the surface of this model system. In addition, LEIS may also shed light on the thermal stability of metal nanoparticles (e.g. Ni), deposited onto the ZrO_2 film. These represent catalytically active centres of SOFC anodes.

The implementation of LEIS requires an accurate geometric arrangement of the ion source, the sample and ion detector inside the respective UHV setup. This means that the ion beam, being invisible to the human eye, must be focussed onto the sample. Therefore, a Au/Cu-target was designed to adjust the sample position and spot size of the ion beam, aiming for the strongest possible Au-response. Optimum settings of the manipulator and ion gun yielded an accuracy of roughly 83.3 at-% of Au.

In order to determine the chemical composition of the topmost atomic layer of $Pt_3Zr(0001)$, quantification was carried out by employing polycrystalline metal foils (Pt, Zr) as elemental standards. Also, a polycrystalline Ni foil was measured, enabling the quantification of Ni nanoparticles on $ZrO_2/Pt_3Zr(0001)$. After performing extensive cleaning procedures, LEIS and XPS survey spectra were obtained. It was obvious that during cleaning bulk impurities present in the foils at a ppm-level continuously segregated to the surface.

Due to a significant contamination of $Pt_3Zr(0001)$ by graphitic carbon, an ultrathin ZrO_2 film could not be grown – despite multiple attempts and optimisation. LEIS results obtained after short sputtering demonstrated a modified surface stoichiometry (Pt/Zr ≈ 5:1 instead of 3:1). Depth profile analysis by angle-resolved XPS, performed after two different pre-treatments, indicated that the desired stoichiometry was only present in the bulk. However, upon annealing C located at interstitials segregated to the surface.

Content

1. Introduction

Solid surfaces provide a platform for various chemical processes which are of highest interest from a scientific as well as from an economic perspective. In particular, it is the demanding field of heterogeneous catalysis for which the understanding of specific interactions between gaseous or liquid reactants and solid surfaces of catalytically active materials opens new routes for chemical and technological improvements. Therefore, studies of surface properties play a key role. Such properties may be divided into three groups: (1) chemical composition[1,2], (2) surface geometry[3,4] and (3) electronic structure[5,6].[7] The working principle of established characterisation methods is based on either photons, charged particles or applied fields. In many cases reduced pressure or even ultrahigh vacuum (UHV, pressure below 10^{-7} mbar) is required to achieve both well-defined surfaces and proper analytical response. Among features like the elemental range, destructiveness, the spatial-, depth-, energy-, and mass-resolution, the surface sensitivity, which is characterised by the information depth d, is the most significant obstacle. For solids, the surface density is roughly 10^{15} atoms/cm^2 whereas 1 cm^3 of the same material comprises of about 10^{23} atoms (see Figure 1-1).
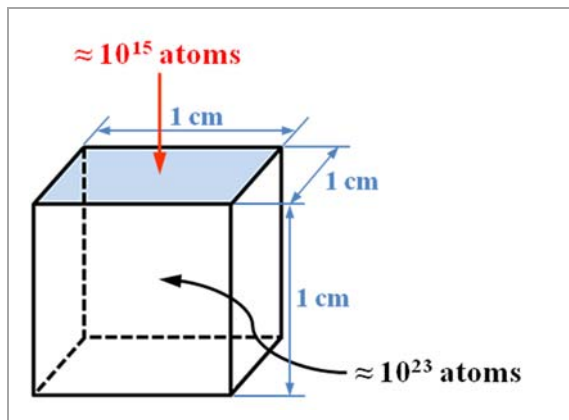
Figure 1-1: Areal versus volumetric atomic density of solids

In other words, the sensitivity of a surface-specific characterisation method must be eight orders of magnitude higher than that of a volumetric method, in order to reach the same detection limit.[8]

The aim of this thesis is to determine the chemical composition of an alloy surface with the highest possible surface sensitivity. The surface stoichiometry influences the growth of thin oxide films, during which one or more alloy species are consumed by film growth. In heterogeneous model catalysis, thin oxide films act as substrates for the growth of metal nanoparticles, leading to so-called "nanoparticle model systems".[9] Although surface science offers a variety of different characterisation methods, only very few methods provide information on the chemical composition of the topmost surface layers.[8,10]

One of the most frequently used techniques is X-ray photoelectron spectroscopy (XPS; also known as electron spectroscopy for chemical analysis, ESCA). A beam of characteristic or, ideally, monochromatic X-ray radiation is focussed onto the sample. Its energy suffices to eject core-level electrons from sample atoms, based on the photoelectric effect, into all spatial directions, into the vacuum chamber of the respective setup. Furthermore, the kinetic energy of the photoelectrons is measured (Figure 1-2, a)). Typically, the detector take-off angle ϑ matches the surface normal of the sample which, depending on the chemical element and the inelastic mean free path λ of photoelectrons within the sample, corresponds to the highest information depth of roughly eight monolayers[1] (ML) or 3λ.[12] Azimuthal rotation of the sample by 10-80° relative to the surface normal (away from the entrance lens of the electrostatic analyser (ESA)) changes the spatial angle of emitted/captured photoelectrons accordingly (Figure 1-2, b)). Applying such angle-resolved measurements (AR-XPS) the information depth can be significantly reduced but is nevertheless still larger than the topmost atomic layer.
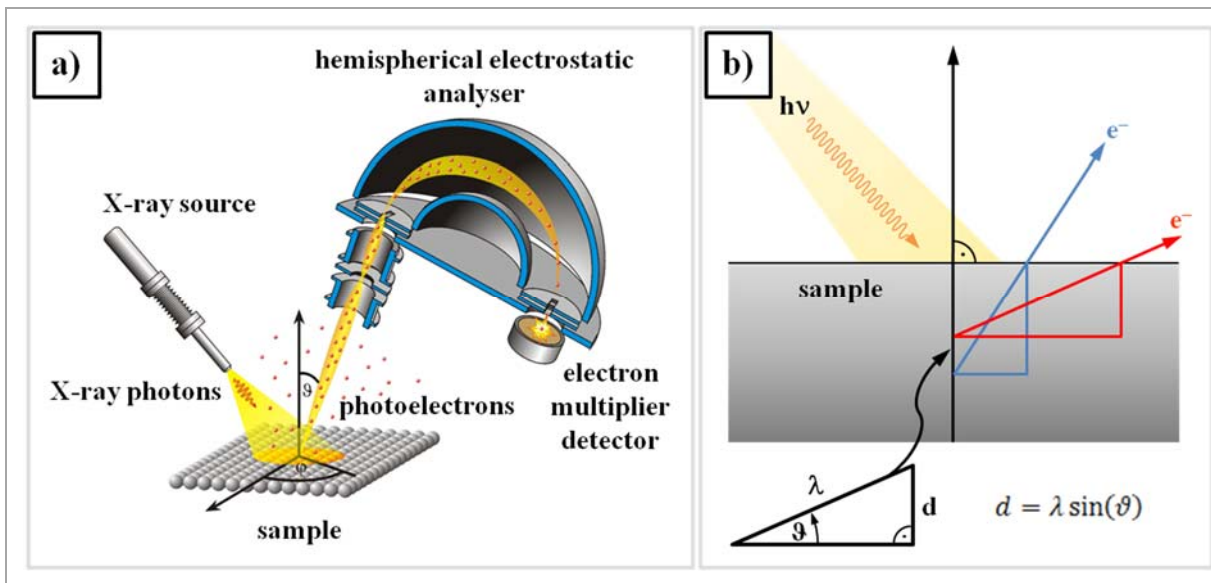
Figure 1-2: Schematic illustration of the principles behind a) XPS[13] and b) AR-XPS

Auger electron spectroscopy (AES) is closely related to XPS. The Auger process[14] occurs preferentially within light elements, in contrast to the activation of secondary characteristic X-ray fluorescence. AES is usually generated by an electron beam in the range of 2-10 keV and includes all elements except for H and He, since the Auger effect can only occur if a target atom possesses at least three electrons.[8,12] The kinetic energy of Auger electrons is generally lower than that of ejected core-level electrons which explains that the information depth can be as low as $\geq$ 2 ML.[8] In secondary ion mass spectroscopy (SIMS) and secondary neutral mass

---

[1] For metals and oxides 1 ML equals approximately 0.2-0.3 nm.[11,12]

spectroscopy (SNMS) a beam of positively or negatively charged primary ions in the range of 10-30 keV is used to probe the sample. If the ion current density is small enough ($\approx$ 1 nA/cm^2) mass analysis of the utmost ML of the sample surface is possible.[15]
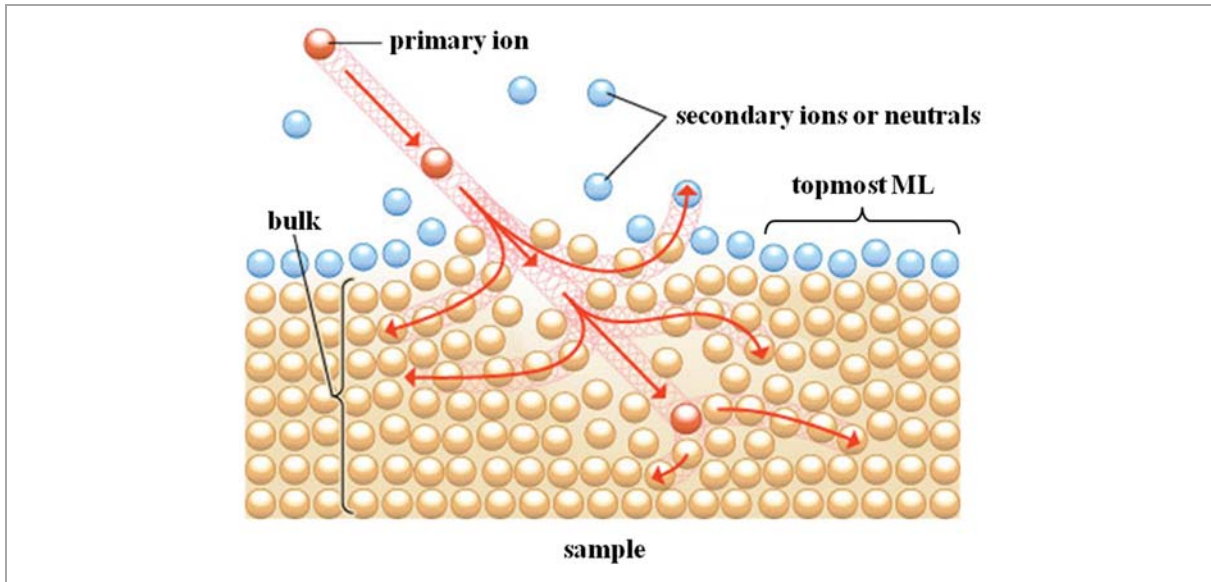
Figure 1-3: Demonstration of the interaction between primary ions and top surface layers of a solid sample in SIMS and SNMS; sputtered secondary particles are analysed by a MS[16]

Alternatively, a pulsed laser, depending on the incident energy density, may also ablate and ionise just the top ML for mass detection (laser microprobe mass analysis, LAMMA). Despite the high surface sensitivity of SIMS, SNMS and LAMMA, the sample surface is destroyed during analysis. This presents a disadvantage for investigations of model systems which require non-destructive analytical methods. In special cases when samples represent nanometre sharp tips, prepared by either electrochemical etching or *via* focused ion beam (FIB), compositional analysis is possible inside a field ion microscope (FIM), coupled to a TOF-MS (atom probe). The size of the tip can be determined by transmission electron microscopy (TEM). Field evaporation of sample ions is achieved by either voltage pulses or laser pulses. Allocation *via* a position-sensitive detector in combination with mass analysis allows the chemical reconstruction of the tip (atom probe tomography, APT). Hence, the chemical composition of the tip's top ML might be derived, depending on the accuracy and spatial resolution of the setup.
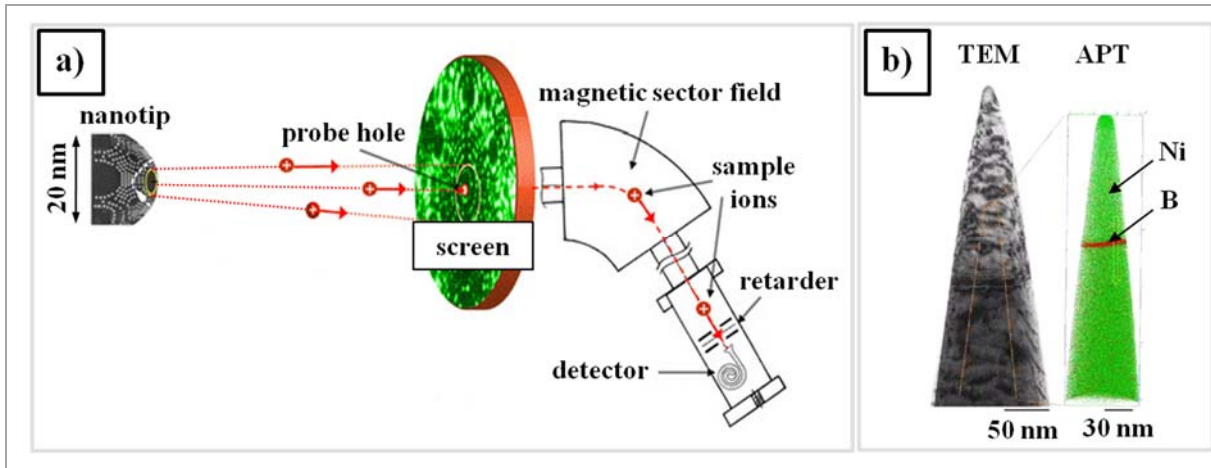
Figure 1-4: a) Schematic presentation of the experimental setup for APT[17] and
b) chemical mapping of a tip[18]

To reach the intended goals of this work, low energy ion scattering (LEIS; also known as ion scattering spectroscopy, ISS), was employed because it has a series of advantages over the methods mentioned above. The term "low energy" differentiates the technique from the related medium energy ion scattering (MEIS) and Rutherford backscattering (RBS), based on their different energy ranges and fields of application. LEIS refers to a kinetic energy of 0.5-10 keV, at which either light alkali ions (Li^+, Na^+) or noble-gas ions (He^+, Ne^+, Ar^+) are accelerated towards the sample surface where they are (back)scattered.[7,8,10] For surface composition analysis the scattering angle θ is fixed. It should be also mentioned that changing the incident angle provides access to structural information. As a result of the ion-atom collision, which will be described in detail below (see chapter 2.1), the projectile ions change their kinetic energy primarily depending on the target atom's mass. As long as these ions are not neutralised in the process, detection is carried out by an ESA/multi channel plate combination (used within this work) or a time of flight mass spectrometer (TOF-MS; this requires a chopped ion beam). LEIS is sensitive to the utmost layer of the surface because of two reasons: (a) At low kinetic energies ions exhibit much higher interaction cross-sections than electrons and photons. (b) The diameter of so-called shadow-cones which obscure target atoms along certain trajectories for incoming ions is of the magnitude of bond lengths.[10] The surface sensitivity additionally benefits from the neutralisation probability of projectile ions in case of ESA/multi channel plate detection which is significantly higher for noble-gas ions than alkali ions.[7,8,10] Furthermore, LEIS exhibits very low detection limits (10^{-2}-10^{-3} ML for light elements and 10^{-3}-10^{-4} ML for heavy elements) and sputtering yields.[19] If He^+-ions are used as projectiles, as in the conducted experiments, the sputtering yield is roughly 10^{-1} atoms/ion. This leads to the assumption that about 10^{-3} ML of the sample surface are removed during the acquisition of one spectrum.[8]

In contrast to SIMS, SNMS or LAMMA, this unique feature enables non-destructive analysis. In addition, it was observed that for a given ion-atom interaction neighbouring surface atoms have no influence, therefore no matrix effects have to be taken into account – although this is still a controversial topic.[20] The spectral peaks originate from elastic scattering but may include contributions from inelastic energy loss, presence of isotopes and multiple scattering, leading to a peak width of 20-30 eV.[19] The energy resolution is reduced upon increasing mass of the target atom which, in combination with the peak width, represents the most severe limitation of LEIS – its poor mass resolution. He^+-projectiles offer the largest acquirable elemental range in comparison to other mentioned probe ions. Apart from H and He all chemical elements can be detected. Quantification, using elemental standards, can be rather easily achieved, however, especially for metallic alloys.[8]

LEIS has already been successfully applied for the analysis of the chemical composition of alloy surfaces[21], as also shown in this work, for nanoparticles on top of oxidic supports[22] and for the study of adsorbates on solid surfaces, which is of particular interest in the field of heterogeneous catalysis.[8]

2. Basic theory of LEIS

The discovery of the interaction between projectile ions and nuclei of target atoms of a Au foil was reported for the first time by E. Rutherford in 1911[23]. This laid the foundation for the first atomic model and for subsequent milestones in nuclear physics. During the following decades it was demonstrated that ion scattering also offers powerful analytical capabilities.[24] Due to instrumental limitations (e.g. the need of advanced vacuum technology) first practical applications emerged only in the 1960ies. At that time D. P. Smith and scientists from the former Soviet Union developed LEIS as a new tool for surface analysis.[7]

The working principle of LEIS is straightforward and has several steps: Primary ions of a known element are accelerated by an electric field to a desired (uniform) kinetic energy (0.5-10 keV). The ion beam formed is focused onto a solid sample, mounted inside a UHV chamber. Then, the energy distribution of primary ions backscattered from the sample surface is measured for a fixed scattering angle θ.[10] The obtained spectra plot the ion count rate versus the kinetic energy of the scattered ions, with the analytical information being limited to the topmost atomic layer(s) of the surface. In most cases, assignment of individual peaks to individual elements is possible, making the qualitative analysis *via* integration of peak areas rather simple, especially in comparison to MS techniques when fragmentation may result in complex spectra.

2.1. Qualitative analysis

2.1.1. Single elastic collision

It was found that the scattering patterns can be explained by the single or binary collision model, which is based on elastic scattering of hard balls.[10,25] This model can be illustrated by a collision occurring during a game of billiard as follows:

(a)   The queue serves as accelerator for the primary collision partner, the white ball, which is targeted onto a coloured ball.

(b)   All collision partners are located near a pocket of the billiard table.

(c)   The initial velocity of the white ball is the same in every trial.

(d)   There is an infinite supply of white balls. The goal – in contrast to real billiard – is to sink the white ball and measure its velocity after the collision (hypothetically, the pocket is equipped with a sensor which enables to determine the velocity). This collision can be repeated many times for better statistics.

(e)   The impact trajectory and thus the initial position of the white ball can be shifted in parallel to make sure that the white ball meets the pocket, which requires a specific collision geometry.

(f)   There is no friction between the table and the balls as well as between the balls. The impact of the white ball does not cause a sound, change of thermal energy or physical damage. There is no spin added to the motion of collision partners.

Figure 2-5 demonstrates the collision between the white ball and a target blue ball, with the white ball intended to hit the pocket.
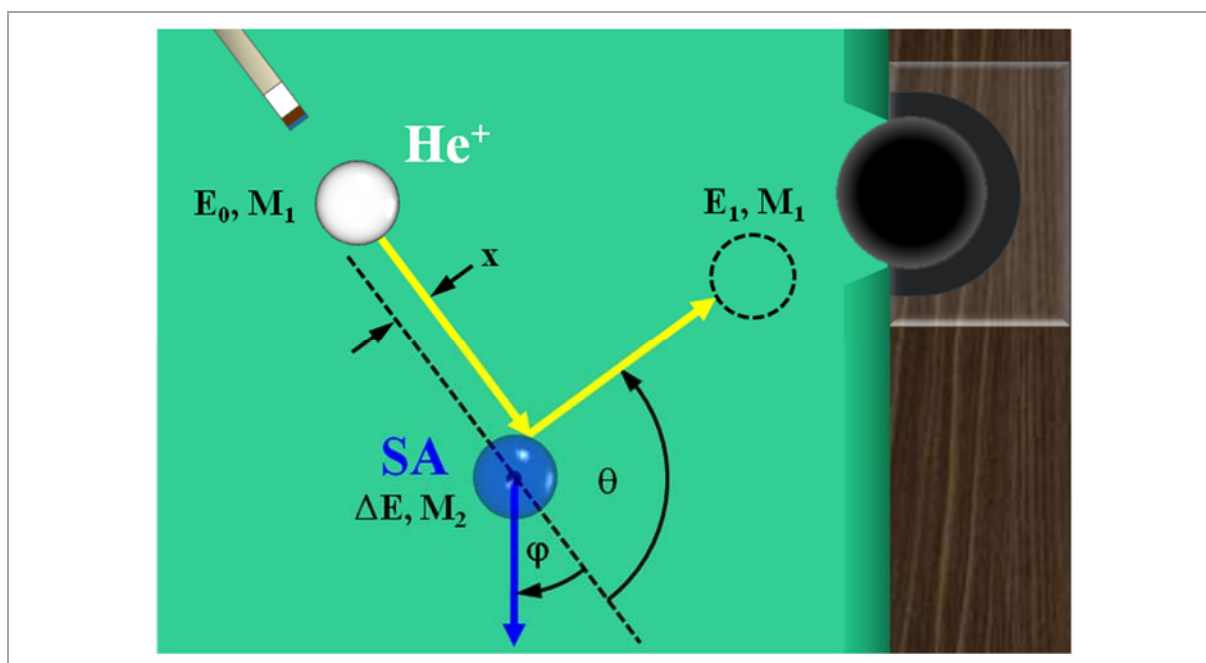
Figure 2-5: Geometric illustration of a collision during a billiard game, representing the kinematic single collision model; see the text for the labels.

If the offset x from the central collision trajectory (dashed line), also called impact parameter, is correct, the white ball (mass M_1, kinetic energy E_0) will be deflected into the pocket. After the collision, the white ball exhibits a kinetic energy E_1 and the target blue ball (mass M_2) is pushed away with a kinetic energy ΔE. The dashed line, which is prolonged behind the blue ball, and the trajectories of the collision partners define two angles: the scattering angle θ and recoil angle φ. The label "He$^+$" clearly hints at the type of projectiles used for the experiments conducted and "SA" stands for "surface atom".

An ideal elastic collision is characterised by the conservation of (kinetic) energy E and momentum p which, applied to Figure 2-5, leads to:

$$\Delta E = E_0 - E_1 \tag{2.1}$$

The definition of kinetic energy $E := \frac{1}{2}M\vec{v}^2$ and momentum $\vec{p} := M\vec{v}$ results in:

$$E = \frac{\vec{p}^2}{2M} \tag{2.2}$$

Equation (2.2) allows the following substitution of (2.1):

$$\frac{\Delta\vec{p}^2}{M_2} = \frac{\vec{p}_0^2}{M_1} - \frac{\vec{p}_1^2}{M_1} \tag{2.3}$$

The momenta in (2.3) are geometrically related *via* the Thales circle:
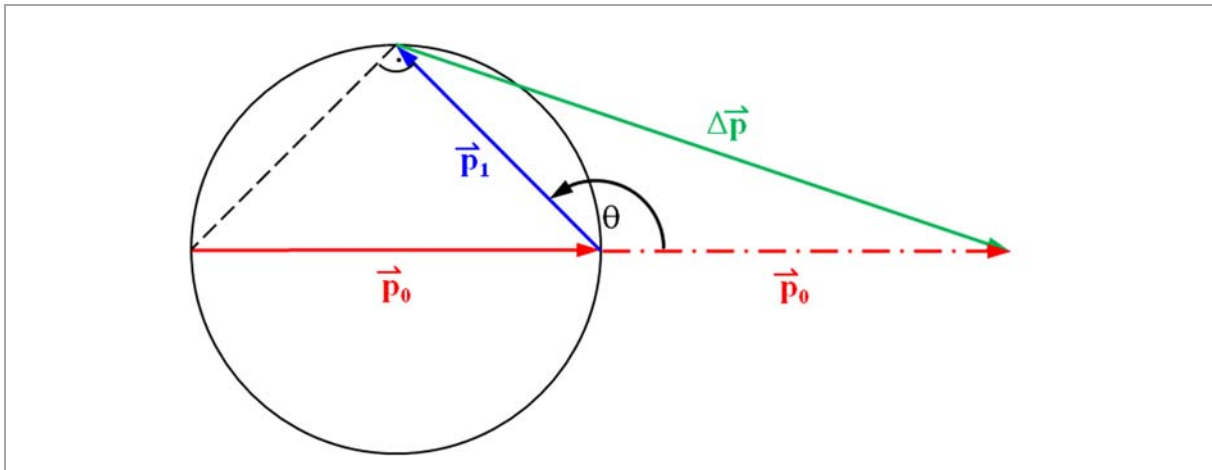
Figure 2-6: Geometric relationship between occurring momenta
(simplified for a centrosymmetric collision, $x = 0$)

Figure 2-6 shows that the momenta span a triangle that includes θ and is described by the cosine theorem:

$$\Delta\vec{p}^2 = \vec{p}_0^2 + \vec{p}_1^2 - 2\vec{p}_0\vec{p}_1\cos(\theta) \tag{2.4}$$

The combination of equations (2.3) and (2.4) yields:

$$\vec{p}_0^2 + \vec{p}_1^2 - 2\vec{p}_0\vec{p}_1\cos(\theta) = \frac{M_2}{M_1}(\vec{p}_0^2 - \vec{p}_1^2) \tag{2.5}$$

(2.5) is a quadratic equation of $\vec{p}_1$ which is simplified by $a := \frac{M_2}{M_1}$ and its solution is:

$$\vec{p}_{1(\pm)} = \vec{p}_0 \frac{\cos(\theta) \pm \sqrt{a^2 - \sin^2(\theta)}}{1 + a} \tag{2.6}$$

The white ball will only hit the pocket if $M_2 > M_1$ or $a > 1$, respectively. Therefore, the negative sign in front of the square root in (2.6) does not apply and by employing (2.2) the following expression is obtained:

$$\frac{E_1}{E_0} := k = \left(\frac{\cos(\theta) + \sqrt{a^2 - \sin^2(\theta)}}{1 + a} \right)^2 \tag{2.7}$$

Herein, k is called kinematic factor and is a function $k(a, \theta)$, graphically represented by Figure 2-7. If θ is constant, then E_1 and k only depend on a, for which M_1 is known and M_2 can thus be deduced by measuring E_1.
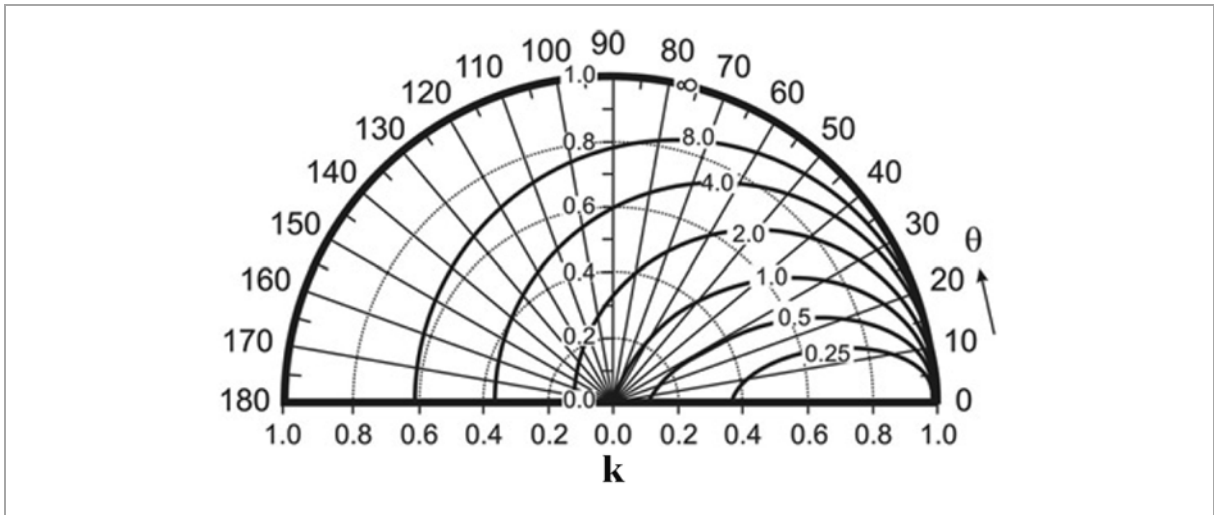
Figure 2-7: Polar plot of the kinematic factor k as a function of a and θ[20]

In similar way a relationship for calculating the kinetic energy of the recoiled blue ball at a recoil angle $\varphi \leq 90°$ is derived to complete the picture:

$$\frac{\Delta E}{E_0} := k' = \frac{4a}{(1 + a)^2} \cos^2(\varphi) \tag{2.8}$$

But how does this model relate to LEIS and why is it important? The answer is apparent if the significant elements of the billiard game are replaced by components of the experimental setup of this work:
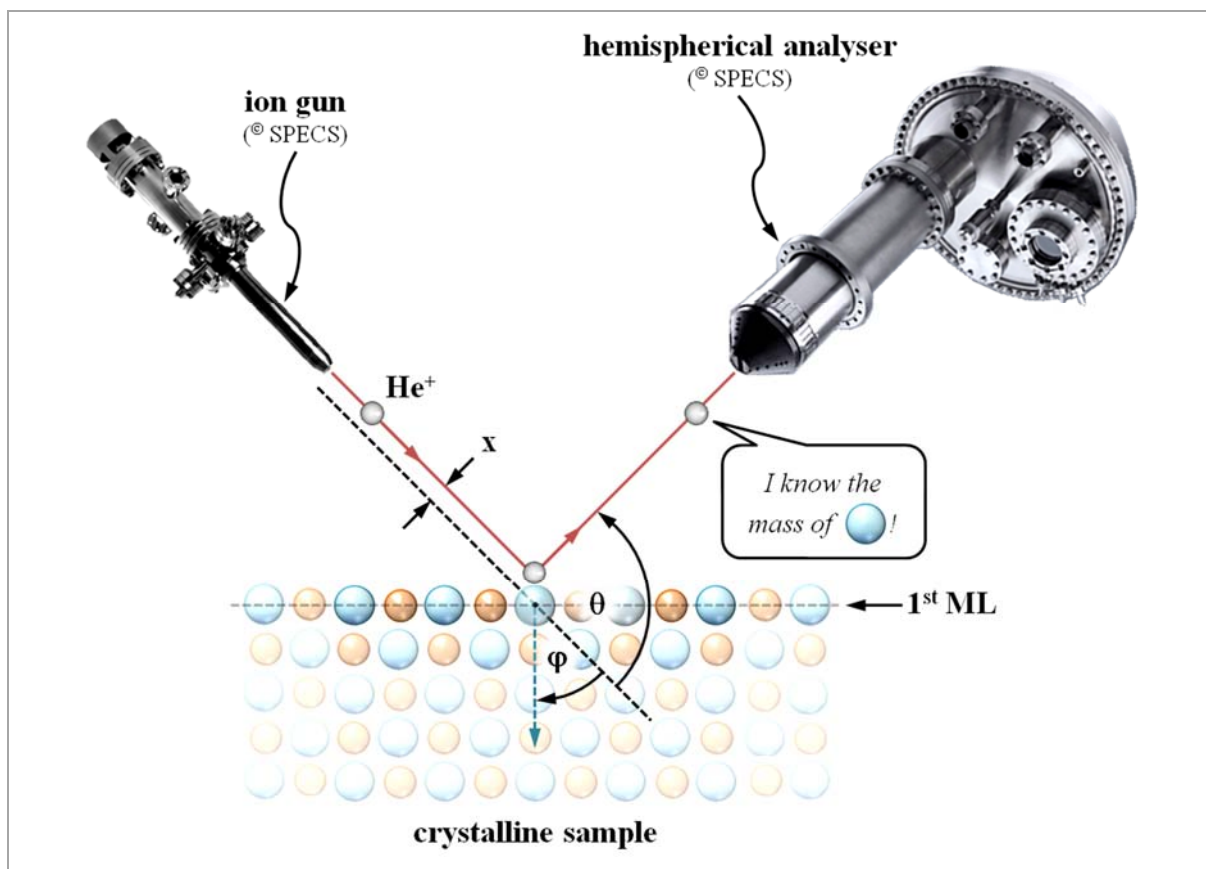

Figure 2-8: Schematic drawing of the experimental setup[26,27]

The previously described features of the billiard game are now "translated" to those of LEIS experiments:

(a) He+-ions (formerly the white balls; hence, M_1 is known) are accelerated by an ion source and collide with a surface atom (formerly the blue ball; M_2 to be measured) of a crystalline (or amorphous) sample at a given temperature. The sample is mounted on a sample holder in the centre of a UHV chamber (see chapter 3.1).

(b) Instead of the billiard pocket/sensor combination an ESA with attached multi channel plate detector is employed to measure the kinetic energy E_1 of He+-ions backscattered from the sample atoms. Ion source and ESA are mounted onto flanges of the UHV chamber, centred to the sample and fixed in position.[2]

---

[2] A TOF-MS would allow the analysis of both the ionic and neutral component of the scattered particle flux but at a lower energy resolution. Also, the topmost and deeper layers could not be differentiated.[32]

(c)   The kinetic energy of He^+-ions prior to the collision E_0 is 1 keV.

(d)   A constant flux of He-atoms is ionised. Only He^+-ions are measured. He-atoms are "invisible" to the ESA.

(e)   Backscattering occurs for every chemical element except H and He, if He^+-ions are used as projectiles due to equation (2.7). Thus surface atoms of different elements can be differentiated *via* their different kinetic energies E_1.

(f)   A He^+-ion beam is focused onto a sample which presents a round target with a diameter of 5 mm. He^+-ions move along parallel trajectories and are scattered from the sample surface in all possible directions (apart from other interactions that may appear; for details see chapter 2.1.3). The ions which are backscattered to the entrance slit of the ESA are detected. Therefore, the acquired scattering angle θ is fixed.

(g)   At 1 keV, He^+-ions move at a velocity of $2.2 \cdot 10^5$ m·s^{-1} (220 km·s^{-1}) and, if treated as waves, have a de Broglie wavelength of $4.5 \cdot 10^{-3}$ Å. Relativistic mass increase as well as diffraction of He^+-ions are excluded, because their de Broglie wavelength is by a factor 10^3 smaller than typical bond lengths in crystals. Conditions for elastic collisions between He^+-projectiles and surface atoms are given by the following criteria:

I.   The vibrational energy of atoms in solids is estimated to be 40 meV at room temperature.[25] The interaction time of He^+-ions and target atoms is orders of magnitude shorter than the period of thermal vibrations of surface atoms and there is no coupling with phonons.[28-30] Thus, surface atoms behave as quasi-free static particles.

II.   The magnitude of the repulsive atomic potential of target atoms is only comparable to E_0 of approaching He^+-ions at distances of roughly 0.5 Å which is why single collisions occur.[31] For low energy ions quantum effects can be neglected based on the theory developed by N. Bohr, therefore ion scattering can be treated as classical phenomenon.[30]

III.   The effects of charge transfer, electronic excitation and other inelastic interaction processes (see chapter 2.1.3) are not considered because they are negligible compared to the elastic energy loss through transmission of momentum.

Figure 2-9 represents an example for LEIS spectra, acquired by J. Morais et al.[33] from a Zr silicate film, prepared by chemical vapour deposition (CVD) of Zr onto a Si substrate. These substrates are known to form substantial amounts of silicon oxide (silica), even under UHV. Postannealing within an enriched $^{18}O_2$-atmosphere showed that mass transport of ^{16}O, deriving from silica that existed before the deposition of Zr, to the surface and strong ^{16}O-^{18}O exchange throughout the entire silicate film took place. This is reflected by the detection of both isotopes *via* LEIS.
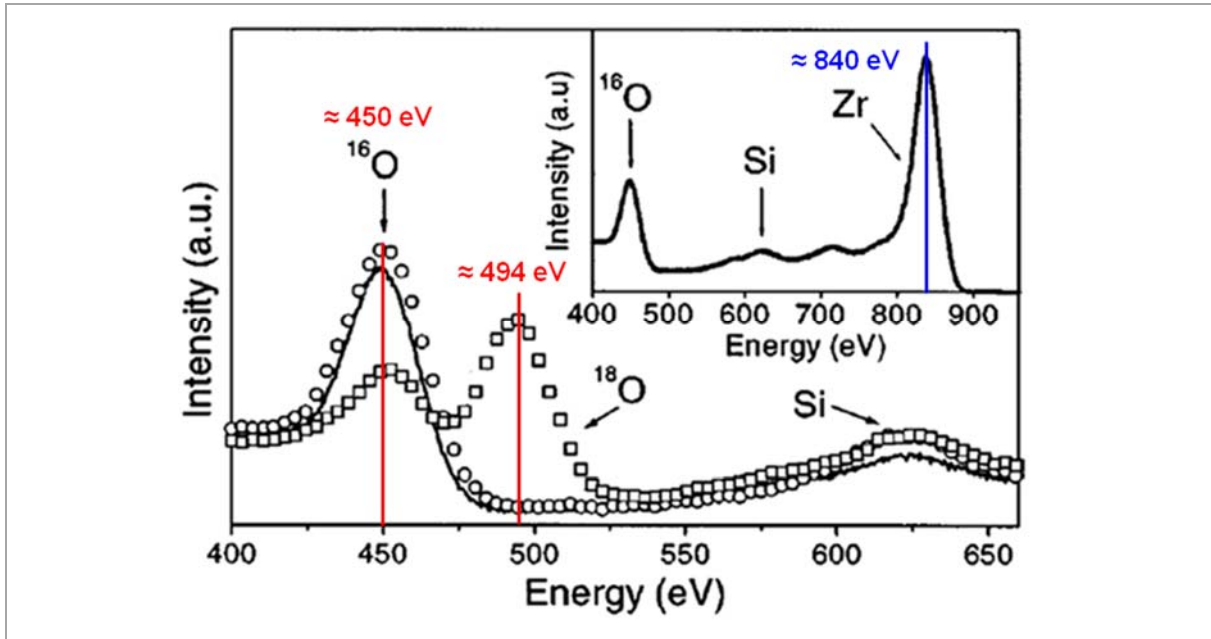
Figure 2-9: LEIS spectrum (1 keV He$^+$, $\boldsymbol{\theta}$ = 165°) of a ZrSi$_x$O$_y$ film deposited on a Si substrate; the full spectrum is shown in the inset[33]

Equation (2.7) predicts that the difference between measured kinetic energies E_1 of 1 keV He$^+$-ions scattered on ^{16}O- and ^{18}O-atoms at an angle of 165° to be 44.9 eV, and that the main component Zr should appear at a kinetic energy of 841.5 eV. This corresponds very well to the recorded spectra.

2.1.2. Multiple elastic collisions

Apart from elastic single collision signals which dominate for light He$^+$-projectiles[10] and samples of simple structure and composition, LEIS spectra may also exhibit higher complexity, for example when the incident angle α of projectile ions is changed so that multiple collisions with sample surface atoms may occur. For a given type of projectile, fixed primary kinetic energy and fixed scattering angle θ, multiple collisions are favoured both for flat (small) or steep (large) incident angles, small interatomic distances, a significant size difference between

neighbouring atoms and surface roughness/corrugation[21]. All these aspects have in common that the trajectories of projectiles after a single collision are blocked by other surface atoms.

However, the necessary condition for multiple scattering is even fulfilled if a beam of parallel moving ions impinges on a perfectly flat solid surface. This is better understood if the surface is simplified to a string of atoms of its top layer. Additionally, instead of considering all possible trajectories of projectile ions, as they fill out the major part of space surrounding the scattering targets, it is far easier to look at those regions which classical particles cannot enter. These banned areas are located behind each target from the "perspective" of the incoming ion. The trajectories around converge and form a paraboloid, either called "shadow-cone" in case of the first collision or "blocking-cone" which in fact is again a shadow-cone but refers to an obstruction to the already scattered ion. Figure 2-10 visualises both geometric concepts that are very important to all ion probe techniques.
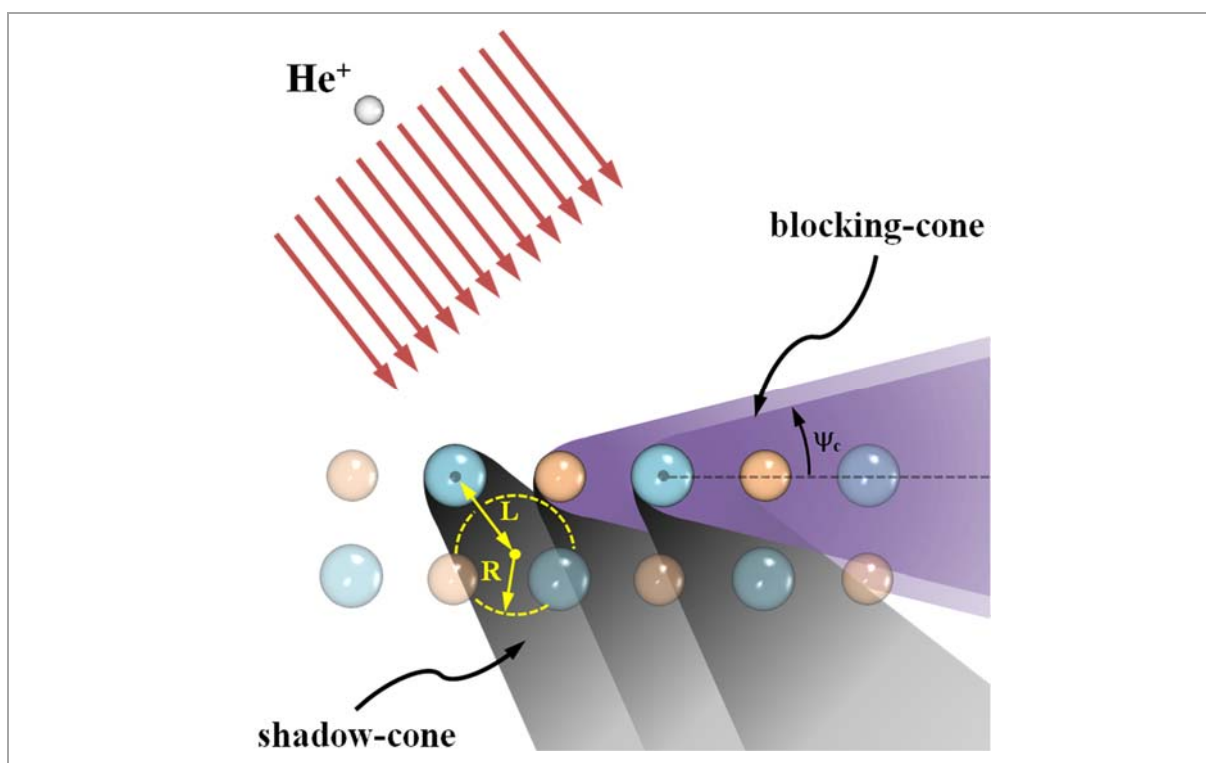
Figure 2-10: Schematic drawing of the shadow- and blocking-cones[7,33]

The repulsive interaction of positively charged ions and nuclei of target atoms, if electronic effects are ignored, is described by the Coulomb potential.

Based on this and more detailed geometric considerations, the radius R of the shadow-cone is approximated:[7]

$$R = 2\sqrt{\frac{Z_1 Z_2 e^2 L}{E_0}} \qquad (2.9)$$

Herein Z_1 and Z_2 are the atomic numbers of the projectile ion and surface atom, e is the elementary charge and L the distance of the surface atom nucleus to the centre of the shadow area (with radius R). The top ML-sensitivity of LEIS is essentially explained by the fact that the magnitude of R is already on the order of typical bond lengths in solids.[10] The blocking-cone is aligned along the interatomic axis (parallel to the surface). It is characterised by a critical opening angle ψ_c enclosed between said axis and the surface of the cone.[7]

For He$^+$-ions at 1 keV the neutralisation probability after a single collision (with metallic atoms) is roughly 90 % and even increases drastically with every additional collision.[8] Thus, it is expected that almost only double collisions are detected by an ESA/multi channel plate detector if multiple scattering of He$^+$-ions occurs. Figure 2-11 displays a simple model for the double collision phenomenon analogous to Figure 2-5 which is understood as two successive single collisions of the white ball with a blue and a red ball.[10]
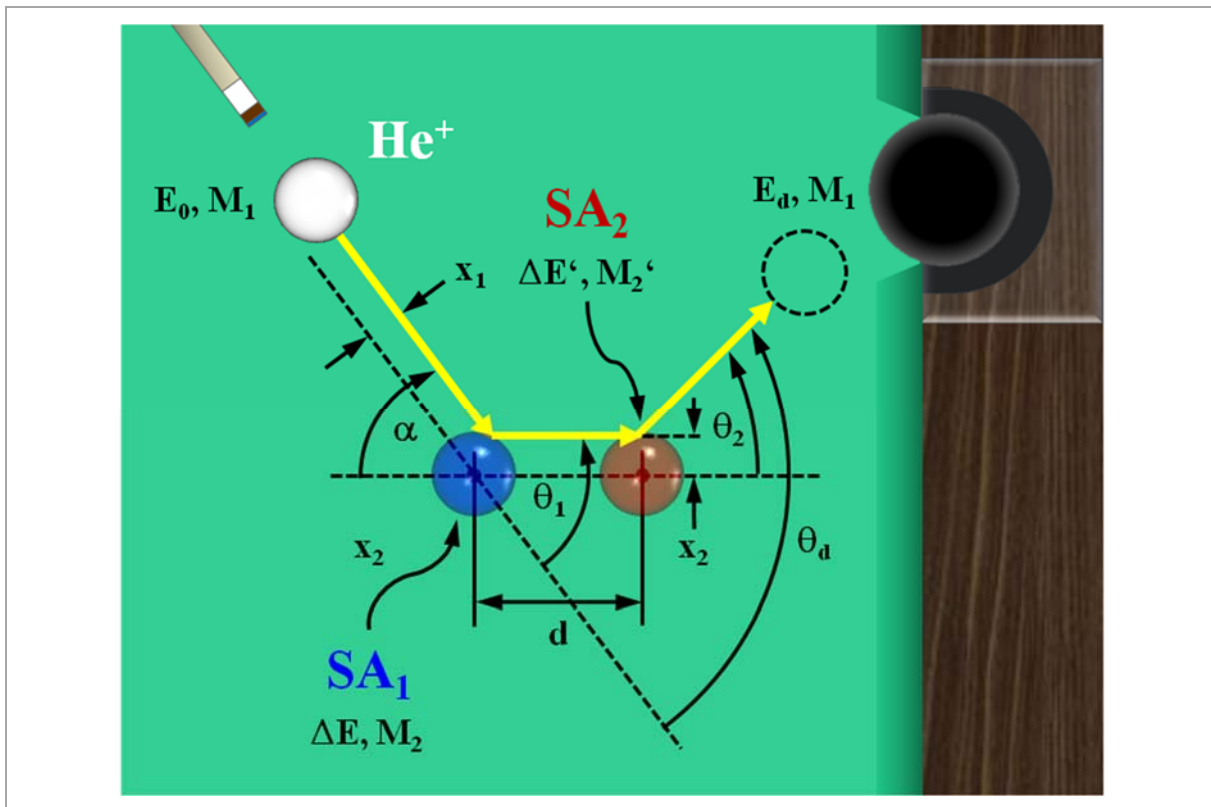
Figure 2-11: Geometric illustration of a billiard game as kinematic double collision model

The distance between the blue and red billiard balls in Figure 2-11 is d and in case those are of different size the impact parameters vary which is reflected by x_1 and x_2. Equation (2.7) is extended to:

$$\frac{E_d}{E_0} = k_1(a_1, \theta_1)k_2(a_2, \theta_2) \tag{2.10}$$

The white ball in Figure 2-11 will only hit the pocket if the double scattering angle θ_d is correct, which is given by:

$$\theta_d = \theta_1 + \theta_2 \tag{2.11}$$

Translated to an experimental setup where θ is fixed, θ_d must equal the scattering angle of a single collision. The most important consequence of (2.7) in context of double scattering is that the kinetic energy transferred from a projectile ion to a surface atom decreases with θ.

By intuition He^+-ions should lose more kinetic energy if they undergo multiple collisions. Hence, it would be expected that double scattering peaks appear at lower kinetic energies in LEIS spectra, in comparison to respective single scattering signals if He^+-ions collided with two surface atoms SA1 and SA2 of the same chemical element ($a_1 = a_2$). In fact, the opposite is the case due to $\theta_1, \theta_2 < \theta_d$. The dependence of k on θ is particularly pronounced for light collision partners, like in the following example: A 1 keV He^+-ion is elastically scattered on a single C-atom at an angle of 135°. Equation (2.7) predicts that the primary kinetic energy E_0 of said ion should be reduced to $E_1 = 305.2$ eV. If double scattering on two neighbouring C-atoms occurs the way it is portrayed in Figure 2-11 and the incident angle α is 11° with respect to the surface normal, then $\theta_1 = 79°$ and $\theta_2 = 56°$. Accordingly, $k_1 = 0.5725$ and $k_2 = 0.7408$ which leads to a kinetic energy $E_d = 424.1$ eV. Everything becomes even more complicated if multiple scattering involves two surface atoms of different chemical elements which may result in signals somewhere in the midrange of the LEIS spectrum.

Angle-resolved experiments not only allow distinguishing between single and multiple scattering signals but also to obtain structural data of the sample surface (roughness).[7,10,30]

2.1.3. Overview to further ion-atom interactions in LEIS

The kinematic description of the ion-atom collision outlined above disregarded the role of inelastic effects. Peak shifts to lower kinetic energies (for 1 keV He$^+$-ions scattered from various elements by 19-35 eV[20]) as well as peak broadenings observed in LEIS spectra are, however, an indication of their significance. With regard to condition I for elastic scattering (see chapter 2.1.1) it was reported that a 1 keV He$^+$-ion scattered on an Al atom with a vibrational energy of only 25 meV caused a Doppler peak broadening of about 5 eV.[20] Atoms of solid surfaces exhibit chemical bonds to neighbouring surface atoms as well as to atoms underneath. Energies of primary atomic bonds in solids (i.e. metallic and covalent bonds) are in the range of 1-10 eV.[34] Therefore, it is feasible that these bonds "cushion" the impact to a certain extent until the transmission of momentum is sufficient to cause bond dissociation. Condition III, on the other hand, involves several types of interactions, as summarised in Figure 2-12.
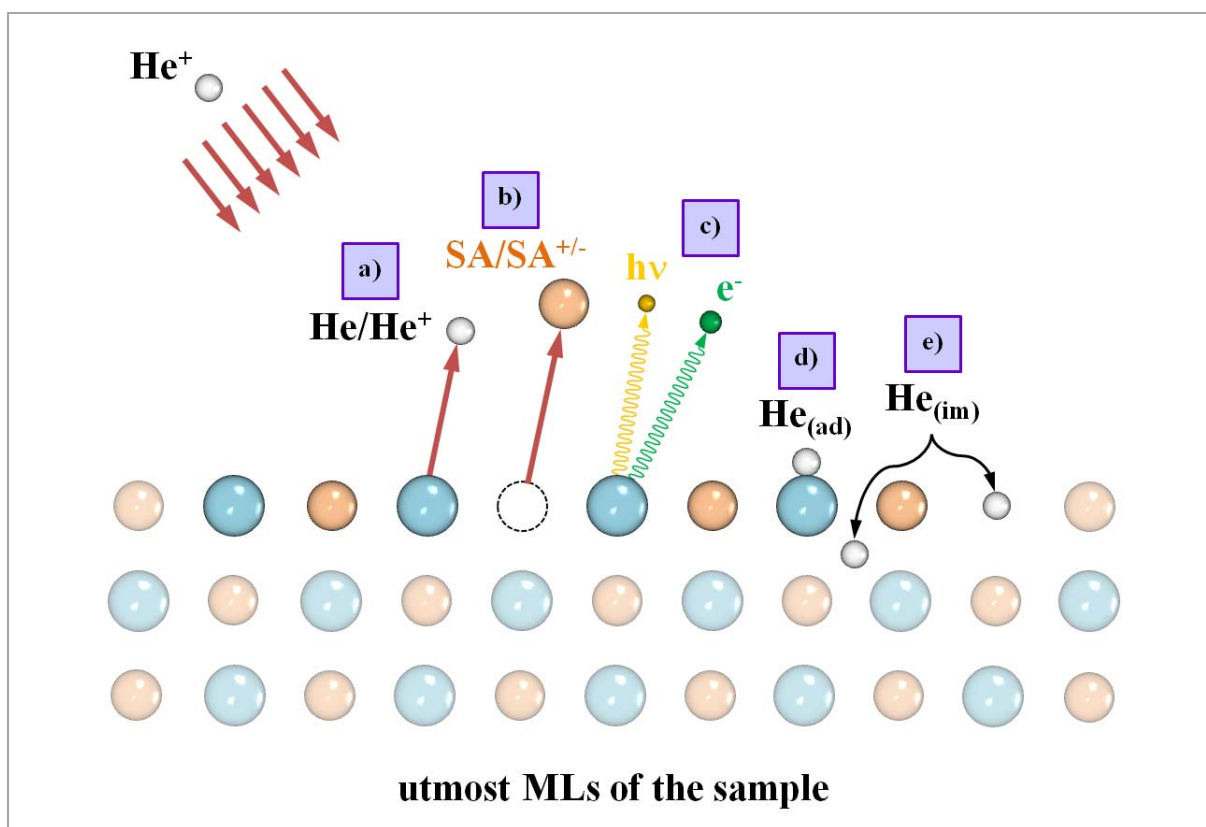
Figure 2-12: Possible effects that accompany the backscattering of He$^+$-ions from surface atoms and change the topmost atomic layers of the sample

a) *Neutralisation and reionisation:* Within the discussion of multiple scattering in the previous chapter it was mentioned that He^+-ions show a very high tendency for neutralisation in the presence of surface atoms. This behaviour is favourable because it directly correlates with an enhanced first monolayer-sensitivity but unfavourable at the same time due to drastically reduced signal intensity if only ions are detected. Despite the short collision time window, being in the range of 10^{-16}-10^{-15} s[25], incoming He^+-ions are capable of interacting with the conduction band of surface atoms. At closest approach He^+ may be neutralised through electron capture.[7] This is understood as either a resonant (determined by the tunnelling probability) or collision-induced (i.e. by electronic excitation and level crossings of the He 1s level with open valence levels of the target atom) effect[20] and also leads to reionisation of He-atoms. In both cases a threshold energy exists as a barrier which, for a fixed scattering angle θ, depends on the ion-atom or atom-atom distance.[35] The fact that most LEIS experiments are performed in the reionisation regime is an important issue because it may significantly increase the information depth.[36] Furthermore, a complete charge changing cycle of $He^+ \rightarrow He^0 \rightarrow He^+$ reduces the kinetic energy of the projectile by ≥ 20 eV.[20]

b) *Sputtering:* Bombardment by primary ions transferring sufficient amounts of kinetic energy to surface atoms and recoil atoms may trigger collision cascades within the first few atomic layers of the sample. A detailed theoretical description of this phenomenon was proposed by P. Sigmund in his famous work[37] and often illustrated by Monte Carlo simulations[38]. As a result, low-energy atoms, ions, molecules, fragments and clusters in various charge states emerge from the sample into the vacuum.[7] Usually, He^+-ions that participate in sputtering cascades are not available for ion detection. Sputtering also diminishes the top monolayer-sensitivity of LEIS but if He^+-ions are utilised at 1 keV, which represents the lightest noble-gas ion hitting the sample surface at the lower end of the typical kinetic energy range, the surface damage is kept to a minimum. The sputtering probability correlates with increasing kinetic energy and mass of the projectile and is therefore generally higher for alkali ions.

c) *Photon and Auger electron emission:* Details of the electronic structure of surface atoms strongly influence the dynamics of the projectile's atomic levels in close collision encounters.[36] Changes caused by charge transfers that occur along the way might lead to excitation of electrons to highly excited states. Relaxation from those states is accompanied by the emission of either photons or Auger electrons. The latter also contribute to the neutralisation of projectile ions.

d) *Adsorption:* Multiple collisions and inelastic energy losses can slow down the projectiles to a point where attraction to the surface occurs. Noble-gas ions like He^+ are exclusively physisorbed to surface atoms. Alkali ions on the other hand may undergo chemical reactions.

e) *Implantation:* In particular, low energy heavy ions colliding with target atoms of the first atomic layers of the surface may alter the chemical composition due to dislocations, replacements and interstitials.[27] Again this effect is expected to play a minor role for 1 keV He^+-ions.

2.1.4. Mass resolution

The relationship between measured kinetic energies E_1 of backscattered projectile ions and masses of target atoms M_2, pointed out by equation (2.7), implies that the effective energy resolution directly correlates with the mass resolution. For constants E_0, M_1 and $\theta > 90°$ Figure 2-13 indicates that $E_1(M_2)$ is a function which increases monotonously with M_2.

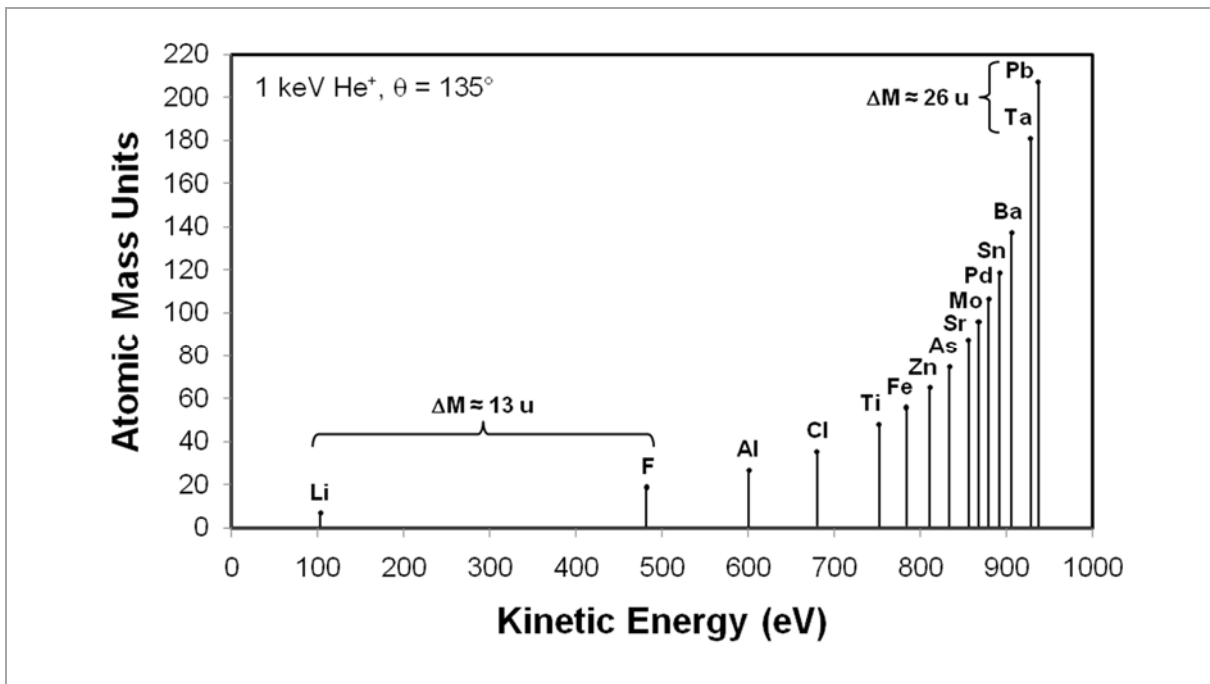**Figure 2-13:** Elastic scattering of He^+-ions at different target atoms

According to Figure 2-13 He$^+$-ions are very sensitive to light target atoms and clear identification should be possible up to atomic masses around that of e.g. Fe. Within this range even isotopes are more or less reliably resolved. Signals deriving from heavier collision partners are progressively getting closer in E_1, preventing an explicit differentiation of elements, especially if there are contributions from multiple collisions and inelastic effects. It is still possible to identify e.g. Pt nanoparticles deposited on alumina but not Cu and Zn in brass. A small improvement is reached by using heavier projectiles (e.g. Ar$^+$)[40] but accompanied by a significant loss of surface sensitivity (and increased beam damage). Based on equation (2.7) a mathematical relationship for the mass resolution can be derived ($a > 1$):[8,10]

$$\frac{M_2}{\Delta M_2} = \frac{E_1}{\Delta E_1} \frac{a + \sin^2(\theta) - \cos(\theta)\sqrt{a^2 - \sin^2(\theta)}}{a^2 - \sin^2(\theta) + \cos(\theta)\sqrt{a^2 - \sin^2(\theta)}} \qquad (2.12)$$

This equation infers that large scattering angles θ lead to better mass resolution.

2.2. Quantitative analysis: determination of the chemical composition of sample surfaces

Whilst the spectral position of peak maxima is adequately described by elastic single and multiple scattering the resulting peak area A_i, which is related to the number of collision partners of a certain species i, is a product of various parameters:[41]

$$A_i(E_0, \theta) = I \frac{d\sigma_i}{d\Omega} \widetilde{N}_i Y_i f R \qquad (2.13)$$

Therein, I is the projectile ion current, $\frac{d\sigma_i}{d\Omega} := \sigma_{\text{diff}, i}$ the differential scattering cross-section[3], $\widetilde{N}_i$ the areal density, Y_i the projectile ion yield, f an experimental factor which includes e.g. the transmission of the ESA and R the surface roughness. I and f are determined by the experimental setup and are accessible with good accuracy. $\sigma_{\text{diff}, i}$ is calculated but has some degree of uncertainty because it depends on the interaction potential $V(r)$ which is only estimated.

---

[3] $\sigma_{\text{diff}, i}$ is defined as the ratio of the number of particles (here: He$^+$-ions) backscattered from the surface into the solid angle $d\Omega$ to the areal atom density $\widetilde{N}_i$ of a sample surface species i.[7]

$V(r)$ includes the nuclear charges of the projectile ion $Z_1 e$ and target atom $Z_2 e$ whereas the latter is approached along a distance r:[10]

$$V(r) = \frac{1}{4\pi\varepsilon_0} \frac{Z_1 Z_2 e^2}{r} \Phi\left(\frac{r}{b}\right) \tag{2.14}$$

The Coulombic pre-factor, containing the vacuum permittivity ε_0, is multiplied with a "screening function" $\Phi\left(\frac{r}{b}\right)$ which accounts for the interaction between the projectile and electrons, surrounding the target atom, along a screening length b. At high primary kinetic energies E_0, applied in RBS or MEIS experiments, $V(r)$ matches the Coulomb potential which leads to the Rutherford scattering cross-section:[8]

$$\frac{d\sigma_i}{d\Omega} = \left(\frac{Z_1 Z_2 e^2}{4 E_0}\right)^2 \frac{1}{\sin^4(\theta)} \tag{2.15}$$

However, in LEIS $\Phi\left(\frac{r}{b}\right)$ contributes significantly to $V(r)$ which falls off faster than $1/r$, also outlined in Figure 2-14.[8,10] In other words, the repulsion between positive charges in the ion-atom collision is weakened because of electrons shielding the target nucleus. This is why scattering cross-sections obtained in LEIS are much higher than in RBS or MEIS.
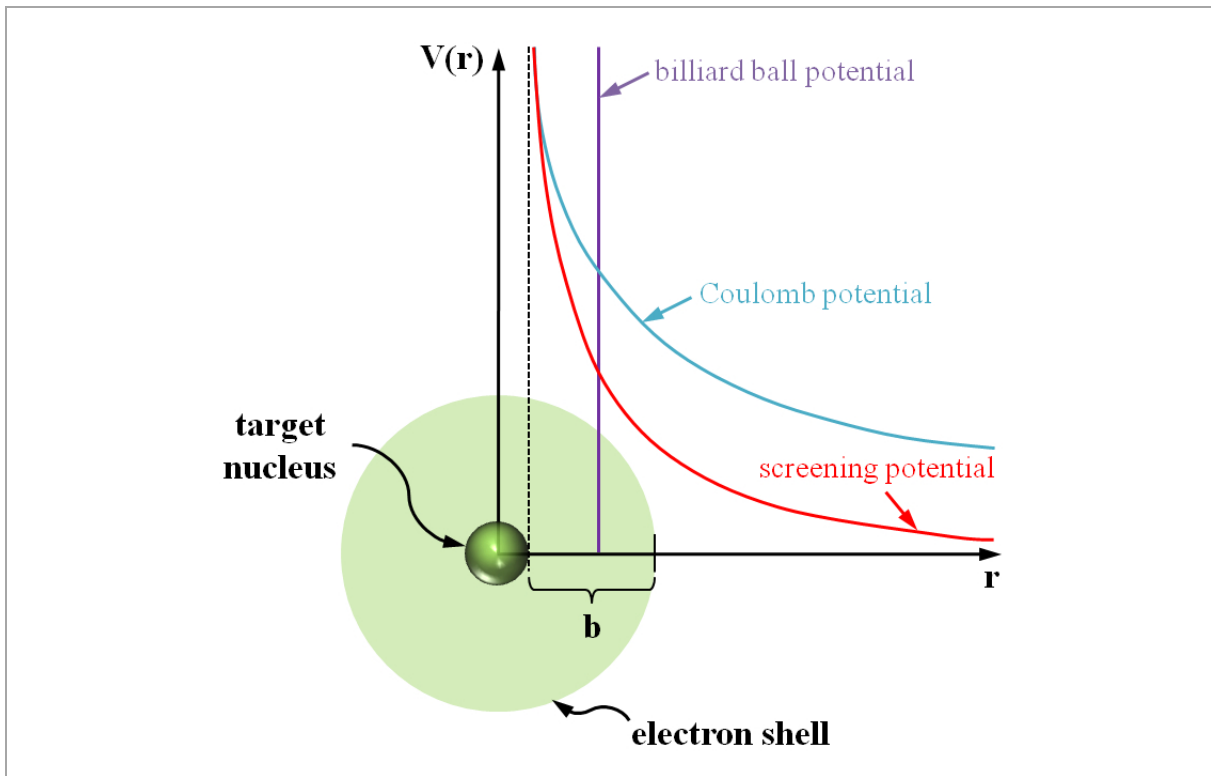

Figure 2-14: Schematic comparison of interaction potentials[8]

In order to estimate the screening potential the Thomas-Fermi-Molière approximation or empirical Ziegler-Littmark-Biersack function is applied.[4] However, Y_i and R compromise the quantification because it is virtually impossible to provide specific values. Compensation of this disadvantage is mastered by using elemental reference samples.[42] If these show very similar characteristics and experimental conditions are kept constant it is appropriate to simplify equation (2.13) to:

$$A_i(E_0, \theta) \approx \frac{d\sigma_i}{d\Omega} \widetilde{N}_i \qquad (2.16)$$

Even though a reasonable approximation for absolute values of $\widetilde{N}_i$ (atoms per unit of surface area) can be determined that way, in practice it is convenient to calculate atomic ratios X_i.[12] In case of a binary metallic alloy Vegard's law $X_1 + X_2 = 1$ applies and X_1 is given by:[8]

$$X_1 = \frac{1}{1 + \frac{A_2}{A_1} \frac{A_{ref,1}}{A_{ref,2}} \frac{\widetilde{N}_2}{\widetilde{N}_1}} \qquad (2.17)$$

---

[4] A detailed explanation is beyond the scope of this work but available in the literature (see [7], [10] and [20]).

3.   Experimental

3.1. The UHV setup

After discussing the fundamental theoretical aspects of LEIS the apparent question is: What are the requirements of an experimental setup in order to obtain the chemical composition of the topmost surface layer of a solid sample? The following list should provide answers:

- Most importantly, sample preparation (sputtering, oxidation, reduction, heating) and LEIS measurement must be carried out inside the same UHV chamber. Adsorption of (residual) gas atoms and molecules has a significant impact on the surface composition[5] and must therefore be minimised.

- The proportionalities $A_i \propto \widetilde{N}_i$ and $A_i \propto R$ imply that measurements will have a better signal to noise (S/N)-ratio if the spot size of the He$^+$-ion beam scattered from the sample surface is as large as possible, whereas $A_i \propto \widetilde{N}_i$ and a negligible value of R are preferred. Higher values of A_i allow lower detection limits (or higher sensitivity) of species i consequently.

- Generally speaking, UHV setups are often constructed in a way that the sample is located in the centre of a chamber on a manipulator. Then, the acquired scattering angle θ in a LEIS experiment only depends on which flanges the ESA/multi channel plate detector (or TOF-MS) and the ion gun are attached to.[6] Transfer of momentum from a projectile ion to a surface atom directly correlates with mass resolution and reaches its maximum at $\theta = 180°$.[7] Simultaneously, the differential interaction cross-section is reduced to a minimum and that corresponds to a decreased scattering or detection intensity.[8,10] The literature does not give a conclusive recommendation for the choice of angles $90° < \theta < 180°$ in association with compositional analysis since this relies on

---

[5] At room temperature and a base pressure of e.g. 10^{-9} mbar a ML-coverage of 1 cm^2 of surface area by residue air molecules and atoms is given after $\approx$ 1 h. This estimation is made under the assumption that the sticking coefficient $s_i = 1$ for all respective species i. The time span is even much shorter for individual air components (e.g. O$_2$, H$_2$O).[43]

[6] Setups dedicated to angle-resolved experiments may have the ESA rest on a turntable to access a certain range of scattering angles.[44]

[7] Scattering at 180° is solely captured in case of a central single collision where the surface atom shows an impact parameter $x \approx 0$.[30]

the nature of the sample and whether or not mass resolution can be sacrificed in favour of a lower detection limit and better S/N-ratio (and vice versa).

- So far it was taken for granted that He$^+$-ions backscattered under discrete scattering angles are detected. In case of using an ESA, there is a solid acceptance angle $\Delta\theta$ which is given by the degree to which the iris slit is opened. Large values of $\Delta\theta$ trigger higher sensitivity but at the expense of mass resolution.[20] Also, if the source area (beam spot on the target sample) is bigger than the acceptance aperture only a fraction of backscattered He$^+$-ions is measured which lowers the detection efficiency.[20,30]

- A suitable ion source provides an ion beam of uniform kinetic energy and well-defined focus.

Further considerations are about to follow with regard to the actual UHV system employed for the experimental work of this thesis. The setup is schematically illustrated in Figure 3-15, which was constructed by SPECS based on the design-requests of our research group[45]. It comprises three sections that are accessible through a gateway system, based on specifically designed sample holders, locking mechanism and magnetically coupled transfer rods:

(a) Samples are introduced to and removed from the setup *via* a load lock.

(b) At its centre, the system features a preparation chamber. It is equipped with an xyzφ-manipulator on top with integrated electron beam heating which is surrounded by exchangeable tools for sample surface investigation, mounted on respective flanges. During the execution of this work it contained:

- a SPECS IQE 12/38 ion gun (for LEIS)

- a SPECS Phoibos 100 hemispherical electrostatic analyser (for LEIS and XPS) and XR 50 X-ray gun (with a non-monochromatic dual Al/Mg anode)

- a SPECS reverse view ErLEED 150 optics (for low energy electron diffraction, LEED; and AES)

- an electron beam evaporator and a quartz crystal microbalance (allowing precise physical vapour deposition (PVD) of metals in the sub-ML range)

- a sputter gun (for sample cleaning)
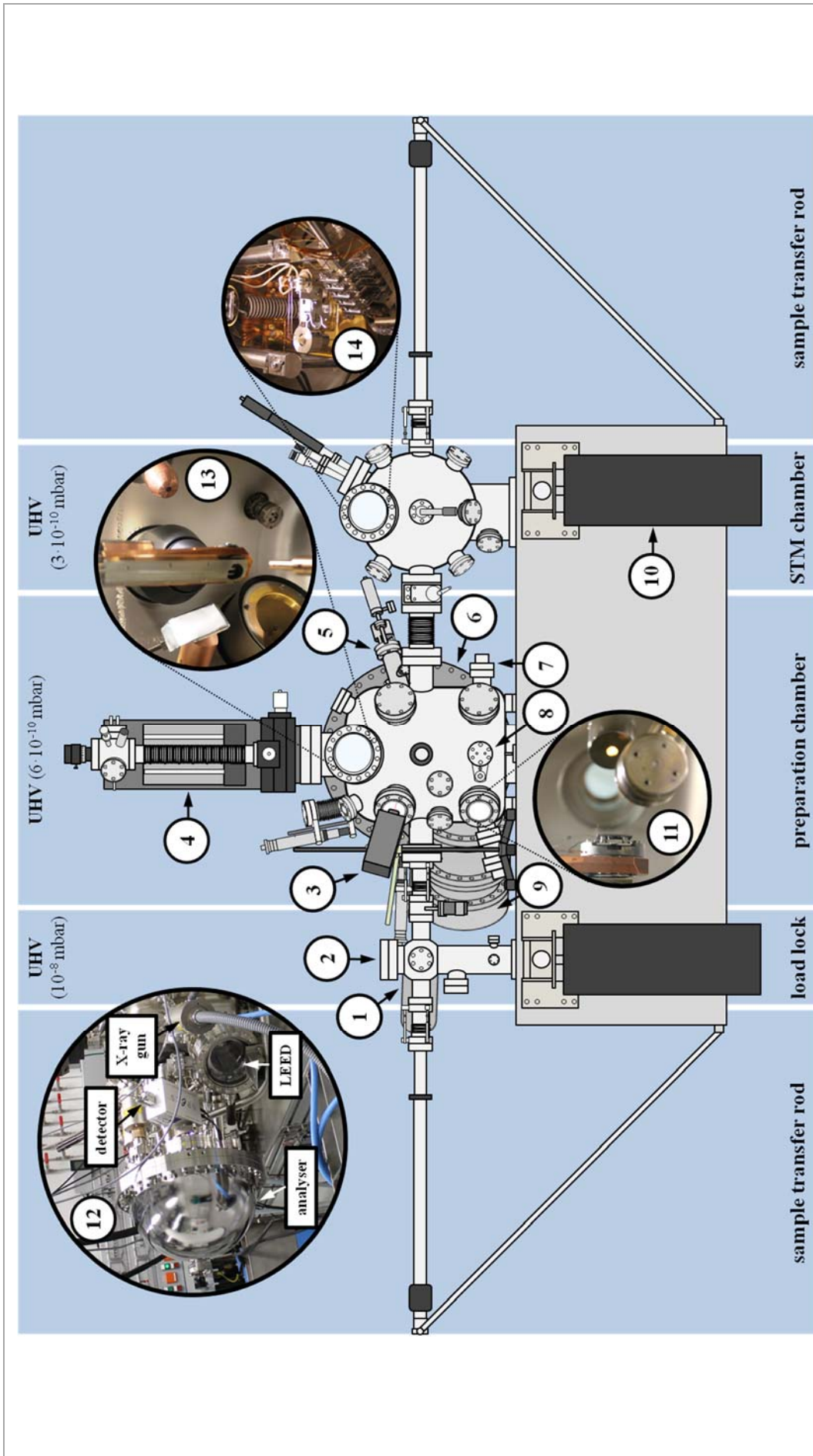
Experimental

Figure 3-15: Sketch of the experimental setup; 1) X-ray gun, 2) sample load, 3) pyrometer, 4) xyzφ-manipulator, 5) He$^+$-ion gun, 6) hemispherical analyser, 7) sputter gun, 8) microbalance, 9) LEED-optics, 10) LEED-optics, 11) air damper, 11) Ar$^+$-sputtering (microbalance in the foreground), 12) backside of the preparation chamber (XPS/LEED), 13) LEIS experiment (X-ray gun on the left with safety shield, lower part of the manipulator in the middle, He$^+$-ion gun on the right, ESA in the back, LEED-optics at the bottom left and electron beam evaporator at the bottom right), 14) STM

Both the ion and sputter guns have high-precision leak valves which were connected to a gas line (including a rotary vane pump) and supply of Ar, He, H_2, N_2, and O_2 – all of high purity (5.0), provided by Messer Austria. In addition to Ar, partial pressures of H_2 and O_2 were dosed through the leak valve of the sputter gun for reductive or oxidative sample pre-treatment.

(c)   Topographical images of sample surfaces at selected positions can be provided by a HT STM 150 Aarhus scanning tunnelling microscope (STM; see Figure 3-15, chamber on the right). The vibration-sensitive microscope is supported by an air damping system.

Sections (a) and (b) are evacuated by turbomolecular and scroll backing pumps, whereas at section (c) vibration-free Ti-sublimation and ion getter pumps are deployed (typical base pressures are indicated in Figure 3-15). Furthermore, the UHV setup is secured by an interlock system that would shut down all instruments for surface investigation if a pressure of $5 \cdot 10^{-6}$ mbar was exceeded. This is especially important for the performance of pre-treatments when Ar (sputtering), H_2 (reduction) and O_2 (oxidation) are dosed to the preparation chamber. Although a sample transfer system is generally very convenient as it avoids breaking the vacuum of preparation and analysis chambers when changing samples, it also comes with two significant drawbacks:

1)   The most reliable way to perform temperature measurements in UHV setups is through installation of a thermocouple connection. Suitable wires, typically supplied by the manipulator, are spot-welded to the sample and fed-through a flange for read-out purposes (in the simplest case by means of a digital multimeter).[46] This is relatively easy to do as long as the sample is fixed to the manipulator. However, for a locking system this presents a complicated challenge. SPECS installed a special design of a K-type thermocouple connection (Ni/NiCr) at the bottom of the manipulator. It would contact the sample holder by springy clips as soon as it is correctly slit into the intended groove (see Figure 3-16). Though, the elasticity of these clips causes the sample to move backwards and contact is lost if the manipulator is moved or the position of the clips with respect to the sample holder is not ideally arranged. In addition, with increasing lifetime of the thermocouple clips (influenced by repeated heating and cooling as well as oxidative and reductive sample treatments) the elasticity of the material is lost, causing further connection issues. These problems were documented in earlier experimental works[45] and therefore the clips had been removed. The reason

for reattaching the clips was to look for faults beyond their proper contact to the sample. After achieving a functioning arrangement of the connections, a test run (using a multimeter) was initiated and accompanied by an IMPAC 140 pyrometer (designed for metallic samples; temperature range: 300-1300 °C; spectral range: 1.45-1.8 μm). Unfortunately, it was found that the deviation between both temperature read-outs could not be matched by any emissivity setting of the pyrometer (available options: $0.1 \leq \varepsilon \leq 1$) or other measures. For this reason temperature measurements were solely conducted *via* the pyrometer (as indicated in Figure 3-15).
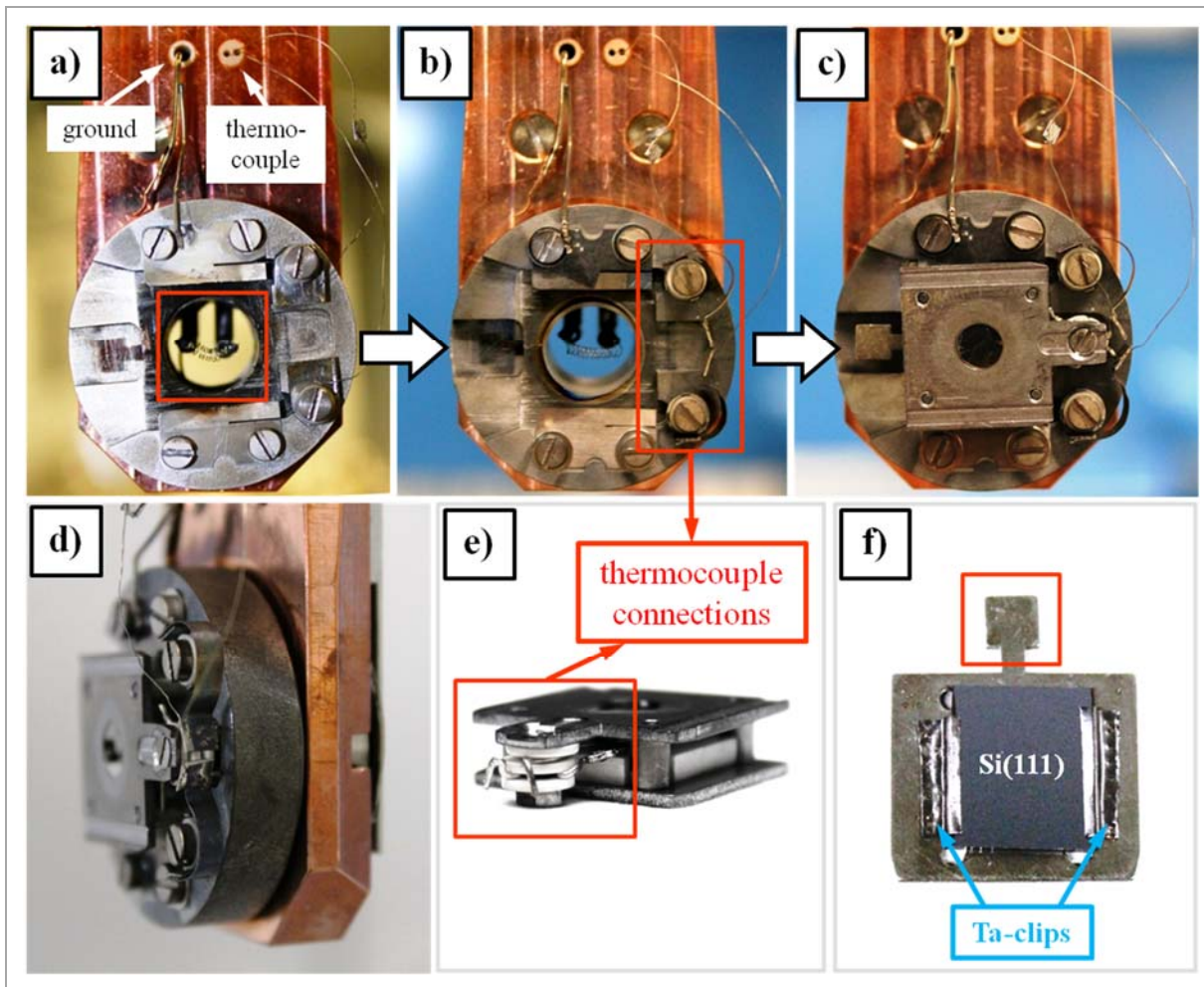
Figure 3-16: Images of the lower part of the manipulator (a)-d)) and sample holders (e) and f)) utilised for experiments; a) manipulator without thermocouple connections (marked red: electron beam heating, surrounded by isolating ceramics), b) springy thermocouple clips (marked red) added to the manipulator, c) manipulator with sample holder (single crystal in the centre), d) close-up of contacted thermocouple connections, e) close-up of thermocouple wires mounted onto the single crystal sample holder (with ceramic isolation disks), f) sample holder for metal foils (here with Si-wafer mounted by spot-welded Ta-clips; marked red: key-shaped

2)   Electron beam heating is implemented by application of electric current to a filament wire (here: made of thoriated W[8], thickness 0.1 mm; maximum current: up to 1.5 A), closely located to the backside of the sample (holder). Heat radiation originating from a glowing filament will be sufficient for reaching temperatures of a few 100 °C, depending on the distance between the filament and the sample, the thickness of the filament, its number of coils and the magnitude of applied current. If higher temperatures are required, then thermionic emission of electrons from the filament is achieved by an electric potential (here: in the range of 900-1000 V) and an electric field accordingly, induced between the sample and the filament. Electron impact leads to a much higher heating rate and maximum temperature. This method is only appropriate as long as it is used to heat the sample after sputtering for the purpose of annealing. Reductive as well as oxidative sample treatment by means of H_2- or O_2-partial pressures during heating will affect the chemical constitution of the filament, and thus diminish the maximum temperature and its life span. In association with LEIS experiments, electric fields that occur outside the ion gun or the ESA may falsify desired results. This is especially the case if the (metallic) sample acts as positive pole of the electric field, as within the electron beam heating, which leads to additional Coulomb repulsion of He^+-ions from the sample surface. Since other surface investigation methods are also negatively affected, electron beam heating is restricted to sample preparation.[48] The only alternatives would be resistive, inductive or laser heating. Therefore, LEIS measurements were exclusively conducted at room temperature.

The list, started at the beginning of this chapter, is amended as follows:

- Sample preparation and LEIS experiments were executed consecutively inside the same preparation/analysis chamber.
- Reference metal foils (mounted on a simple sample holder, shown in Figure 3-16, f)) and a $Pt_3Zr(0001)$ single crystal (fixed to a "sandwich sample holder", demonstrated in Figure 3-16, e) and Figure 3-17) were utilised as LEIS targets.

---

[8] During the heating process Th is segregating to the surface.[47] Although the work function of a material is an anisotropic feature it is reported in the literature that the work function of Th is roughly more than 1 eV lower than that of W.[48,49] As long as pure Th is covering the surface of the utilised filament thermionic emission is enhanced. Having said this, Th shows great tendency to form ThO_2.

- The ESA and ion gun were attached to neighbouring flanges, enclosing an angle of $\gamma = 45°$ (see Figure 3-26). Therefore, the scattering angle θ is 135°.

- The ESA was operated in transmission mode "large area" and its iris slit fully opened which results in a maximum acceptance angle of $\Delta\theta = \pm 5°$.[51] This benefitted the sensitivity of measurements, especially considering the small size of the single crystal, albeit at the expense of mass resolution.

- The SPECS IQE 12/38 ion gun does not contain a Wien filter. Therefore, the gas line had to be rinsed multiple times with He before starting any experiments (for explanation see section 3.3).
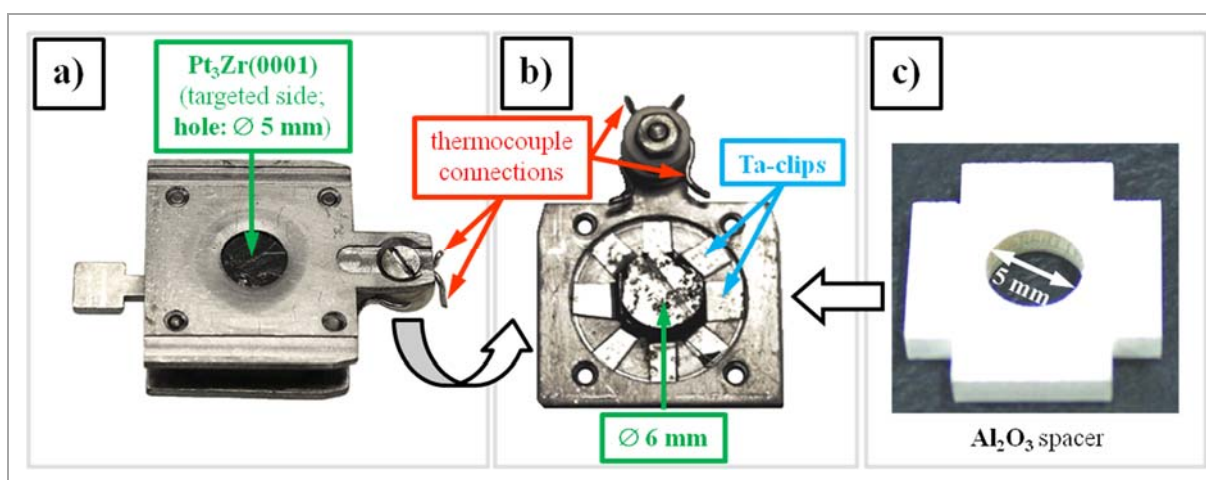
Figure 3-17: "Sandwich sample holder" for $Pt_3Zr(0001)$; a) front side of the assembled sample holder, b) flipped backside of the removed upper Mo-plate including the single crystal, kept in the centre by Ta-clips (spot-welded to the plate), c) ceramic spacer[45]; the crystal is accurately held in the centre by the Ta-clips and spacer, whereas the second plate (the bottom one in a)) also has a hole in the middle so that the crystal can be heated from the backside by the electron beam heating

3.2. Sample and reference materials

As noted in chapter 1, the determination of the chemical composition of alloy surfaces is particularly important if these serve as well-defined substrate for the growth of ordered oxide thin film supports for catalytic model systems[52]. In this context, the superalloy[9] Pt_3Zr (its hexagonal unit cell is shown in Figure 3-18, a)) has been studied extensively over the past years, using a $Pt_3Zr(0001)$ single crystal.[52-56]

---

[9] Superalloys are characterised by extraordinary mechanical, thermal and/or chemical stability. Pt_3Zr is both a superalloy as well as an intermetallic compound.[52,54]

The goal of these studies was to develop a specific high-temperature oxidation treatment under UHV, during which Zr from the top monolayers is consumed in forming an ultrathin ZrO_2 (zirconia) film[10]. Such a film, after deposition of e.g. Ni nanoparticles, then serves as a model for a solid oxide fuel cell (SOFC) anode.[53]

Zirconia is a non-reducible and insulating oxide whose bulk and thin film properties turned out to be different, however.[57] For surface science studies, thin oxide films are desired because they hardly reduce the electric conductivity of the substrate, which makes the oxide accessible to electron-based investigation methods (e.g. STM or XPS). The synthesis of such thin films is very difficult to achieve by common techniques, such as PVD, due to the very low vapour pressure of metallic Zr at its melting point and the tendency of forming disordered films of bulk zirconia.[56] Thus, a more effective route is to employ a Pt-Zr alloy that features a lower concentration of Zr which is available for oxidation at elevated temperature, and a higher concentration of an oxidation resistant element (such as Pt).[54] In that way, the availability of Zr at the surface is evenly distributed and its amount depends on mass transport/diffusion – both factors which promote ordered thin film growth.

---

[10] This film comprises of a single O-Zr-O trilayer, featuring metallic bonds (Zr-Pt) to the substrate alloy and a crystal structure which is similar to cubic $ZrO_2(111)$.[53]
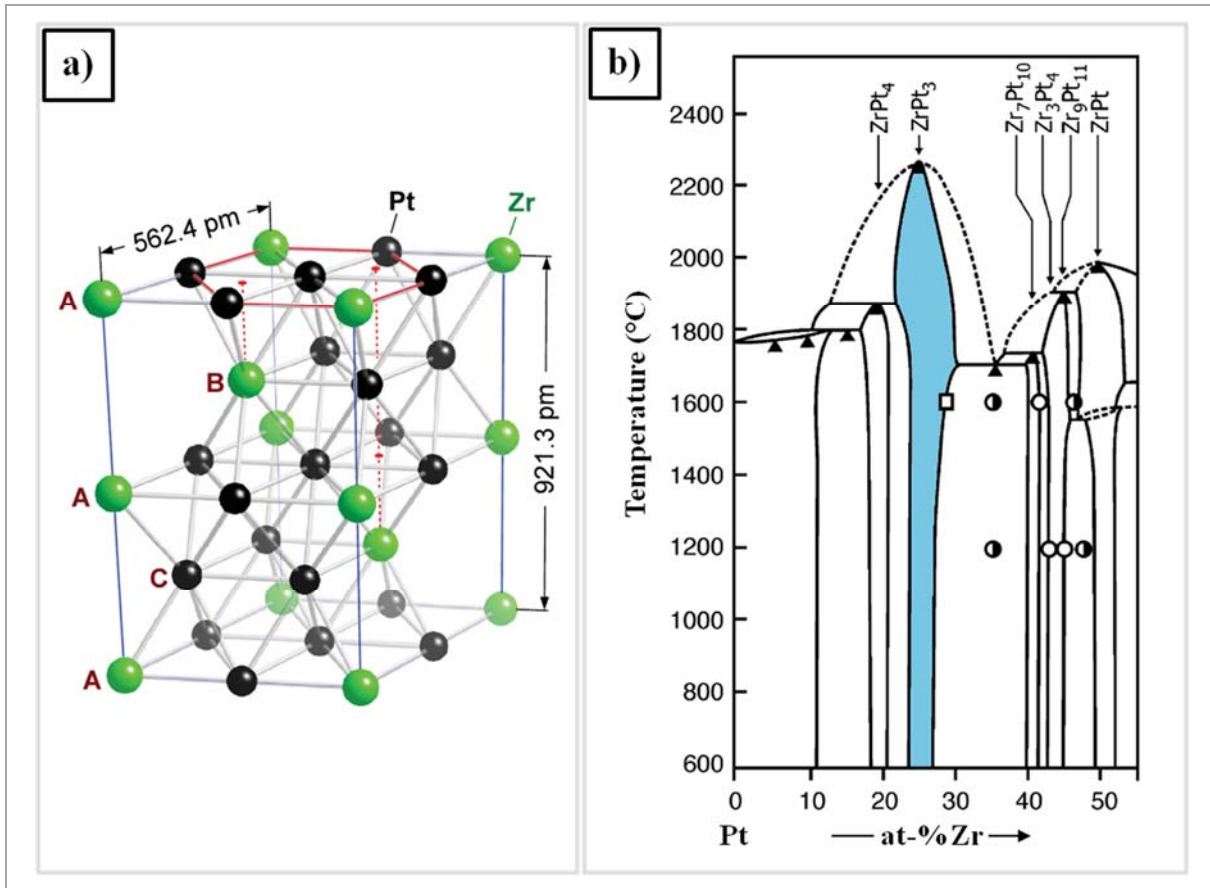
Figure 3-18: a) Hexagonal unit cell of Pt$_3$Zr(0001), Ni$_3$Ti-type, featuring ABAC stacking along [0001][54] and b) Pt-rich section of the binary phase diagram of Pt and Zr[58] (the intermetallic compound Pt$_3$Zr is highlighted blue; marker symbols: ▲ = melting onset upon heating ,□ = composition was determined by energy dispersive spectroscopy (EDS) ,◐ = two-phase alloy ,○ = single-phase alloy)

Although the strong bonds between Pt and Zr in Pt$_3$Zr[54] lead to a high melting temperature of up to 2250 °C[58] (at 1 bar) and chemical stability, it is reported that this material exhibits poor ductility at room temperature, i.e. brittle behaviour (which is enhanced if treated with H$_2$)[59]. Consequently, the single crystal that was originally used by the research group for earlier experimental studies was in very poor (partly disintegrated) condition at the start of this thesis. Therefore, a slightly bigger, circular-disk-shaped spare crystal (see Figure 3-17; diameter: 6 mm, thickness: 2 mm, geometry: K004[60]), which had never been used before, was chosen (imaged in Figure 3-19).
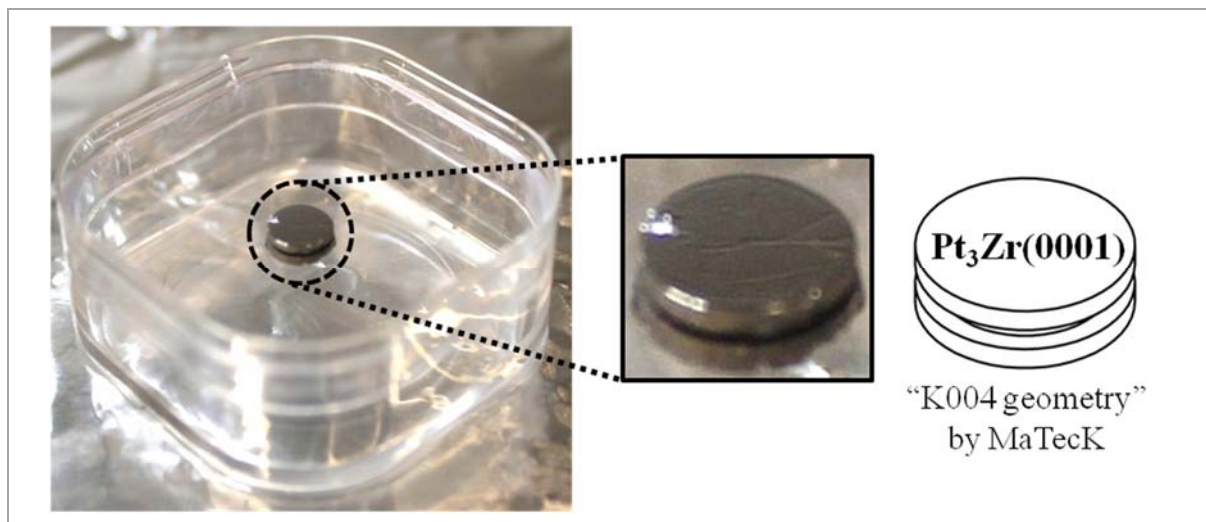
Figure 3-19: New Pt$_3$Zr(0001) single crystal (note: The dent in the front side of the unused crystal and the crooked backside, shown in Figure 3-17, give a clear impression of the crystal's brittleness.)

The growth of this single crystal was carried out by MaTecK *via* the zone melting technique in a mirror furnace under inert gas (Ar), on the basis of Pt and Zr metal powders of technical purity.[29]

In the course of growing the mentioned ultrathin zirconia film on Pt$_3$Zr(0001) 0.64 ML of Zr are removed from the topmost surface layer.[54] Thus, the correct stoichiometry and a clean surface are crucial pre-conditions for successful thin film preparation. Quantification of LEIS measurements, performed on this single crystal, can be achieved if appropriate reference materials (elemental standards of highest purity) are studied under the same experimental conditions. The most suitable reference materials for Pt$_3$Zr(0001) are Pt and Zr single crystals with well-defined atomic surface densities $\widetilde{N}_i$. Since these are rather expensive, high-purity polycrystalline metal foils were used. Needless to say, this approach is more convenient but may involve an error of up to 20 % (caused by many different crystallographic orientations and macroscopic roughness).[20]

In addition to Pt and Zr, also a Ni foil was measured, in order to study Ni nanoparticles grown on the zirconia thin film. Table 3-1 summarises information on the purity of the foils, as provided by the respective supplier.

Table 3-1: Polycrystalline reference foils

Element	Manufacturer	Purity (wt-%)	Impurities (ppm)
Pt	Goodfellow	99.99+[62]	Ag: < 1 Au: 1 Ca: < 1 Cu: 1 Fe: 3 Mg: 1 Pd: 1 Si: 5
Zr	Goodfellow	99.2[63]	C: 250 Hf: 2500 Fe: 200 Cr: 200 N: 100 O: 1000 H: 10
Ni	Alfa Aesar	99.994[64]	S: < 1 C: 6.5 N: 1.5 O: 19 Ta: < 1

As already shown in Figure 3-16, f), the reference foils were mounted onto Mo-sample holders by spot-welded Ta-clips (Advent Research Materials, thickness 0.05 mm and 0.1 mm, purity 99.9 wt-%, depicted in Figure 3-20).
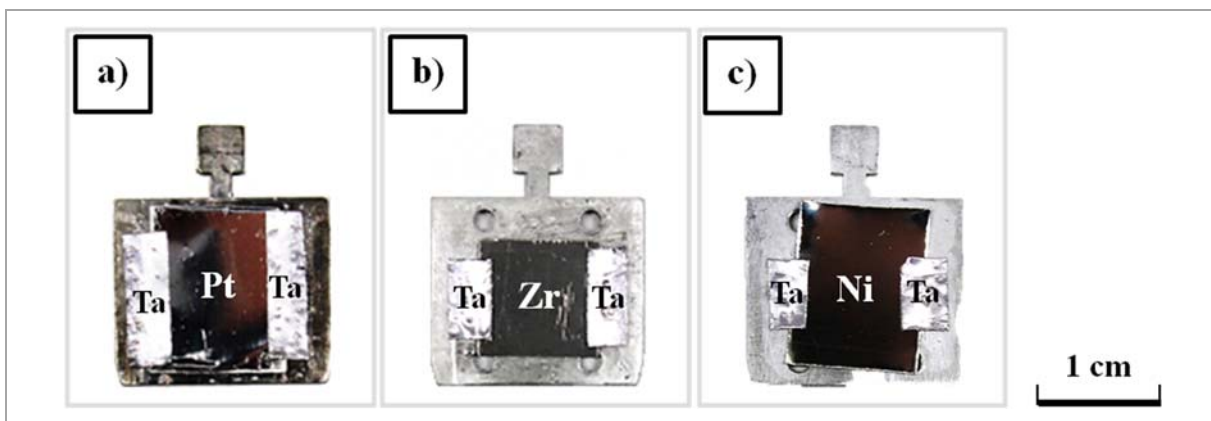
Figure 3-20: Polycrystalline reference foils, mounted onto Mo-sample holders: a) Pt, b) Zr, c) Ni

3.3. Adjustment of geometric settings for LEIS experiments

Apparently, the He⁺-ion beam should match the dimension of the "probe hole" (diameter: 5 mm) in the upper Mo-plate of the sample holder (displayed in Figure 3-17). The hole is closed by the single crystal from the backside and therefore represents the available sample surface area. It is also apparent that the sample must be put to an exact position, determined by the ion gun and the analyser arrangement. This position also depends on the spatial configuration of the manipulator and some "tuning" is thus required. Only then, the sensitivity of LEIS measurements of $Pt_3Zr(0001)$ is optimised and the corresponding geometry is retained for all other scattering experiments. Nevertheless, this is a challenging task because:

(a)   The He⁺-ion beam is invisible for the human eye.

(b)   It is tricky to optimise both the correct spot size and spot position.

It is important to emphasise that the "sandwich sample holder" (including $Pt_3Zr(0001)$) was not suited to tackle this problem (although it seems obvious to work with the actual target) because the mass resolution does not suffice to fully separate the signals of Pt and Mo. This could not be avoided by increasing the primary energy of He⁺-ions, since this has an effect on various beam parameters. Thus, the only alternative was to design a specific target for adjustment.

The first attempt directly addressed to visualise the ion beam by using a target material which exhibits collision-induced photoluminescence and thereby shows the beam spot. ZnO nanoparticles[65] and thin films[66] are known for stimulated fluorescence emission in the blue, shortwave end of the VIS-spectrum. The defect concentration in ZnO is directly correlated with the fluorescence intensity.[67] Deposition onto a substrate that features different lattice parameters causes a lattice mismatch and increases the amount of defects in ZnO.[66] Furthermore, attenuation of fluorescence emission is reduced by deploying a transparent substrate. For these reasons, a ZnO thin film was deposited *via* PVD onto a sapphire sheet (Goodfellow; thickness: 0.5 mm, size: 10×10 mm², purity: 99.9 wt-%) at room temperature and mounted as displayed in Figure 3-21. Additional defects were created by sputtering for 3 s (at $5 \cdot 10^{-6}$ mbar Ar, 0.5 kV acceleration voltage and room temperature).
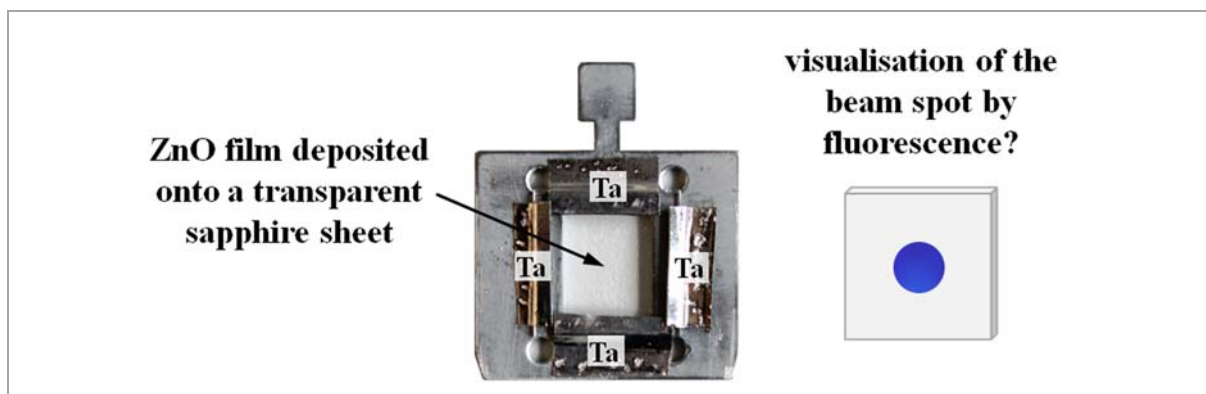
Figure 3-21: Sample holder with square-shaped window: sapphire sheet (single-crystalline Al_2O_3) with ZnO film, deposited by PVD of metallic Zn under high vacuum (HV) at room temperature, mounted *via* Ta-clips.

Blue fluorescence was observed but its intensity was not sufficient to allow for a proper setting with the current layout of windows and manipulator in the UHV system (i.e. a direct view onto the sample holder from the backside would have been necessary, but was blocked by the sample holder).

Although there is room for improvement[68] in terms of red-shift of fluorescence emission, it turned out to be much easier to create a "target model" mimicking the sample surface that is hit by the He^+-ion beam. For that purpose, polycrystalline Au and Cu foils (Goodfellow; thickness: 0.125 mm Au, 0.1 mm Cu; size: $\approx 10 \times 10$ mm^2, purity: 99.99+ wt-%) were used. The Cu foil with a 5 mm in diameter hole was put on top of the Au foil. Both foils were mounted and centred by Ta-clips, spot-welded to the sample holder. Figure 3-22, b) demonstrates the design, as well as the single crystal sample holder (a)). The trick is to get LEIS spectra of only Au and not Cu, by proper adjustment of the sample position and ion beam spot size.
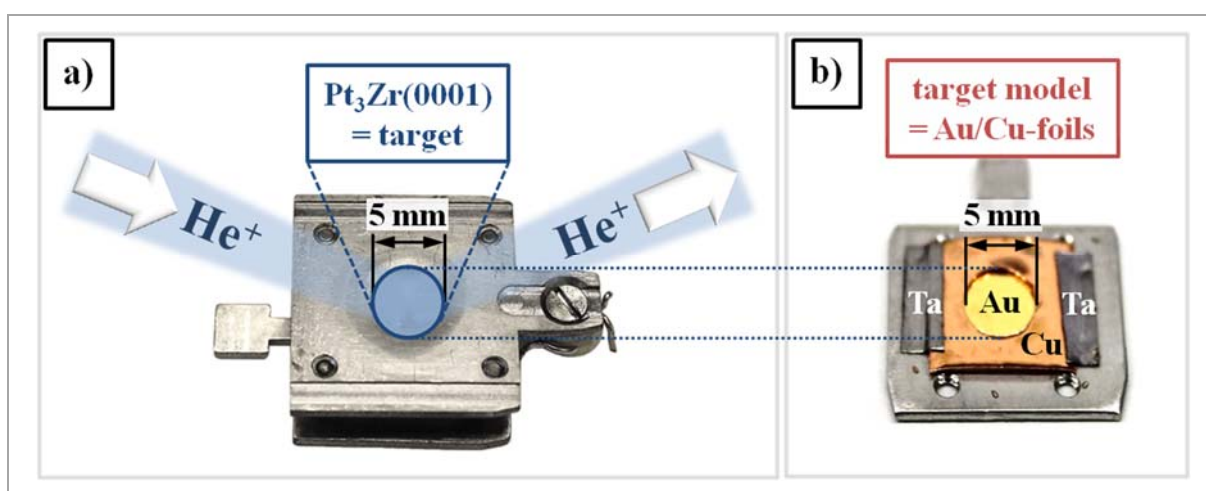

Figure 3-22: He^+-ion beam adjustment: modelling the desired spot size (a)) by a Au/Cu-target (b))

Before starting the positional adjustment of the target model and tuning of the ion source three pre-treatment cycles, explained in Figure 3-23, were performed.
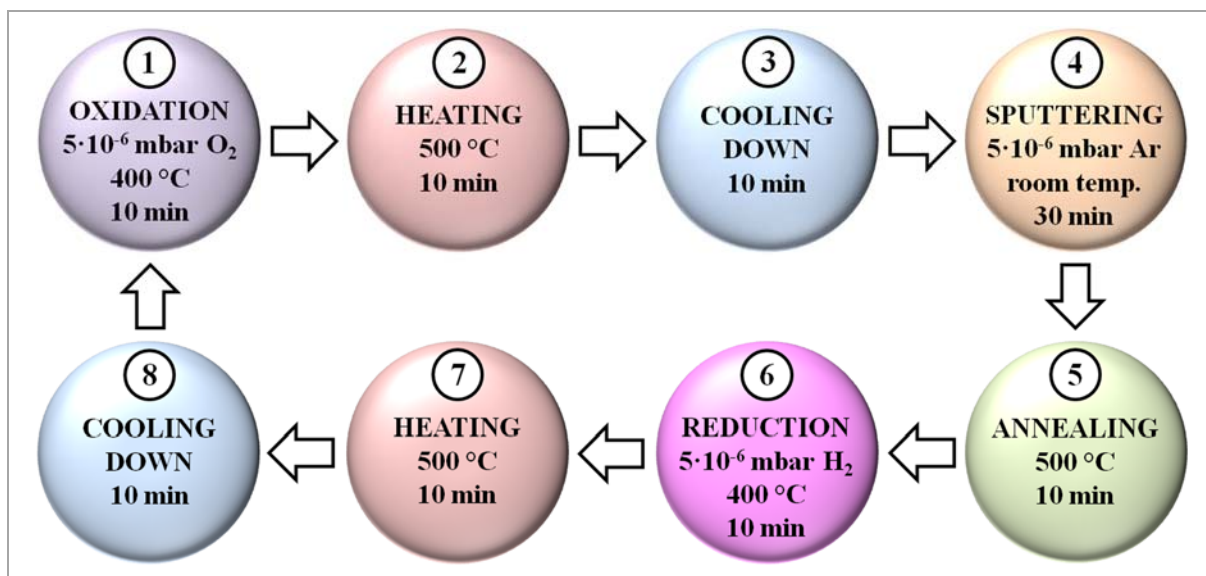
Figure 3-23: Pre-treatment cycle of the Au/Cu-target: all gases were supplied by the leak valve attached to the sputter gun and the gas line was rinsed three times with Ar before introducing a new gas; steps 2 and 7 were conducted while pumping down to a base pressure in the 10^{-9} mbar regime for desorption of reactive species

The SPECS IQE 12/38 (detailed illustration see Figure 3-24) is an extractor type, scanning ion source which uses a thoriated Ir ring filament to ionise He by electron bombardment.[69]
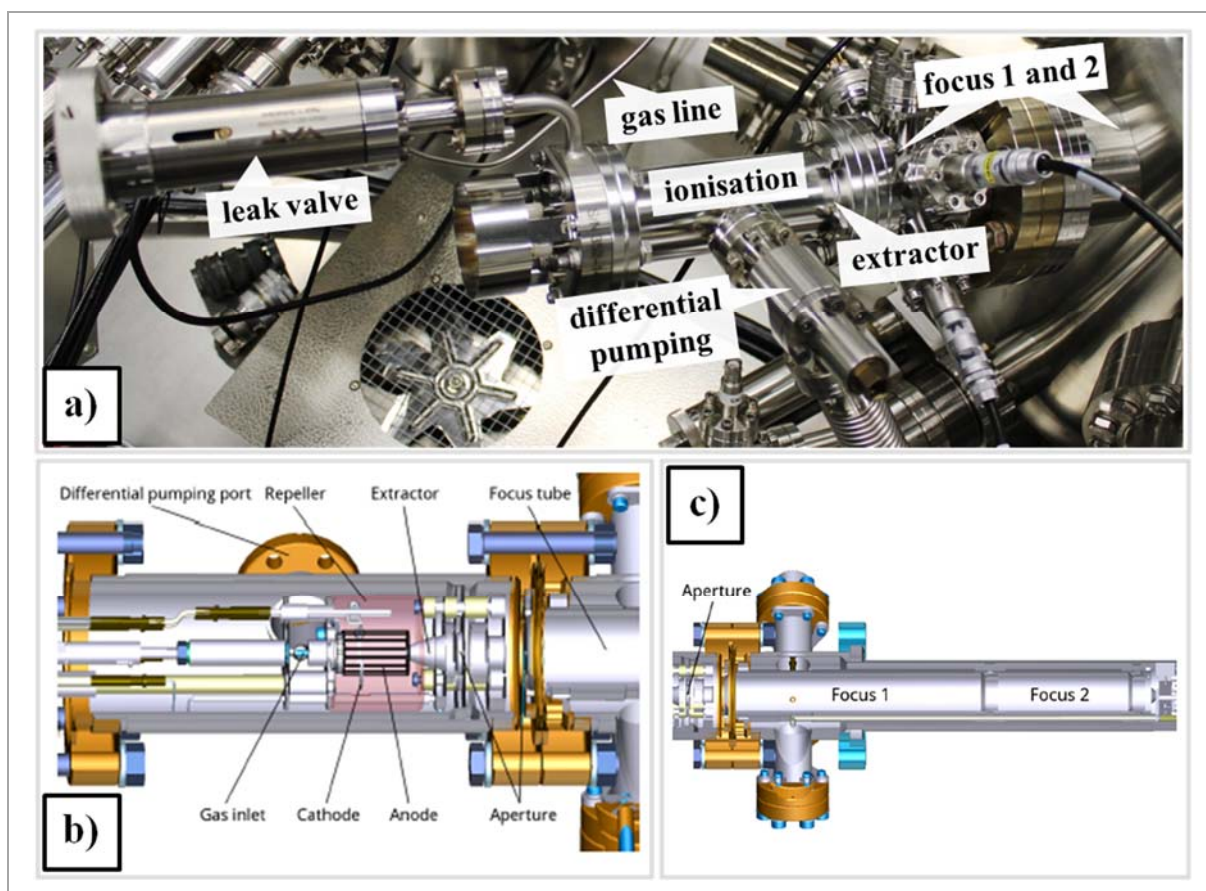
Figure 3-24: SPECS IQE 12/38: a) image of the ion gun, attached to the preparation chamber, b) ionisation compartment of the ion gun, including the extractor[70], c) electrostatic focus lenses 1 and 2[70]

The filament compartment is differentially pumped by the load lock pumps. The generated He$^+$-ions are extracted and accelerated to a kinetic energy of 1 keV.[11] Two electrostatic lenses allow changing the spot size and fine-tuning the spot position.[12]

The control software of the IQE 12/38 offers two modes of operation: a "high current mode" for maximum beam current, if spot size is irrelevant, and the "fine beam mode" that allows focussing the beam down to a small point. The manufacturer's specifications for the "fine beam mode", which was chosen, regarding spot size and ion current for a given kinetic energy are only valid for a standard working distance between ion source and sample of 23 mm.[71] If the manipulator of the preparation chamber (diameter: 350 mm) is in its default centre position, the distance between the aperture of the ion gun and the single crystal is approximately 133 mm. From the sample to the entrance slit of the ESA the distance is 61 mm (in case of metal foils roughly 4 mm have to be added to these values).

Therefore, it was not possible to work with factory settings and the beam alignment was done manually. The manipulator, holding the Au/Cu-target, was set to a position in front of the entrance slit of the ESA where the sample would be ideally located for XPS measurements. Then, the sample holder was moved backwards, away from the ESA by roughly 20 mm, and turned by $\varphi = 45°$ in direction of the ion source. A He partial pressure of $2 \cdot 10^{-7}$ mbar was dosed to the preparation chamber by the high-precision leak valve, attached to the ion source. An acceleration voltage of 1 kV was applied. The iris slit of the ESA was fully opened and a first survey LEIS spectrum, using the "large area" mode of the ESA, was acquired with a scan range of 150-1010 eV. Therein, a small Au-peak at 903 eV could already be observed (see blue region spectrum in Figure 3-25). Subsequently, the beam width was tuned stepwise. The best/smallest ratio obtained for the (decreased) Cu-intensity (at 780 eV) and (increased) Au-intensity is reflected by the green region spectrum in Figure 3-25. Since the ratio between the two signals was not satisfactory, the analyser was set to "fixed energy transmission", so that only He$^+$-ions at a kinetic energy of 903 eV would pass. Then, the manipulator position was slightly changed in x- and y-direction (planar axis) within the arranged z-plane (height axis) as well as turned in direction of the ESA until the highest intensity of the Au-signal was achieved.

---

[11] A Wien filter would have assured a uniform kinetic energy as well as a (isotope-)pure ^{4}He$^+$-ion beam through its perpendicular electric and magnetic fields.

[12] It would be a tremendous improvement if the ion source offered a laser beam (like a simple laser pointer which is also found in the IMPAC 140 pyrometer) for much easier positional adjustment of the sample.

After some fine-tuning of the beam spot size (final setting of the ion gun: 3.5×3.5 mm^2) and focus parameters, the ideal Au/Cu-intensity ratio was found and plotted as the red region spectrum in Figure 3-25.
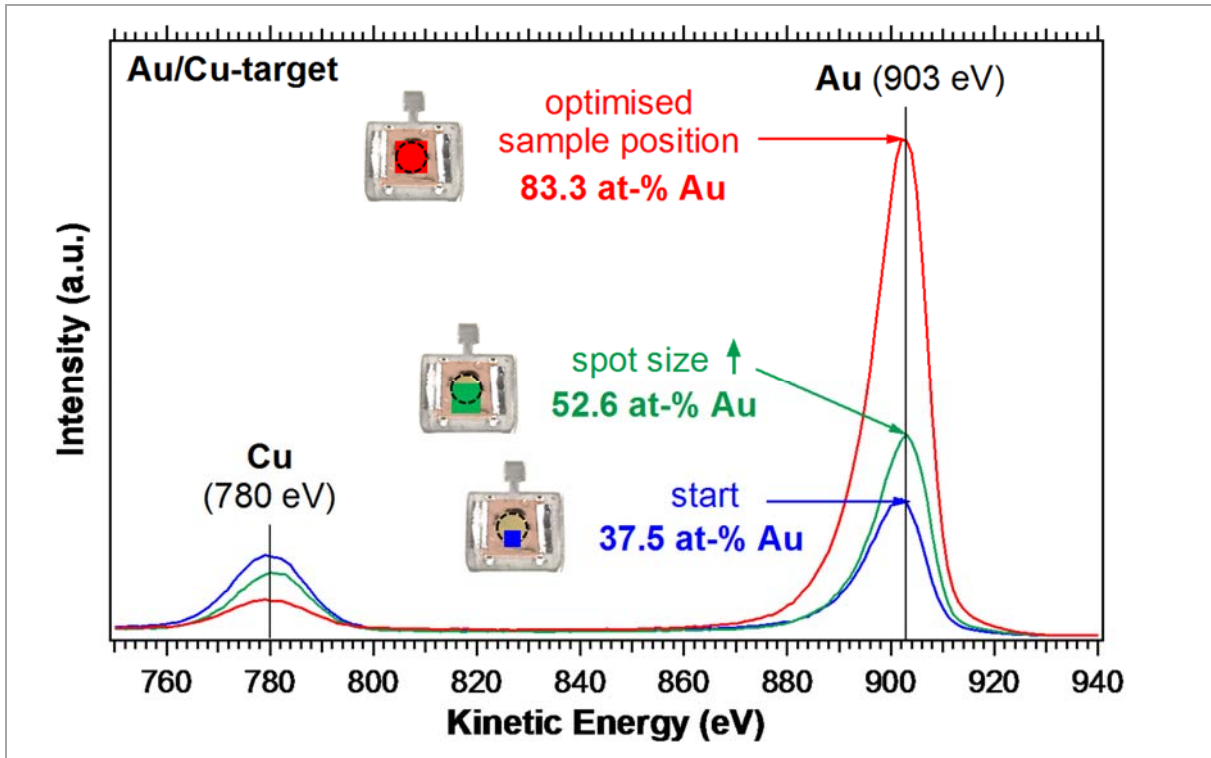

Figure 3-25: LEIS region spectra of the Au/Cu-target

Quantification, indicated in Figure 3-25, was executed by applying equation (2.17). Thereby, the areal atomic densities $\widetilde{N}_{Au}$ and $\widetilde{N}_{Cu}$ had to be disregarded since polycrystalline foils were utilised. Figure 3-26 represents a schematic drawing of the final geometric settings which were kept for all following LEIS experiments. These were validated by transferring the single crystal sample holder, containing Pt$_3$Zr(0001), by changing the position and detecting an increase of signal intensity, attributed to Mo from the sample holder.
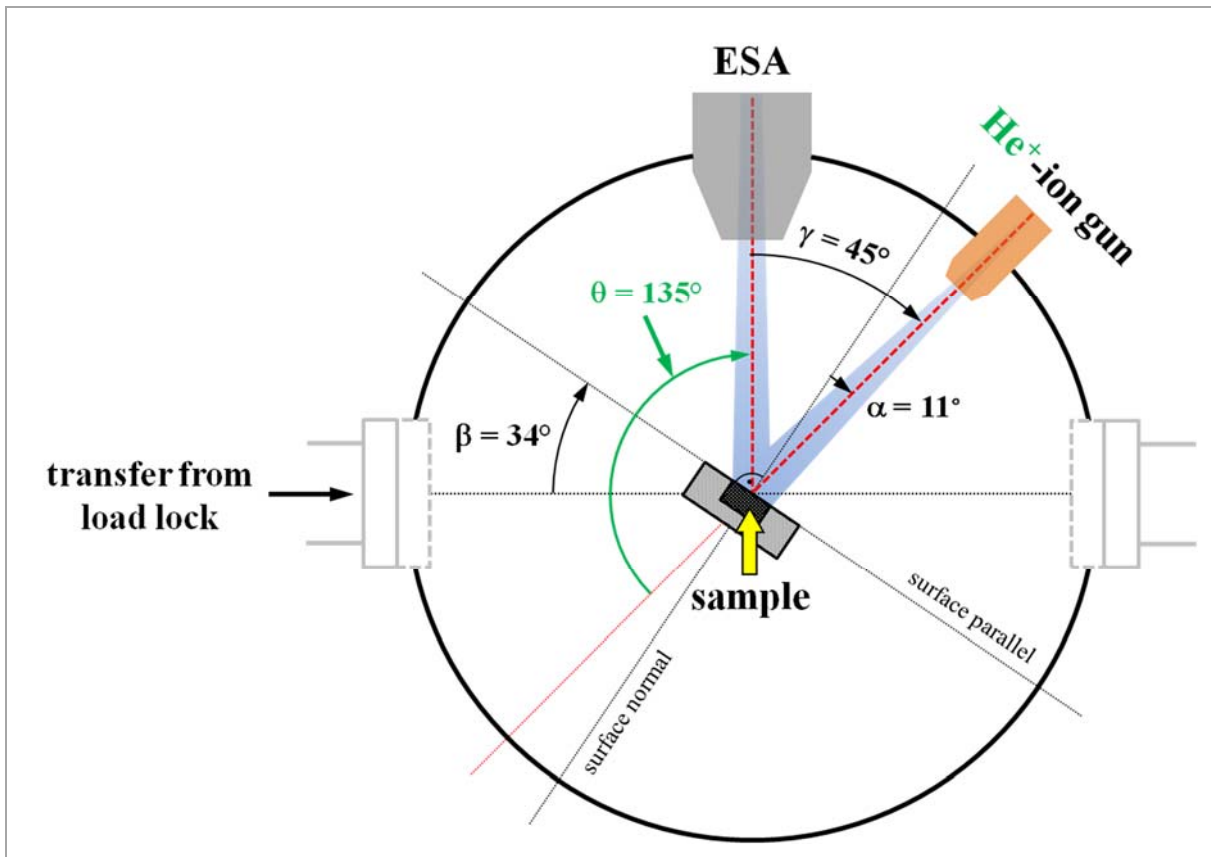
Figure 3-26: Geometric arrangement of LEIS experiments conducted inside the preparation chamber (top view); α = incident angle, β = reflection angle (α and β given with respect to the sample surface normal), γ = angle enclosed by the ion gun and ESA ($\alpha + \beta = \gamma$), θ = scattering angle ($\theta = \pi - \gamma$)

4. Results

For characterisation of reference metal foils Pt, Zr and Ni, and the Pt$_3$Zr(0001) sample, presented in chapter 3.2, LEIS and subsequent XPS experiments were conducted. Prior to that, multiple cleaning cycles that involved sputtering, annealing, oxidation and reduction were performed for all materials. While pre-treatment cycles for metal foils were based on common procedures, found in the literature, the Pt$_3$Zr single crystal was prepared as reported in earlier publications by the research group and colleagues from the Institute of Applied Physics.[52-54] At this point it has to be emphasised that reductive H$_2$ treatment at elevated temperature had to be avoided due to the tendency of Pt$_3$Zr(0001) for hydrogen embrittlement (mentioned in chapter 3.2). Universally employed experimental parameters for LEIS and XPS experiments are summarised in Table 4-2 and Table 4-3 (see following pages).

The scan range in LEIS experiments (given in Table 4-2) was in the lower end limited by a kinetic energy of 150 eV because of a significant increase of background signal. This is caused by unspecific scattering from the preparation chamber (and probably also includes emitted Auger electrons). Unfortunately, in some cases the intensity of the background covered up signals of single elastic collisions between He$^+$-ions and C, expected to appear at a kinetic energy of 305 eV at the given experimental parameters, which marks the elemental detection limit.

As described above, temperature measurements were carried out by a pyrometer. In order to do so, the emissivity of the employed metal foils and Pt$_3$Zr(0001) must be known and be within a range that is configurable (see chapter 3.1). Relevant tables are supplied by the manufacturer[72] and others and include useful parameters for polished Au, Cu, Pt and Ni foils (for pure Zr see [73]) which are roughly in the range of $\varepsilon \leq 0.1$. Since the lowest ε-value that can be applied is 0.1, an emissivity $\varepsilon < 0.1$ would mean that the actual temperature was higher than the measured one. In case of Pt$_3$Zr(0001), the emissivity parameter is unknown (to MaTecK[29], as well as to the literature). Although there are several methods to experimentally determine an unknown emissivity of a sample[74], the only way it could have worked was to install a thermocouple (shown in chapter 3.1) – which did not work out in our experiments.

Table 4-2: LEIS parameters

Ion gun	Acceleration voltage (kV)	1.000
	He partial pressure (mbar)	$2 \cdot 10^{-7}$
	Beam scanning width (mm^2)	3.5×3.5
	Beam position	default
	Emission current (mA)	10
	Extractor (%)	75.34
	Focus 1 (%)	70.00
	Focus 2 (%)	95.00
	Distance gun/sample (mm)	≈ 134 (metal foils) ≈ 130 (Pt$_3$Zr(0001))
ESA	Mode	High angular dispersion
	Scan range (kinetic energy, eV)	150-1010
	Entrance slit	5:7×20
	Iris slit	50
	MCD calibration	"wien_28-01-15"
	Step size (eV/dot)	1 (survey scans) 0.1 (region scans)
	Dwell time (ms/dot)	0.1
	Lens mode	Large area
	Energy pass (eV)	50
Positional arrangement	Scattering angle θ	135°
	Incident angle α	11°
	Reflection angle β	34°

Table 4-3: XPS parameters

X-ray anode	Radiation	Al K$_\alpha$ (1486.61 eV)
	Power (W)	200
	Acceleration voltage (kV)	12.50
ESA	Mode	High angular dispersion
	Maximum scan range (binding energy, keV)	1.500
	Entrance slit	5:7×20
	Iris slit	7.5-10
	MCD calibration	"wien_28-01-15"
	Step size (eV/dot)	1 (survey scans) 0.1 (region scans)
	Dwell time (ms/dot)	0.1
	Lens mode	Large area
	Energy pass (eV)	50 (survey scans) 20 (region scans)
Positional arrangement	X-ray anode/ESA	≈ 54.7° ("magic angle")
	Electron take-off angle ϑ	0° (for AR-XPS: 0°-40°)

It was not possible to measure the ion current between the ion source and the sample which occurred during LEIS and Ar-sputtering. For the latter, besides an acceleration voltage of 1.5 kV and filament emission current of 6 mA, positional settings, documented in earlier experimental reports, were used. XPS survey spectra demonstrated that samples were cleaned upon sputtering. Further support is provided by the fact that the front plate of the single crystal sample holder, surrounding the crystal, appeared "shiny" after some sputtering treatments (depicted in Figure 4-27) which was definitely not the case at the start of this thesis.
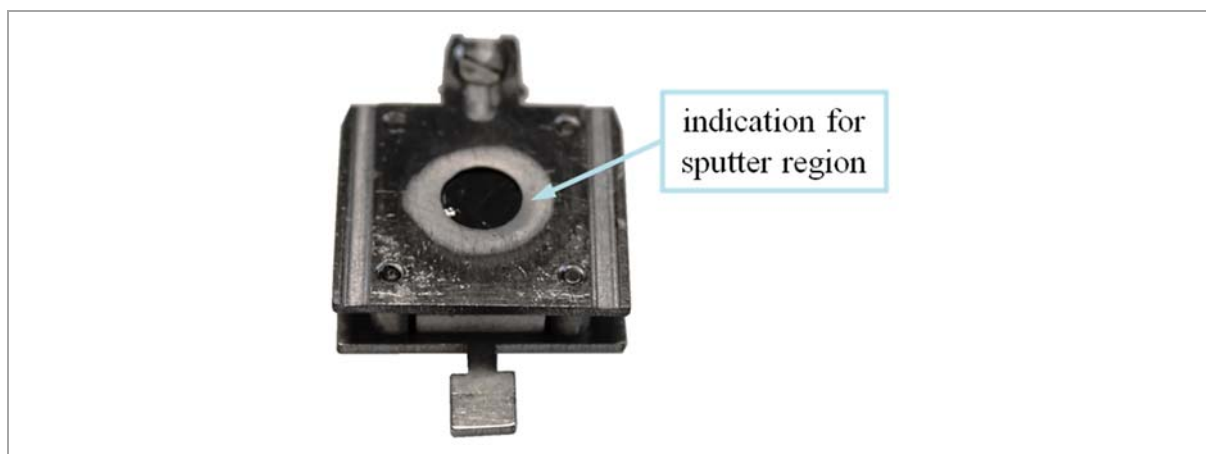
Figure 4-27: Polished circular area surrounding the single crystal after various pre-treatment cycles

The obtained XPS and AR-XPS scans were calibrated using the C 1s signal of graphitic (sp²-hydridised) carbon as internal standard, which is widely known to appear at a binding energy of 284.8 eV[75] (with the exception of the Ni foil where no C was found after the pre-treatment). In addition, the position of the Fermi edge of the valence band was examined which is by definition located at a binding energy of 0 eV after calibration.

4.1. Reference material: polycrystalline Pt foil

Preceding the LEIS and XPS measurements the pre-treatment cycle, illustrated in Figure 4-28, was conducted two times.
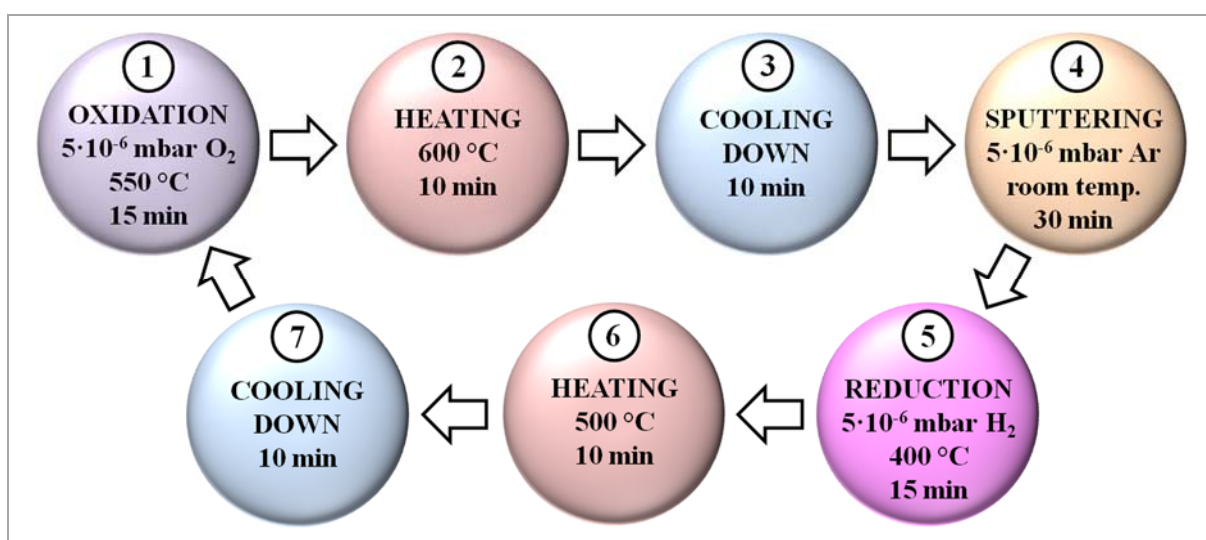
Figure 4-28: Pre-treatment cycle of the polycrystalline Pt foil

Herein, steps 2 and 7 were performed while pumping down to a base pressure in the lower 10^{-9} mbar regime in order to desorb reactive gases from the surface of the foil. Afterwards, the LEIS spectrum, shown in Figure 4-29, was obtained.
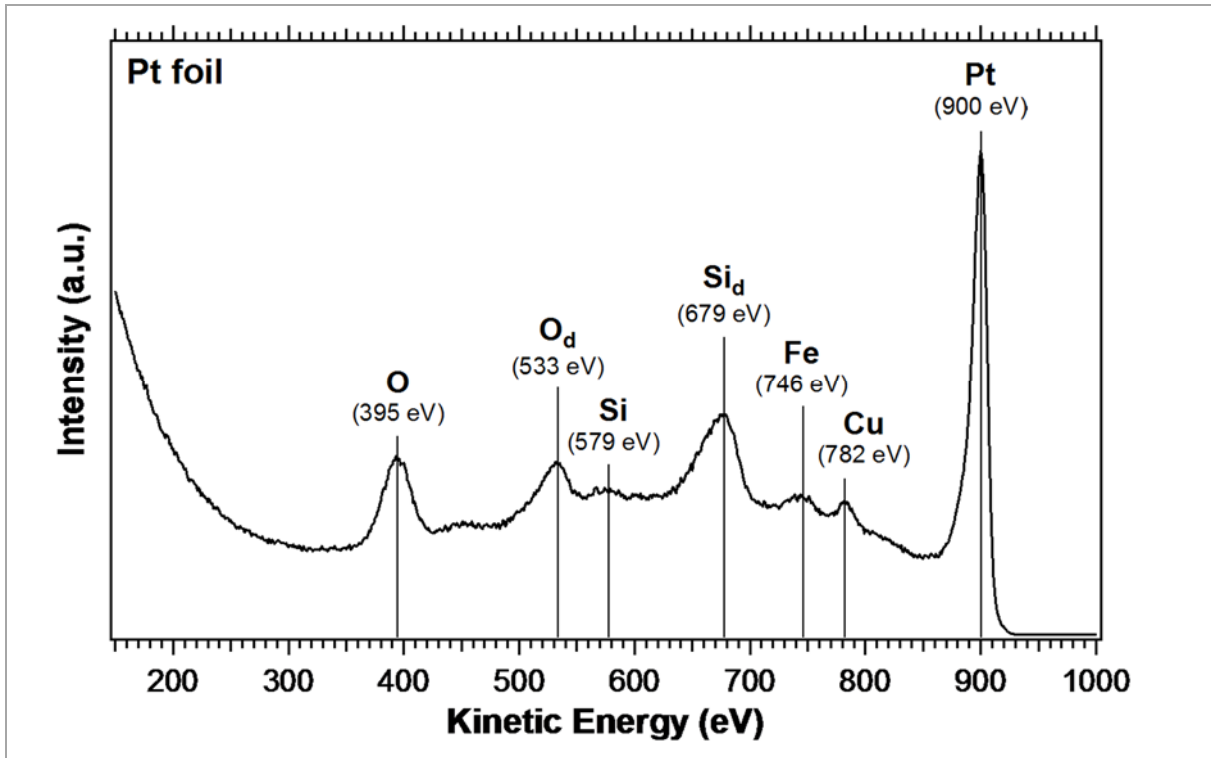
Figure 4-29: LEIS survey spectrum: polycrystalline Pt foil after cleaning

The following table compares the measured signals to calculations, based on equation (2.7). The index "d" stands for "double collision".

Table 4-4: Summary of signals, found in the LEIS spectrum of the Pt foil; measured and calculated values are opposed

Detected species	Measured kinetic energy E_1	Calculated reference kinetic energy E_{ref} (eV)	Shift of kinetic energy $(\Delta E_1 = E_1 - E_{ref}, eV)$
O	395	417	−22
O$_d$	533	534[76]	−1
Si	579	613	−34
Si$_d$	679	702[76]	−23
Fe	746	783	−39
Cu	782	806	−34
Pt	**900**	**932**	**−32**

The results for O$_d$ and Si$_d$ are taken from the LEIS energy calculator[76], provided by the Institute of Applied Physics, and refers to the maximum possible energy with double collision.

When looking at the LEIS spectrum above it is conspicuous that the mid-range signals (between kinetic energies of $\approx$ 400-850 eV) seem to emerge from a rather high background which could be assigned to all sorts of multiple scattering (expected due to the different orientations of crystallographic domains, present on the surface of polycrystalline metal foils). Therefore, the sensitivity of the LEIS measurement in this region is reduced and significant peak shifts, shown in Table 4-4, were observed. The latter can also be the result of inelastic scattering phenomena. Especially the assignment of the Si_d-signal is ambiguous, as the single collision peak is of very weak intensity. Simply put, multiple scattering is favoured if the target's surface shows a certain degree of roughness which may be an explanation for this observation. An alternative explanation of signals in the range of Si_d would be double scattering that comprises consecutive single scattering at an O-atom and an atom of the heavy main component (here: Pt), located next to each other. Since it is not possible to provide a conclusive answer, the indication "Si_d" is kept, but pointing out that it is an assumption. Hypothetically speaking, if this signal was found on a (clean) Pt single crystal, which only shows one crystallographic orientation on the surface, identification is feasible by recording a series of LEIS spectra at different incident angles. If a variation of peak intensity occurs then this would be evidence for a feature that is caused by geometric aspects.

However, it is remarkable that a high purity Pt foil exhibits species like Si, Fe and Cu, located at its surface. Table 3-1 enlists common bulk impurities (at ppm level) of the Pt foil and therein all three species appear. Also the XPS survey spectrum, displayed in Figure 4-30, clearly demonstrates that, besides Pt, there indeed are traces of said impurities (peak identification was based on the NIST XPS database[77]).
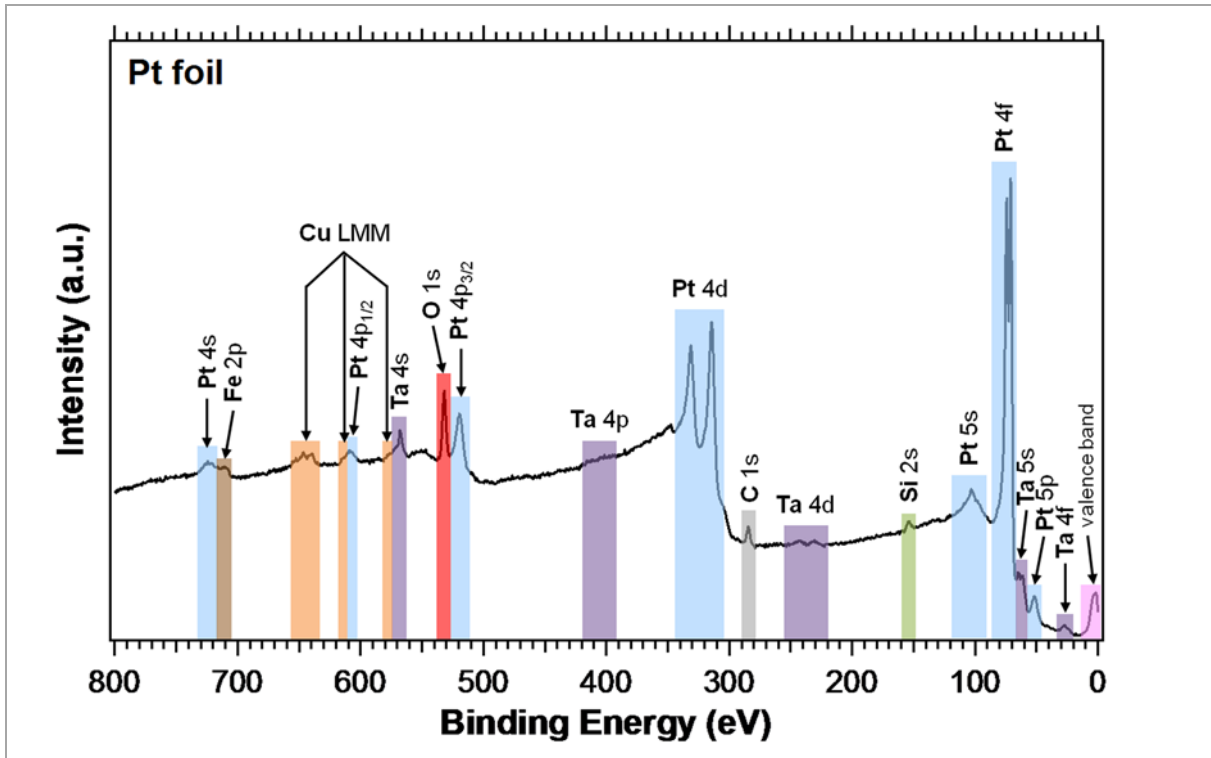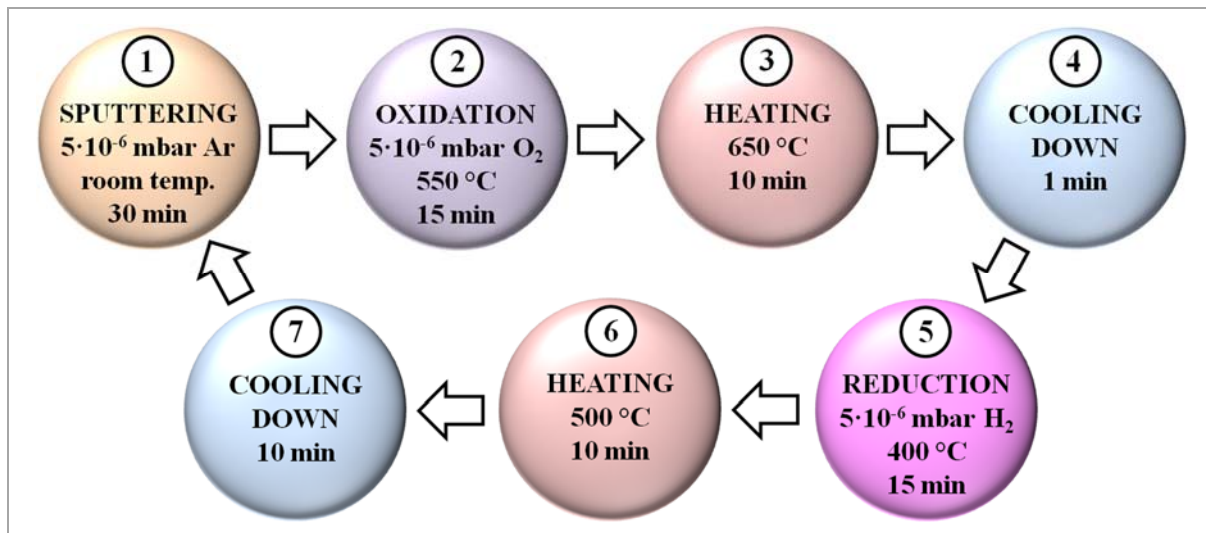
Figure 4-30: XPS survey spectrum: polycrystalline Pt foil after cleaning

If they had been on the surface before the pre-treatment, they would have been sputtered away. So it is obvious that the reason why they are still present after the performed cleaning procedure is segregation upon heating, i.e. during annealing. This phenomenon is well documented in literature[78,79] and LEIS is among the most suited methods for its investigation[10,20], as long as the segregating species' atomic masses differ sufficiently from those of main components (here: Pt). Polycrystals consist of many single crystals, separated by grain boundaries which are preferred transport channels for solutes.[80,81] These species are displayed due to the top-layer sensitivity of LEIS.

4.2. Reference material: polycrystalline Zr foil

As opposed to the polycrystalline Pt foil, the Zr foil was much more difficult to clean. The pre-treatment cycle, presented in Figure 4-31 below, was repeated multiple times.

Figure 4-31: Pre-treatment cycle of the polycrystalline Zr foil

After every two pre-treatment cycles, an XPS survey scan was taken, with main attention being paid to the signal intensities of O 1s and C 1s. The reason for this is already implied by the amount of impurities, shown in Table 3-1, which surpass those found in Pt by at least a factor 10^2 for the most species. Zr features a strong chemical affinity, in decreasing order, for O, N, S and C.[82] Again, when arriving at steps 3 and 6, the previously established oxidic or reductive atmospheres were removed and the sample was heated for the purpose of desorption. Extended sputtering did not reduce the concentration of O and C. Thus, it is assumed that these impurities were continuously segregating to the surface during heating (especially at the end, step 7). At some point, further cleaning did not affect the appearance of XPS spectra and therefore the LEIS survey scan, shown in Figure 4-32, was acquired.
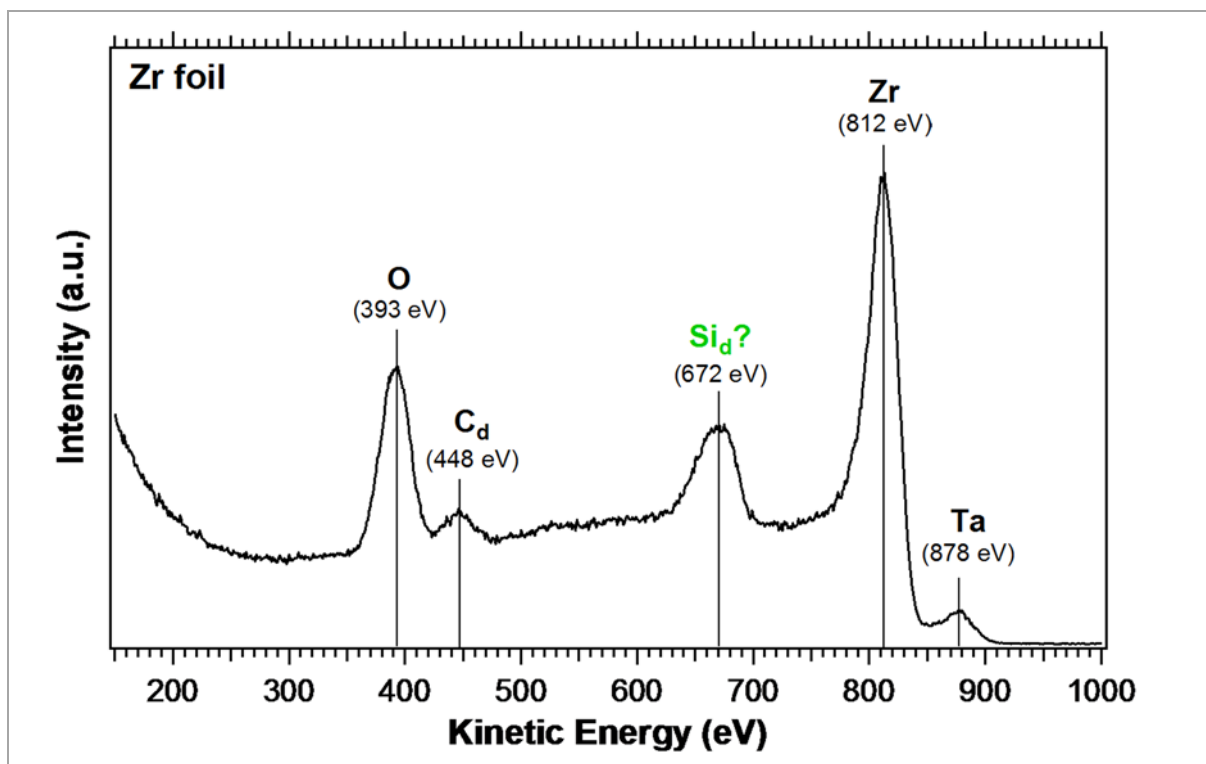
**Figure 4-32:** LEIS survey spectrum: polycrystalline Zr foil after cleaning

Analogous to the discussion of the Pt foil, Table 4-5 compares the signals of the LEIS spectrum above to calculations, based on elastic scattering.

Table 4-5: Summary of signals, found in the LEIS spectrum of the Zr foil; measured and calculated values are opposed

| Detected species	Measured kinetic energy E_1	Calculated reference kinetic energy E_{ref} (eV)	Shift of kinetic energy ($\Delta E_1 = E_1 - E_{ref}$, eV)
O	393	417	−24
C_d	448	429[76]	+19
Si_d?	672	702[76]	−30
Zr	**812**	**861**	**−49**
Ta	878	927	−49

Here, the assignment of the peak at 672 eV to Si_d makes even less sense than before because Si is not among the list of bulk impurities, given by the manufacturer, in Table 4-5. Still it cannot be ruled out since these specifications derive from random purity examinations due to significant costs of eligible analysis methods. However, if the double scattering model, proposed in the previous chapter 4.1, applies, when He$^+$ scatters on neighbouring O- and Zr-atoms, then a kinetic energy of roughly 676 eV would be measured for an elastic single collision

with O at $\theta_1 = 71°$, followed by another single collision with Zr at $\theta_2 = 64°$ ($\theta_1 + \theta_2 = 135°$). An explanation for obtained Ta-peaks in LEIS could be that spot-welded Ta-clips stick out in contrast to the reference foils which affects the trajectories of scattered He$^+$-ions (this is negligible for XPS; schematic drawing see Figure 4-33).
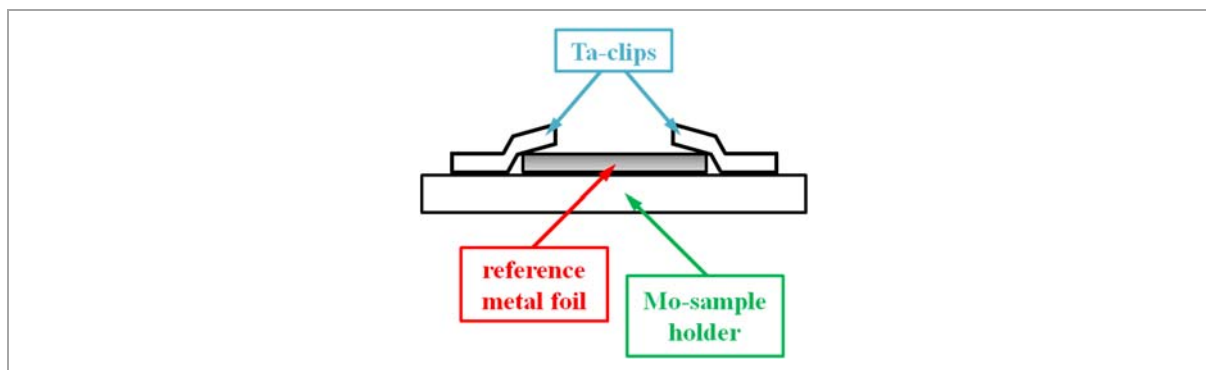
Figure 4-33: Sketch of the sample holder for reference foils including spot-welded Ta-clips (side view)

It has to be assumed that, accidentally, the iris slit was not sufficiently closed during XPS experiments, to exclude the Ta signal, which is reflected by the spectrum, displayed in Figure 4-34.
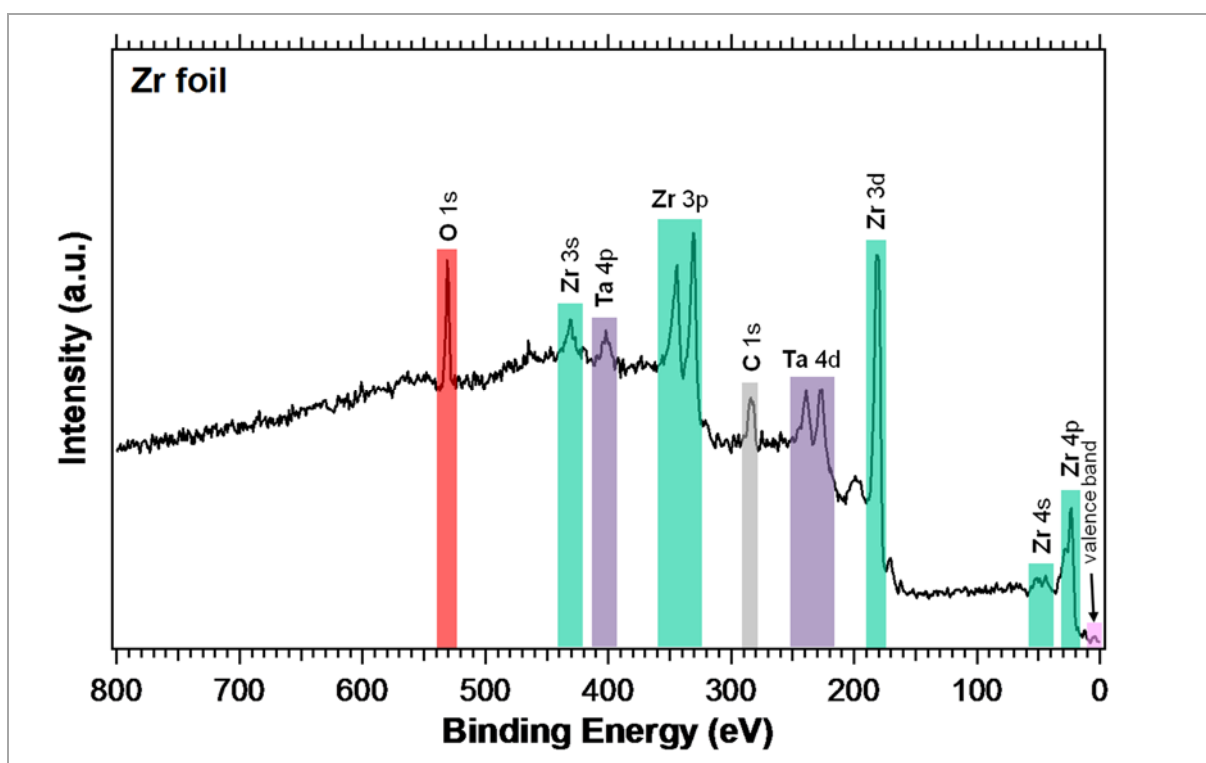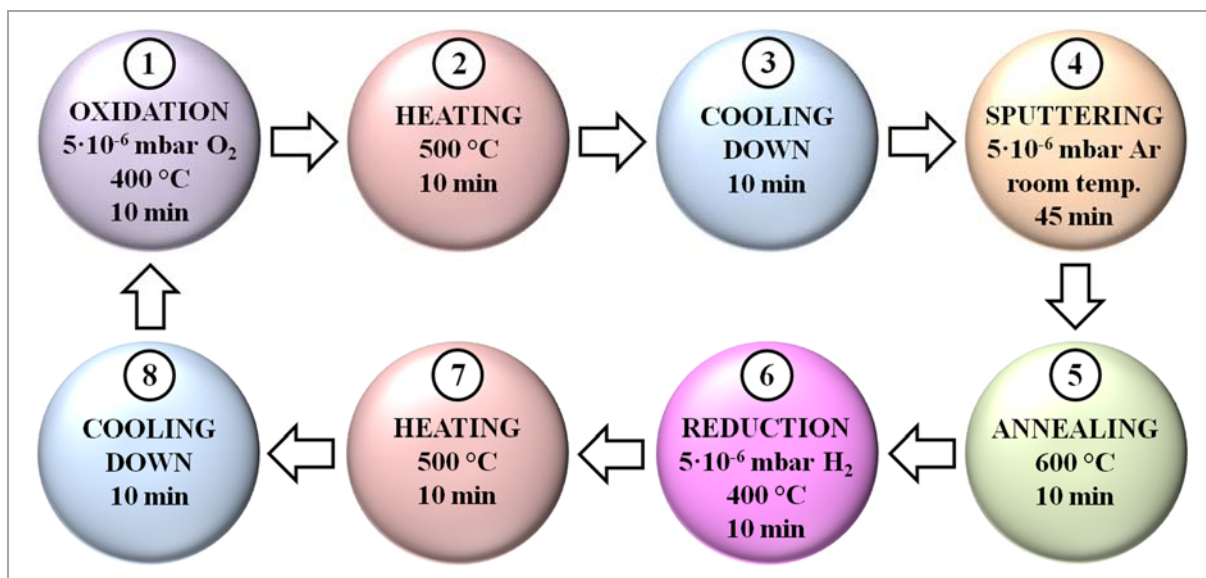

Figure 4-34: XPS survey spectrum: polycrystalline Zr foil after cleaning

Despite the great cleaning effort, there was still a large amount of O according to XPS results.

4.3. Reference material: polycrystalline Ni foil

The pre-treatment cycle, illustrated in Figure 4-35, is in fact very similar to the one conducted with the Au/Cu-target, with the exception of a prolonged sputtering time (step 4) and higher annealing temperature (step 5).

Figure 4-35: Pre-treatment cycle of the polycrystalline Ni foil

For steps 2 and 7 see chapters 4.1 and 4.2. After performing two cycles, an XPS survey spectrum was taken which indicated a clean foil. Therefore, the LEIS spectrum, shown in Figure 4-36, was recorded after a third cycle. As expected, there are hardly any significant contributions other than that of the main component, Ni. Since the cleaning efforts put into the Ni and Pt foils are comparable, it was surprising though that the nobler Pt exhibited more surface impurities than Ni. On the other hand, segregation of solutes to the surface may also play a key role here.
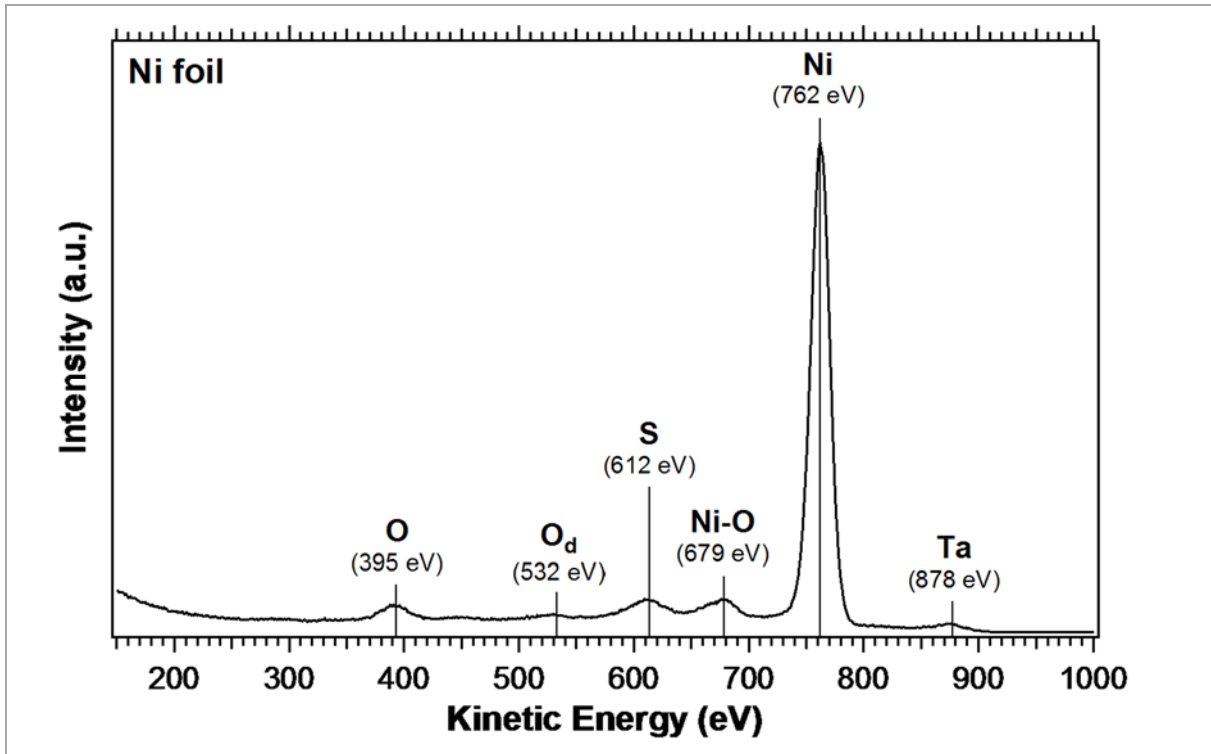
Figure 4-36: LEIS survey spectrum: polycrystalline Ni foil after cleaning

As previously, the results of the upper LEIS spectrum are compared to calculations in Table 4-6.

Table 4-6: Summary of signals, found in the LEIS spectrum of the Ni foil;

measured and calculated values are opposed

Detected species	Measured kinetic energy E_1	Calculated reference kinetic energy E_{ref} (eV)	Shift of kinetic energy ($\Delta E_1 = E_1 - E_{ref}$, eV)
O	395	417	−22
O$_d$	532	534[76]	−2
S	612	652	−40
Ni-O	679	678	—
Ni	**762**	**792**	**−30**
Ta	878	927	−49

Ni is very well featured in the upper LEIS spectrum, whereas there are only small contributions from other species. The Ni-O double scattering signal approximately fits if He$^+$-ions scatter on Ni at $\theta_1 = 69°$ and O at $\theta_2 = 66°$ subsequently, which yields a kinetic energy of ≈ 678 eV. Here, the Ta- and S-peaks could be the result of segregation to the surface.

The XPS survey spectrum, depicted in Figure 4-37, confirms that there are hardly any other species present than Ni. The intensities of O, Ta and S are very weak.
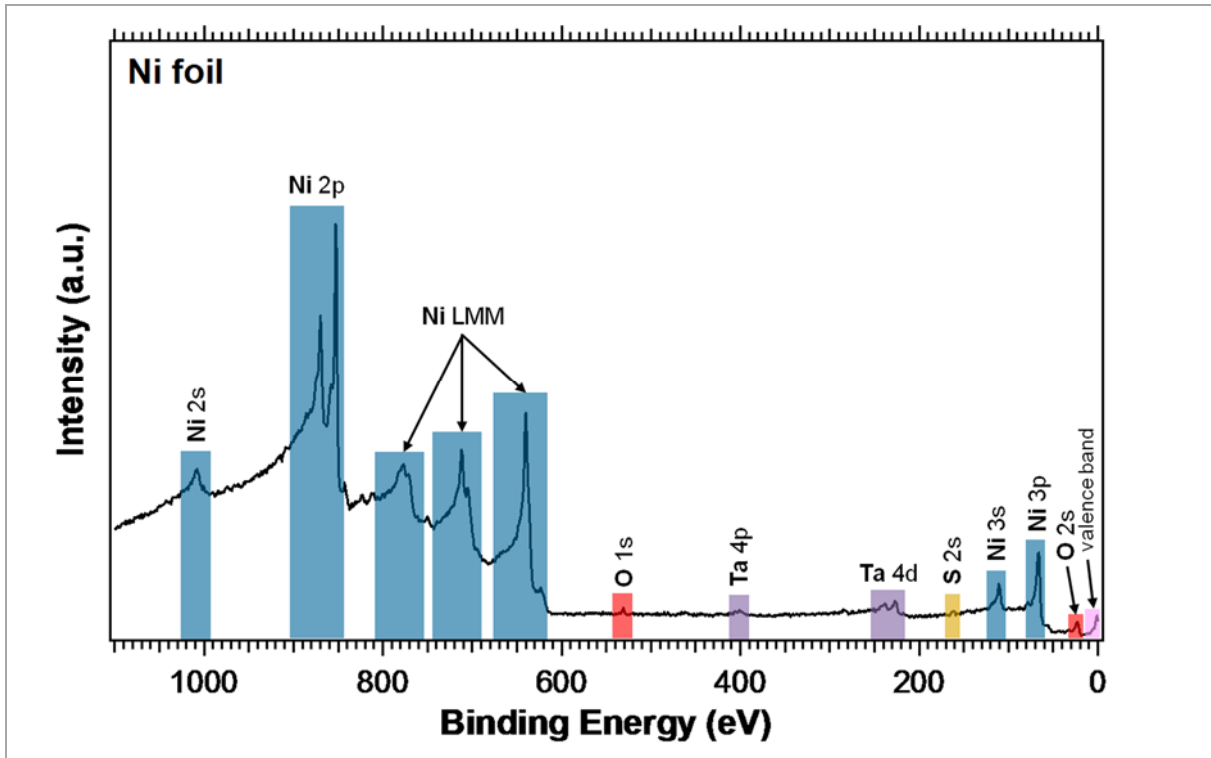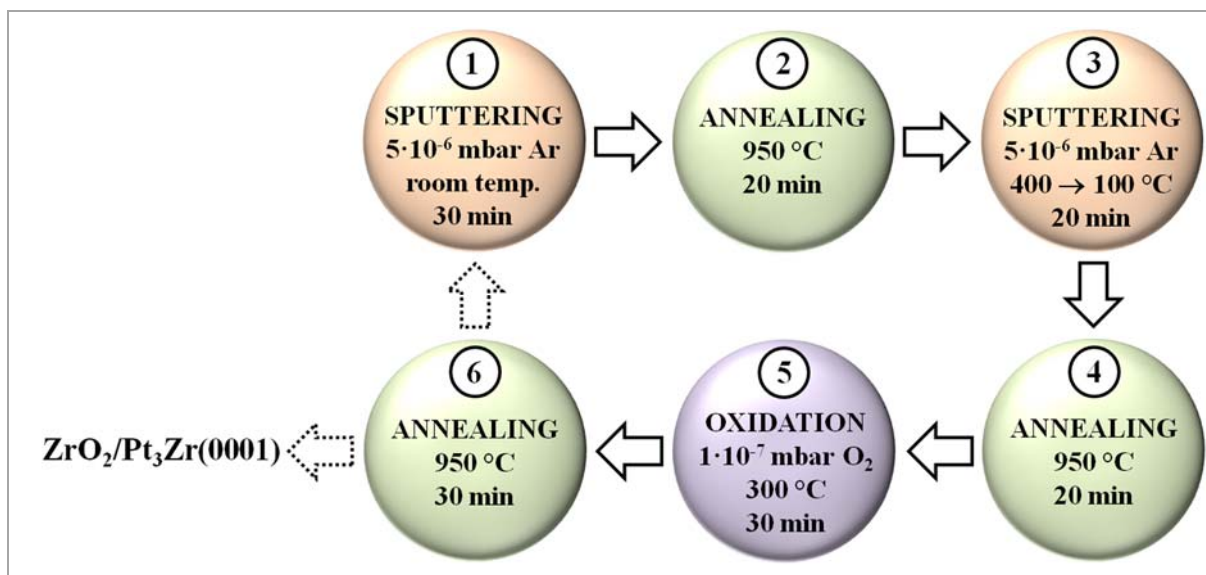

Figure 4-37: XPS survey spectrum: polycrystalline Ni foil after cleaning

4.4. Sample: Pt$_3$Zr(0001)

The preparation procedure of the Pt$_3$Zr(0001) single crystal is well described in the literature[52-54] and illustrated in Figure 4-38. The only slight differences are found in the sputtering steps 1 and 3, which were carried out at the upper pressure limit of the UHV setup.

Figure 4-38: Recipe for growing an ultrathin ZrO$_2$ film on Pt$_3$Zr(0001)[52-54]

The last arrows are only dotted which means that the treatment either ended if the ultrathin ZrO$_2$ film was successfully prepared or was repeated, as this recipe is also used as cleaning procedure. Unfortunately, the ZrO$_2$ film could not be grown on the new Pt$_3$Zr(0001) crystal. In the process, it was repeatedly tried to vary the sputtering and annealing times, the annealing temperature (since the temperature measurement was not very accurate) and the O$_2$ partial pressure, but nothing was successful. It might be assumed that the applied temperatures were probably too high (in case of $\varepsilon < 0.1$) which results in decomposition of the oxide. XPS survey spectra obtained from the new crystal (see Figure 4-39) revealed a very intense C 1s peak, even after three months of constantly running cleaning/preparation cycles. In contrast, the "old" crystal[52] was free from C after a few pre-treatment cycles.
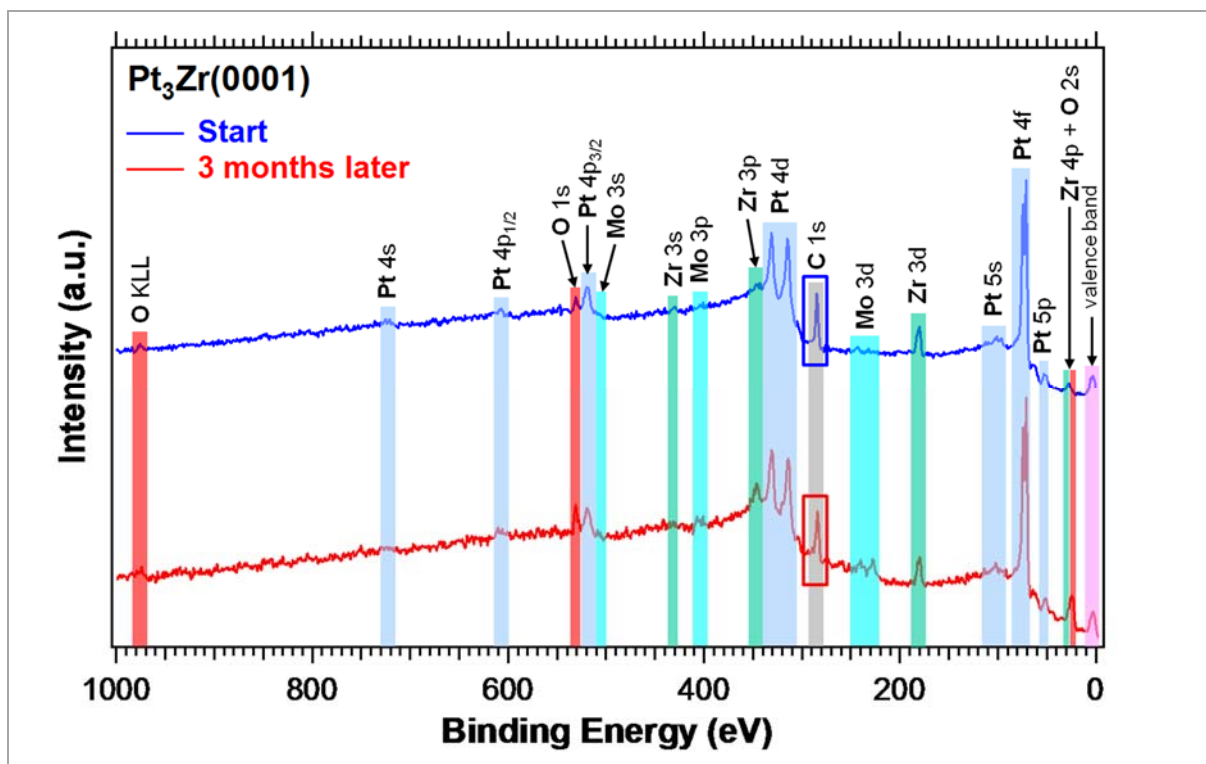
Figure 4-39: XPS survey spectra of Pt$_3$Zr(0001)

By taking into account the photoionisation cross-sections[83] of C 1s (0.014 Mbarn) and Pt 4f (0.230 Mbarn) with respect to chosen experimental parameters, the atomic ratio of Pt:C decreased from 34.2 at-% to 32.9 at-% after three months. From this it could be concluded that the amount of C even increased slightly over time. Though, the accuracy of quantification in XPS is known to be $\pm$ 10 % at best and hence it is more plausible that the conducted pre-treatments showed no cleaning effect. Nevertheless, there is about three times more C than Pt within the top $\approx$ 8 ML of the sample, which is a tremendously high amount of C. Pt and Zr could thus not be observed in most recorded LEIS spectra.

Only once, after 5 min sputtering at room temperature ($5 \cdot 10^{-6}$ mbar Ar, 2 kV), following a preparation cycle, the spectrum, displayed in Figure 4-40, was obtained.
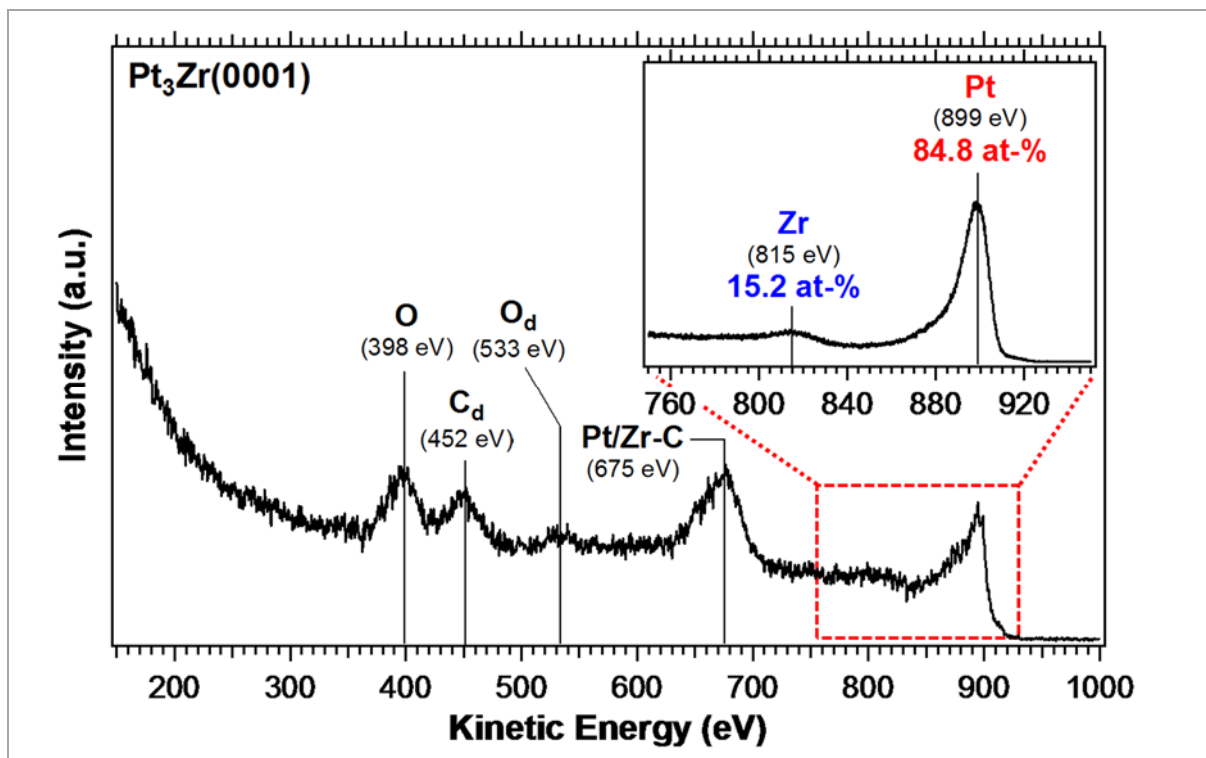
Figure 4-40: LEIS survey spectrum: $Pt_3Zr(0001)$ (inset: detailed scan of the Zr-Pt-region)

This spectrum appears rather noisy and the signal of Zr can only be guessed. Due to significant amounts of surface C it is assumed that the peak at 675 eV reflects double collisions of He^+-ions with Pt and C or Zr and C (since there is also O on the surface it could have been part of the double collision as well). The region scan (inset) was acquired immediately after the survey scan. The peak shape of Pt indicates that He^+-ions suffered from significant inelastic energy loss when colliding with Pt. The atomic ratios, given in Figure 4-40 (Pt/Zr ≈ 5:1), were calculated with respect to the Pt and Zr reference foils, neglecting existing surface impurities. Needless to say, these ratios are only very rough estimates. If the intensity of Pt is compared to that of Pt of the reference foil (Figure 4-29), then only 14.5 at-% instead of expected 75 at-% are observed. An analogous calculation for Zr yields 1.78 at % instead of 25 at-%. It is thus clear why it was not possible to grow a ZrO_2 thin film.

The peaks observed in the upper LEIS spectrum are compared to calculations in Table 4-7.

Table 4-7: Summary of signals, found in the LEIS spectrum of Pt₃Zr(0001); measured and calculated values are opposed

Detected species	Measured kinetic energy E_1	Calculated reference kinetic energy E_{ref} (eV)	Shift of kinetic energy ($\Delta E_1 = E_1 - E_{ref}$, eV)
O	398	417	−19
O$_d$	533	534[76]	−1
C$_d$	452	429[76]	+23
Pt-C	675	678*	—
Zr-C	675	676†	—
Zr	**815**	**861**	**−46**
Pt	**899**	**932**	**−33**

* for $\theta_1(Zr) = 77°$ and $\theta_2(C) = 58°$; † for $\theta_1(Pt) = 73°$ and $\theta_1(C) = 62°$

The kinetic energies are in good agreement with those of reference foils (presented in Table 4-4 and Table 4-5).

AR-XPS not only provides a validation of the LEIS data, acquired from the new Pt₃Zr(0001) crystal, but it is also possible to compare the effect of i) sputtering at room temperature (here: 15 min, 5·10⁻⁶ mbar Ar, 2 kV) and ii) three consecutive pre-treatment cycles (sputtering by employing the same parameters as in i), followed by annealing for 20 min at 900 °C, under UHV). In addition, depth profile analysis based on spectra recorded at different take-off angles, may visualise concentration gradients. Therefore, the exit angle of photoelectrons, detected by the ESA, was varied by azimuthal rotation of the sample between $\vartheta = 0°$ (which corresponds to photoelectrons that move along the surface normal to the ESA; largest information depth) and 40° (here: lowest information depth) in direction of the X-ray gun. In each case, the angle was changed in steps of 10°. As the first spectra of Pt 4f and Zr 3d were recorded it became apparent that angles higher than 40° were not meaningful since the detection limit of Zr was already reached at this point. In order to supplement the results of Pt and Zr, the C 1s region was also examined. Depth profiles are plotted and compared, regarding both mentioned sample treatments, in Figure 4-41, Figure 4-42 and Figure 4-43.
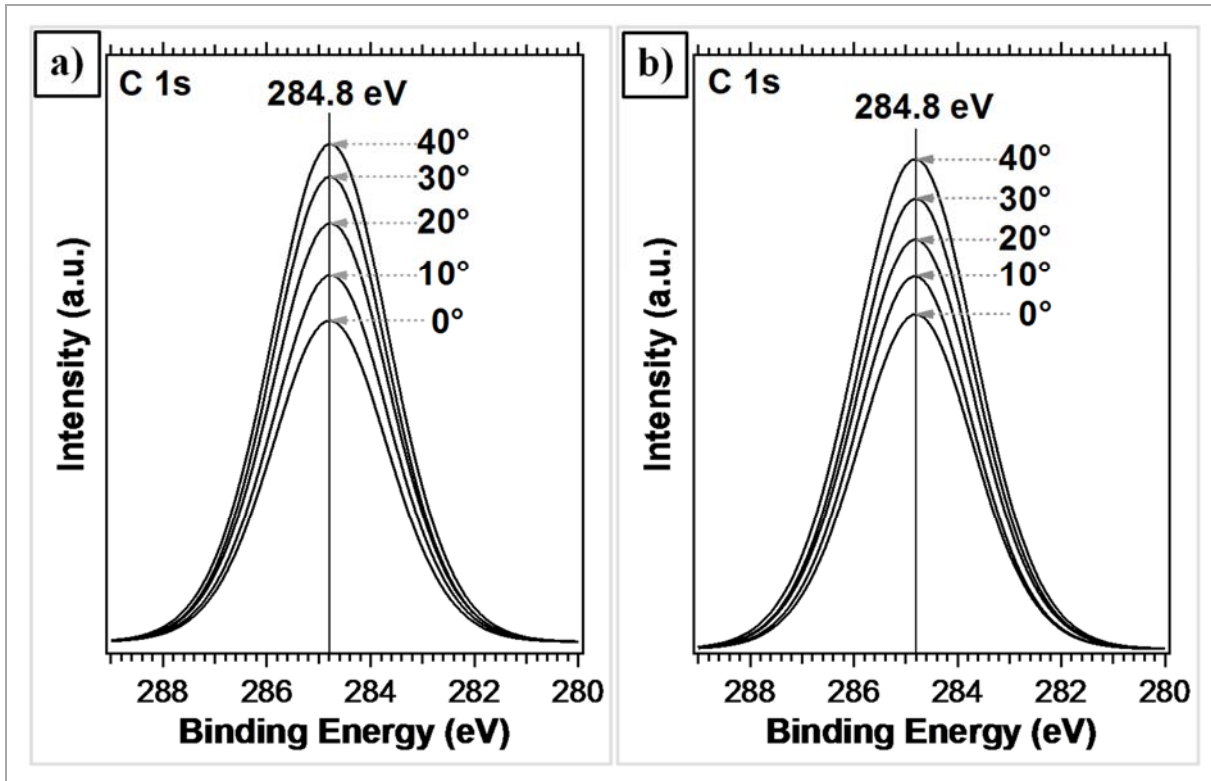
Figure 4-41: AR-XPS of Pt$_3$Zr(0001), C 1s region: a) after three pre-treatment cycles, b) after sputtering
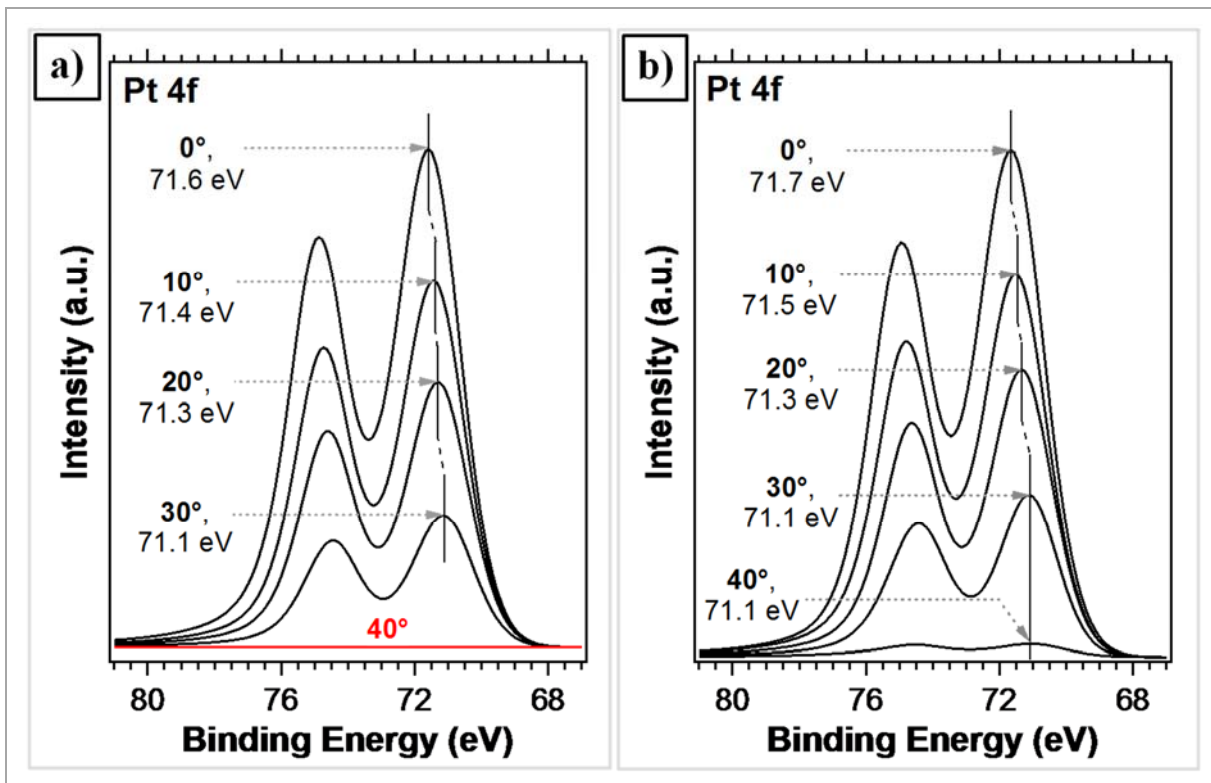

Figure 4-42: AR-XPS of Pt$_3$Zr(0001), Pt 4f region: a) after three pre-treatment cycles, b) after sputtering
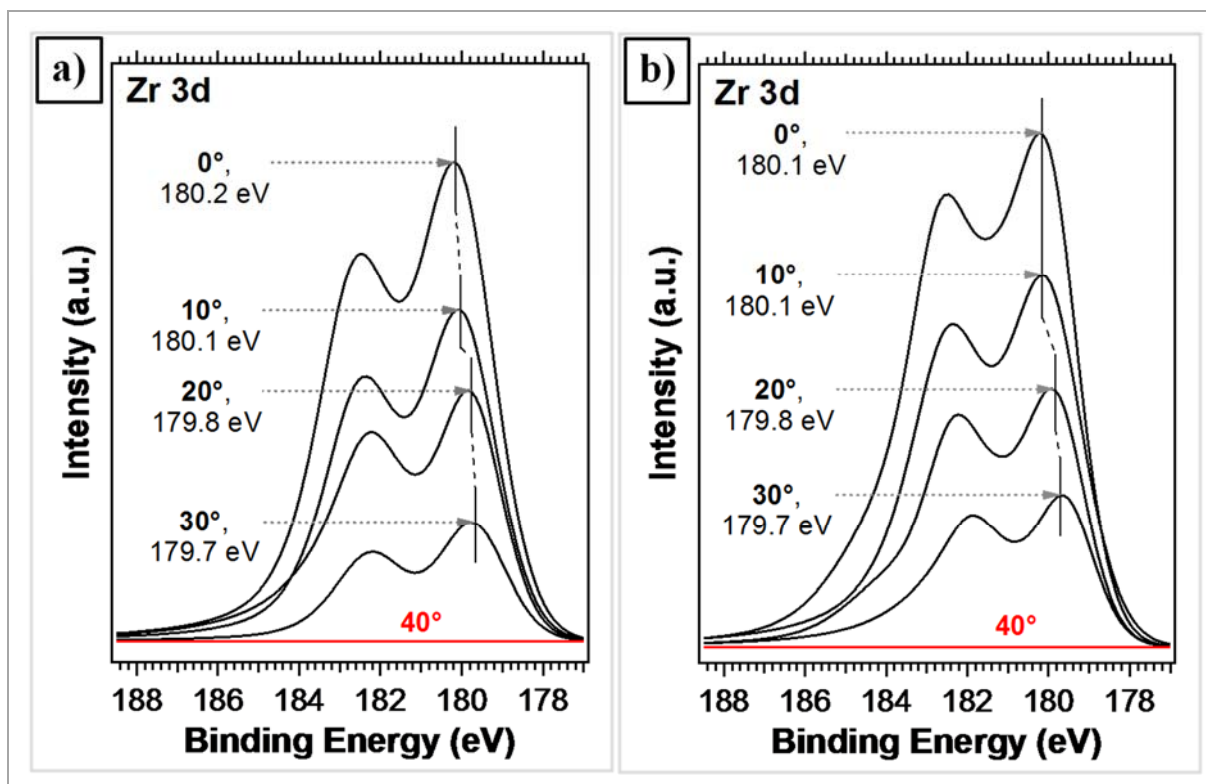
Figure 4-43: AR-XPS of Pt₃Zr(0001), Zr 3d region: a) after three pre-treatment cycles, b) after sputtering

The doublets of Pt and Zr are due to spin orbit splitting. The peak positions (binding energies) agree well with those of metallic Pt (71.4 eV) and Zr (179.6 eV), reported in the literature.[53] Marginal shifts to lower binding energies with decreasing information depth suggest an increase of electron density towards the surface. In this direction, the intensity of C is continuously increased whereas signals of Zr and Pt fade away. At an angle of 40° only a weak signal of Pt is detected if the sample was just sputtered. It can be concluded that the surface is passivated by graphitic C to a great extent. The fact that C is even found to a significant degree within deeper atomic layers of the sample, is an indication of C segregation from the bulk to the surface. Since the formation of ZrC can be excluded due to a missing shoulder at ≈ 282.2 eV[84] in the C 1s region, it is assumed that C is located at interstitials. Otherwise, the stoichiometry of the single crystal would be compromised. The concentration profiles, shown in Figure 4-44 and Figure 4-45, should provide clarification. Underlying calculations again involved the above mentioned photoionisation cross-sections as well as the one of Zr 3d, which is 0.097 Mbarn[83].
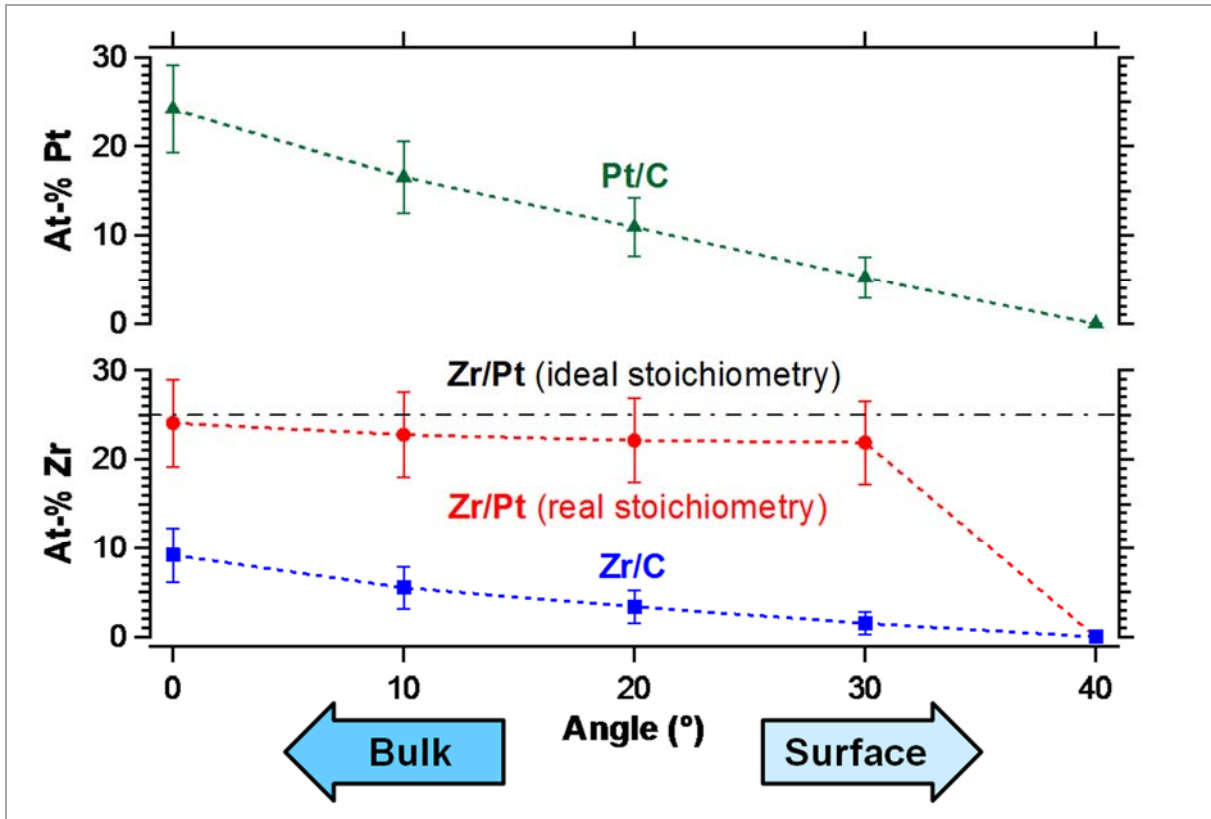
Figure 4-44: Depth profile results from AR-XPS of Pt$_3$Zr(0001) after three pre-treatment cycles
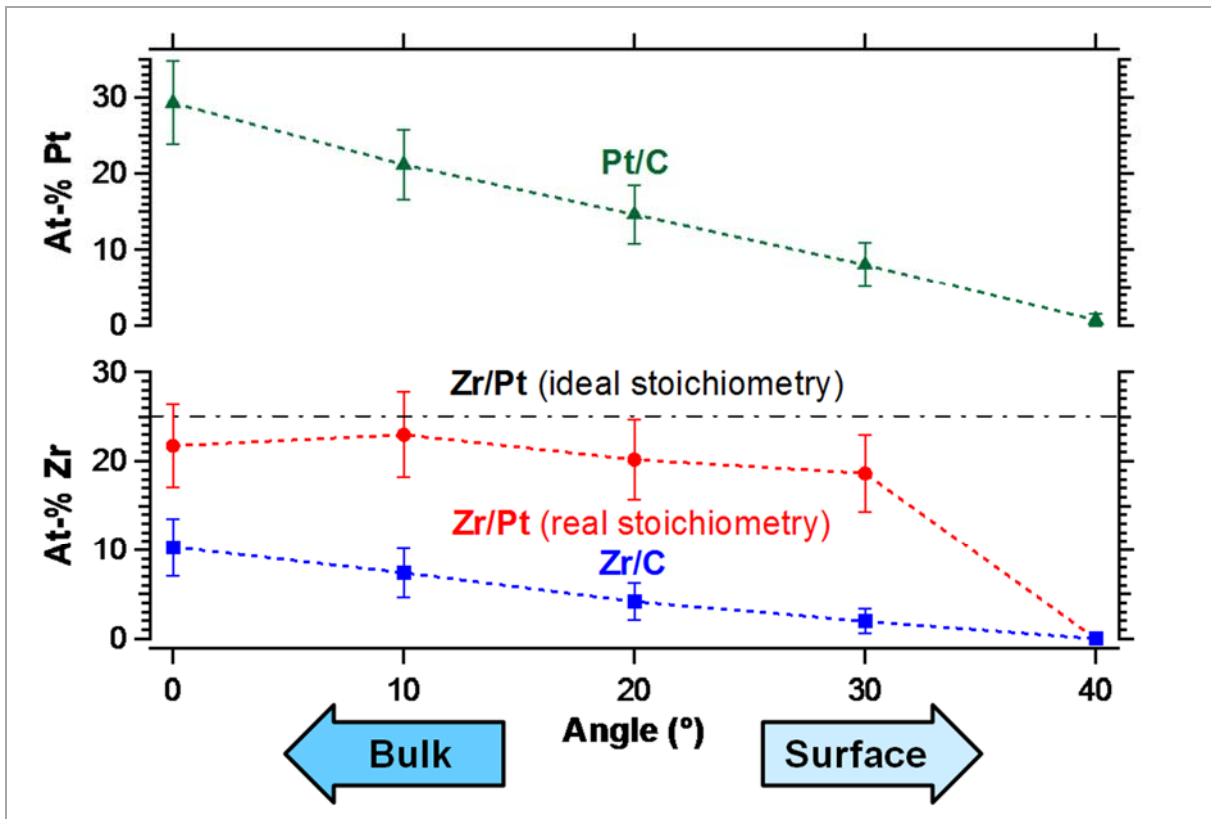

Figure 4-45: Depth profile results from AR-XPS of Pt$_3$Zr(0001) after sputtering

The trends of the ratios of Pt/C and Zr/C are similar after both treatments, especially as far as the latter is concerned. Upon annealing the distribution of C seems more regular across the examined depth range which causes a smaller slope of the Pt/C ratio. The Zr/Pt ratio decreases steadily towards the surface and changes abruptly between angles of 30° and 40°. Its trend is rather erratic if the sample was just sputtered. Hence, it is implied that Zr is preferentially sputtered away which makes sense due to its much lower atomic mass in comparison to that of Pt. This has a significant influence on the stoichiometry up to a certain depth, which depends on the kinetic energy of impinging Ar^+-ions and the sputter time. In general, the stoichiometry of $Pt_3Zr(0001)$ seems to be intact within subjacent atomic layers and is only altered close to the surface. This substantiates the assumption that the major part of the surface is passivated/poisoned by C and that C is segregating to the surface from bulk interstitials. Apart from that, the results of AR-XPS experiments clearly demonstrate the superior surface sensitivity of LEIS, which still allows the detection of Pt and Zr in the topmost atomic layer of the sample surface.

It can be excluded that the C-impurity originated from the UHV setup because C was not observed after pre-treating the Ni foil. Therefore, it is evident that the mentioned impurity originates from the synthesis of the single crystal. MaTecK is using Pt and Zr metal powders of technical purity for growing $Pt_3Zr(0001)$ in a mirror furnace under inert gas (Ar). The purity of these powders is examined qualitatively *via* X-ray fluorescence analysis (XRF) on a random basis and rarely (due to considerable costs) by inductively coupled plasma mass spectrometry (ICP-MS).[85] It is most likely that the Zr powder had been contaminated by significant amounts of C which could not be removed during the zone melting.

5. Summary

The objective of the present thesis was to describe the theoretical background of LEIS to the experimentalist and to demonstrate a seemingly simple application, i.e. the determination of the chemical composition of a single crystal alloy surface – namely that of $Pt_3Zr(0001)$.

In the course of this endeavour, physical principles that are important for the understanding of spectral results of LEIS measurements were presented stepwise, using the analogy with a billiard ball game. Special attention was paid to aspects which are responsible for the ultimate surface sensitivity of LEIS, particularly prevalent for He^+-projectile ions at a low kinetic energy of 1 keV.

A detailed description of the UHV setup involved a critical analysis of instrumental parameters, which contribute to the quality of the acquired LEIS spectra. This was followed by the implementation of a suitable scattering geometry with respect to the position and dimension of the sample single crystal, mounted on a transferrable sample holder. The difficulty at hand – the invisibility of the He^+-ion beam – was mastered by designing a scattering target that mimics the shape of a single crystal mounted to the sample holder. The final design consisted of two high purity polycrystalline foils of Au and Cu, with a hole cut into the Cu foil and put on top of the Au foil, forming a golden "bulls eye" in the centre. Since the kinetic energy of backscattered He^+-ions mainly depends on the mass of a target atom for a given experimental geometry, the strongest possible Au-response was aimed for. Optimum parameters yielded a value of approximately 83.3 at-% Au. Possibly, the rather large distance between the ion source and the sample diminished the accuracy of the ion beam. Nevertheless, these parameters were kept for the following experimental measurements of this work.

In order to allow quantitative analysis of a LEIS spectrum it is a well-established approach to use high purity polycrystalline metal foils as reference materials. Therefore, LEIS and XPS survey scans of a Pt and Zr foil were obtained. Also a Ni foil was measured as an additional standard. In case of a successful preparation of an ultrathin ZrO_2 film, grown on $Pt_3Zr(0001)$, quantification of subsequently deposited Ni-nanoparticles should have been possible with this work. All foils were pre-treated extensively for cleaning, necessary due to the high surface sensitivity of LEIS. Reference data was acquired to a satisfying degree with both analytic methods. On the Pt foil also bulk impurities (being in the ppm-range according to vendors) Si, Fe and Cu were observed clearly *via* LEIS, which could only be guessed within the XPS scan. Their presence after pre-treatments hints to segregation upon annealing after oxidation and

reduction at elevated temperatures. This is a well-known phenomenon, encountered even on high purity noble metal foils.

Cleaning of $Pt_3Zr(0001)$ and preparation of an ultrathin ZrO_2 film are more or less similar procedures. It is reported that H_2 embrittles the Pt_3Zr crystal. Hence, reduction was not applied. Despite oxidative treatments, a ZrO_2 thin film could not be grown, despite many efforts varying the preparation procedure, only interrupted by XPS measurements. XPS revealed a significant amount of graphitic C within the top atomic layers of the sample. Interestingly, the quantity of C remained the same, even after months of cleaning procedures. Upon short Ar-sputtering, a LEIS survey and region spectrum was recorded that showed only 14.5 at-% Pt and 1.78 at-% Zr in comparison to surface concentrations found for the reference foils (in contrast to the ideal values of 75 at-% Pt and 25 at-% Zr for Pt_3Zr). The stoichiometry of these leftover "main" components was approximately $Pt/Zr \approx 5:1$, explaining why the preparation of the ZrO_2 thin film had failed.

To discuss the origin of the C impurity further, depth profile analysis by AR-XPS was carried out. The results obtained indicated that the stoichiometry of $Pt_3Zr(0001)$ was intact within the bulk but drastically changed close to the surface where the main components were (almost) replaced by C. The absence of ZrC leads to the conclusion that C is located at interstitials and repeatedly segregates from a bulk reservoir to the surface after treatments at elevated temperatures.

The origin of the C impurity within the single crystal is likely related to the synthesis. The manufacturer, MaTecK, used Pt and Zr metal powders as materials for zone melting without checking their purity beforehand. It must be assumed that the Zr powder was contaminated with C, maybe due to the affinity of Zr to C. As a result the Pt_3Zr single crystal exhibited a significant bulk reservoir of C that could not be removed.

References

[1]   Sachtler, W. M. H., and Van Santen, R. A. "Surface composition and selectivity of alloy catalysts." *Advances in catalysis* 26 (1977): 69-119.

[2]   Chorkendorff, I., and Niemantsverdriet, J.W. *Concepts of modern catalysis and kinetics*. John Wiley & Sons, 2017.

[3]   Wang, J., Fan, C. J., Sun, Q., Reuter, K., Jacobi, K., Scheffler, M., and Ertl, G. "Surface coordination chemistry: Dihydrogen versus hydride complexes on RuO2 (110)." *Angewandte Chemie International Edition* 42.19 (2003): 2151-2154.

[4]   Nørskov, J. K., Bligaard, T., Hvolbæk, B., Abild-Pedersen, F., Chorkendorff, I., and Christensen, C. H. "The nature of the active site in heterogeneous metal catalysis." *Chemical Society Reviews* 37.10 (2008): 2163-2171.

[5]   Somorjai, G. A., and Li, Y. *Introduction to surface chemistry and catalysis*. John Wiley & Sons, 2010.

[6]   Stamenkovic, V., Mun, B. S., Mayrhofer, K. J. J., Ross, P. N., Markovic, N. M., Rossmeisl, J., Greeley, J., and Nørskov, J. K. "Changing the activity of electrocatalysts for oxygen reduction by tuning the surface electronic structure." *Angewandte Chemie* 118.18 (2006): 2963-2967.

[7]   Rabalais, J. W. *Principles and applications of ion scattering spectrometry: surface chemical and structural analysis*. New York: Wiley, 2003.

[8]   Vickerman, J. C., and Gilmore, I. *Surface analysis: the principal techniques*. John Wiley & Sons, 2011.

[9]   Ertl, G., Knözinger, H., and Weitkamp, J. "Handbook of heterogeneous catalysis." (1997): 1831.

[10]   Niehus, H., Heiland, W., and Taglauer, E. "Low-energy ion scattering at surfaces." *Surface Science Reports* 17.4-5 (1993): 213-303.

[11]   Hwang, C. S., and Yoo, C. J. *Atomic layer deposition for semiconductors*. Springer Science & Business Media, 2013.

[12]   Henning, B., Rivière, J. C., Arlinghaus, H. F., Hutter, H., Jenett, H., Bauer, P., Palmetshofer, L., Fabry, L., Pahlke, S., Quentmeier, A., Hinrichs, K., Hill, W., Gruska, B., Röseler, A., and Friedbacher, G. *Surface and Thin-Film Analysis*. Wiley-VCH Verlag GmbH & Co. KGaA, 2002.

[13]   Jacobs, K. *Schematic drawing of a typical photoelectron spectrometer.* Universität Saarland (retrieved: October 9th, 2017):
       http://jacobs.physik.uni-saarland.de/images/Photomemission%20Setup.jpg

[14]   Carlson, T. A., and Krause, M. O. "Experimental evidence for double electron emission in an Auger process." *Physical Review Letters* 14.11 (1965): 390.

[15]   Benninghoven, A. "Surface investigation of solids by the statical method of secondary ion mass spectroscopy (SIMS)." *Surface Science* 35 (1973): 427-457.

[16]   Secondary ion mass spectrometry. Encyclopædia Britannica, Inc.
       (retrieved: October 9th, 2017):
       https://media1.britannica.com/eb-media/43/123343-004-6A7E5D80.jpg

[17]   Suchorski, Y. "Probing adsorption on a nanoscale: field desorption microspectroscopy." *Adsorption* 23.2-3 (2017): 217-224.

[18]   Raabe, D., Metallurgical Materials Science, Grain boundary segregation energineering (retrieved: October 9th, 2017):
       http://www.dierk-raabe.com/grain-boundary-segregation-engineering/

[19]   Czanderna, A. W., and Hercules, D. M. *Ion spectroscopies for surface analysis.* Vol. 2. Springer Science & Business Media, 2012.

[20]   Brongersma, H. H., Draxler, M., de Ridder, M., and Bauer, P. "Surface composition analysis by low-energy ion scattering." *Surface Science Reports* 62.3 (2007): 63-109.

[21]   Rameshan, C., Weilach, C., Stadlmayr, W., Penner, S., Lorenz, H., Hävecker, M., Blume, R., Rocha, T., Teschner, D., Knop-Gericke, A., Schlögl, R., Zemlyanov, D., Memmel, N., Rupprechter, G., and Klötzer, B. "Steam reforming of methanol on PdZn near-surface alloys on Pd(111) and Pd foil studied by in-situ XPS, LEIS and PM-IRAS." *Journal of Catalysis* 276.1 (2010): 101-113.

[22]   Dulub, O., Hebenstreit, W., and Diebold, U. "Imaging cluster surfaces with atomic resolution: the strong metal-support interaction state of Pt supported on $TiO_2(110)$." *Physical Review Letters* 84.16 (2000): 3646.

[23]   Rutherford, E. "LXXIX. The scattering of α and β particles by matter and the structure of the atom." *The London, Edinburgh, and Dublin Philosophical Magazine and Journal of Science* 21.125 (1911): 669-688.

[24]   Chu, W.-K., Mayer, J. W., and Nicolet, M.-A. *Backscattering spectrometry.* Elsevier, 2012.

[25]   Smith, D. P. "Scattering of Low-Energy Noble Gas Ions from Metal Surfaces." *Journal of Applied Physics* 38.1 (1967): 340-347.

[26]   SPECS ion source IQE 12/38 product brochure (retrieved: September 12th, 2017): http://www.specs.de/cms/front_content.php?idcat=103

[27]   SPECS hemispherical analyser with wide-angle lens PHOIBOS 150 WAL product brochure (retrieved: September 12th, 2017): http://www.specs.de/cms/front_content.php?idcat=266

[28]   Logan, R. M., Keck, J. C., and Stickney, R. E. "Simple classical model for the scattering of gas atoms from a solid surface." *The Journal of Chemical Physics* 44.1 (1966): 195-201.

[29]   Igel, T. *Untersuchung der strukturellen und magnetischen Eigenschaften ultradünner 3d-Metall-Filme auf Fe(100) mit Ionenstrahlen*. Diss. Humboldt-Universität zu Berlin, Mathematisch-Naturwissenschaftliche Fakultät I, 2001.

[30]   Liegl, A. "Untersuchungen zum Rauhigkeitsübergang an der Cu(115)-Oberfläche mittels Ionenstreuung." (1992).

[31]   Hellings, G. J. A. *Energy and Angle Resolved Ion Scattering Spectroscopy*. Diss. Thesis, Technical University, Eindhoven, The Netherlands, 1986.

[32]   MacDonald, R. J., O'Connor, D. J., King, B. V., Ting, L., and Li, Z. "Problems of Quantitative Surface Composition Analysis Using LEIS." *Surface Science*. Springer Berlin Heidelberg, 1996. 101-114.

[33]   Morais, J., da Rosa, E. B. O., Miotti, L., Pezzi, and Baumvol, I. J. R. "Stability of zirconium silicate films on Si under vacuum and O_2 annealing." *Applied Physics Letters* 78.17 (2001): 2446-2448.

[34]   John, R. *Solid State Physics, 1e*. McGraw-Hill Education, 2014.

[35]   Markin, S. N., Primetzhofer, D. and Bauer, P. "On the origin of the LEIS signal in TOF-and in ESA-LEIS." *Nuclear Instruments and Methods in Physics Research Section B: Beam Interactions with Materials and Atoms* 267.4 (2009): 634-637.

[36]   Primetzhofer, D., Spitz, M., Taglauer, E., and Bauer, P. "Resonant charge transfer in low-energy ion scattering: Information depth in the reionization regime." *Surface science* 605.21 (2011): 1913-1917.

[37]   Sigmund, P. "Theory of sputtering. I. Sputtering yield of amorphous and polycrystalline targets." *Physical review* 184.2 (1969): 383.

[38]   Biersack, J. P. "Computer simulations of sputtering." *Nuclear Instruments and Methods in Physics Research Section B: Beam Interactions with Materials and Atoms* 27.1 (1987): 21-36.

[39]   Bird, J. R., and Williams, J. S. *Ion beams for materials analysis.* Elsevier, 1990.

[40]   Ter Veen, H. R. J., Kim, T., Wachs, I. E., and Brongersma, H. H. "Applications of high sensitivity-low energy ion scattering (hs-leis) in heterogeneous catalysis." *Catalysis Today* 140.3 (2009): 197-201.

[41]   Jacobs, J-P., Reijne, S., Elfrink, R. J. M., Mikhailov, S. N., and Brongersma, H. H. "Quantification of the composition of alloy and oxide surfaces using low-energy ion scattering." *Journal of Vacuum Science & Technology A: Vacuum, Surfaces, and Films* 12.4 (1994): 2308-2313.

[42]   Brongersma, H. H., and van Santen, R. A. *Fundamental aspects of heterogeneous catalysis studied by particle beams.* Vol. 265. Springer Science & Business Media, 2013.

[43]   Wutz, M., Adam, H., and Walcher, W. *Handbuch Vakuumtechnik: Theorie und Praxis.* Springer-Verlag, 2013.

[44]   Fauster, Th. "Surface geometry determination by large-angle ion scattering." *Vacuum* 38.2 (1988): 129-142.

[45]   Holzapfel, H. H. *Surface science investigations of catalytic alloys on metal surfaces by XPS, PM-IRAS, TPD, LEED, and STM.* Diss. Technische Universität Wien, Fakultät für Technische Chemie, 2015.

[46]   Weilach, C. *Surface science investigations of mono-and bimetallic catalytic nanostructures by PM-IRAS and XPS spectroscopy.* Diss. Technische Universität Wien, Fakultät für Technische Chemie, 2009.

[47]   Eberhard, B. *Computer simulations for thorium doped tungsten crystals.* Diss. Universität Augsburg, Mathematisch-naturwissenschaftliche Fakultät, 2009.

[48]   Müller, E. W. "Work function of tungsten single crystal planes measured by the field emission microscope." *Journal of Applied Physics* 26.6 (1955): 732-737.

[49]   Riviere, J. C. "The Work Function of Thorium." *Proceedings of the Physical Society* 80.1 (1962): 124.

[50]   Denzler, D. N. *Zur ultraschnellen Reaktionsdynamik von Wasserstoff und Grenzflächenstruktur von Wasser auf der Ru(001)-Oberfläche.* Diss. Freie Universität Berlin, 2003.

[51] SPECS hemispherical analyser PHOIBOS 100/150 product brochure
(retrieved: October 3rd, 2017)
http://www.specs.de/cms/front_content.php?idart=122

[52] Anic, K. *Preparation and characterization of Ni/ZrO$_2$/Pd$_3$Zr as model systems for methane reforming*. Dipl.-Arb. Technische Universität Wien, Fakultät für Technische Chemie, 2013.

[53] Li, Hao, Choi, J.-I. J., Mayr-Schmölzer, W., Weilach, C., Rameshan, C., Mittendorfer, F., Redinger, J., Schmid, M., and Rupprechter, G. "Growth of an ultrathin zirconia film on Pt$_3$Zr examined by high-resolution x-ray photoelectron spectroscopy, temperature-programmed desorption, scanning tunneling microscopy, and density functional theory." *The Journal of Physical Chemistry C* 119.5 (2015): 2462-2470.

[54] Antlanger, M., Mayr-Schmölzer, W., Pavelec, J., Mittendorfer, F., Redinger, J., Varga, P., Diebold, U., and Schmid, M. "Pt$_3$Zr(0001): A substrate for growing well-ordered ultrathin zirconia films by oxidation." *Physical Review B* 86.3 (2012): 035451.

[55] Volkov, S. A. "Operando X-ray investigation of solid oxide fuel cell model electrodes." (2017).

[56] Choi, J.-I. J., Mayr-Schmölzer, W., Valenti, I., Luches, P., Mittendorfer, F., Redinger, J., Diebold, U., and Schmid, M. "Metal Adatoms and Clusters on Ultrathin Zirconia Films." *The Journal of Physical Chemistry C* 120.18 (2016): 9920-9932.

[57] Puigdollers, A. R., and Pacchioni, G. "Reducibility of ZrO$_2$/Pt$_3$Zr and ZrO$_2$/Pt 2D films compared to bulk zirconia: a DFT + U study of oxygen removal and H$_2$ adsorption." *Nanoscale* 9.20 (2017): 6866-6876.

[58] Stalick, J. K., and Waterstrat, R. M. "The zirconium–platinum phase diagram." *Journal of alloys and compounds* 430.1 (2007): 123-131.

[59] Pan, Y., Guan, W., Wen, M., Zhang, J., Wang, C., and Tan, Z. "Hydrogen embrittlement of Pt$_3$Zr compound from first-principles." *Journal of Alloys and Compounds* 585 (2014): 549-554.

[60] MaTecK GmbH, Metallische Einkristalle (retrieved: October 11th, 2017)
https://mateck.com/info/metallische-einkristalle.html

[61] MaTecK GmbH, "Re: Herstellungsprozess: Pt$_3$Zr(0001)", message to the author, August 8th, 2017

[62] Goodfellow GmbH, online catalogue, polycrystalline Pt foil (retrieved: October 12th, 2017)
http://www.goodfellow.com/catalogue/GFCat4I.php?ewd_token=kHjnuyWgNKZRqyJBhkOD
Avu8939CZl&n=rjBWqJK4QNPbhxg7UaCbrbOnWN2xgl&ewd_urlNo=GFCat411&Catite=P
T000260&CatSearNum=2

[63] Goodfellow GmbH, online catalogue, polycrystalline Zr foil (retrieved: October 12th, 2017) http://www.goodfellow.com/catalogue/GFCat4I.php?ewd_token=RNMCH76L9erwNUaApRf2f hNN0WXk0c&n=AhIB9c2kYcAehAn5DLd2ICmHYHtkFn&ewd_urlNo=GFCat411&Catite=Z R000260&CatSearNum=6

[64] Alfa Aesar GmbH & Co KG, "Re: Article 12046, Nickel foil, thickness 0.1 mm, purity 99.994 %", message to the author, April 21st, 2017

[65] Zeng, H., Duan, G., Li, Y., Yang, S., Xu, X., and Cai, W. "Blue Luminescence of ZnO nanoparticles based on non-equilibrium processes: defect origins and emission controls." *Advanced Functional Materials* 20.4 (2010): 561-572.

[66] Kumar, R., Kumar, G., and Umar, A. "Pulse laser deposited nanostructured ZnO thin films: A review." *Journal of nanoscience and nanotechnology* 14.2 (2014): 1911-1930.

[67] Takai-Yamashita, C., Ishino, T., Razavi-Khosroshahi, H., and Fuji, M. "ZnO crystals supported by hollow SiO_2 nanoparticles with fluorescent property." *Journal of the Ceramic Society of Japan* 124.3 (2016): 239-241.

[68] Chaaya, A. A., Viter, R., Baleviciute, I., Bechelany, M., Ramanavicius, A., Gertnere, Z., Erts, D., Smynthyna, V., and Miele, P. "Tuning optical properties of Al_2O_3/ZnO nanolaminates synthesized by atomic layer deposition." *The Journal of Physical Chemistry C* 118.7 (2014): 3811-3819.

[69] Roszell, J. P. T. *The Effect of Ion Energy and Substrate Temperature on Deuterium Trapping in Tungsten*. Diss. University of Toronto (Canada), 2012.

[70] SPECS ion source IQE 12/38 user manual v2.2, December 16th, 2013

[71] SPECS ion source IQE 12/38 website (retrieved: October 14th, 2017): http://www.specs.de/cms/front_content.php?idcat=103

[72] LumaSense Technologies, Table of emissivity parameters (retrieved: October 17th, 2017): http://www.automatika.rs/wp-content/uploads/2013/07/Emissivity-Table-of-various-Surfaces-for-Infrared-Thermometry.pdf

[73] Solaa, X., Ignatieva, M., Flamanta, G., Smurovb, I., and Konstantinovc, S. "Monitoring of melting and solid state phase transformation induced by pulsed laser action on pure zirconium." *Applied surface science* 109 (1997): 106-112.

[74] Schindel, B. "Thermographie in der Theorie und Praxis", 2007 (retrieved: October 17th, 2017): www.thermografie.co.at/files/ebs.pdf

[75] Bai, H., Xu, Y., Zhao, L., Li, C., and Shi, G. "Non-covalent functionalization of graphene sheets by sulfonated polyaniline." *Chemical Communications* 13 (2009): 1667-1669.

[76] Schmid, M. LEIS energy calculator. IAP/TU Wien Surface Physics Group, 2002-2013 (retrieved: October 17th, 2017): https://www.iap.tuwien.ac.at/www/surface/leis

[77] National Institute of Standards and Technology (NIST), XPS database https://srdata.nist.gov/xps/main_search_menu.aspx

[78] Vogel, D. *Local reaction kinetics of CO oxidation on heterogeneous platinum, palladium and palladium oxide surfaces*. Diss. Technische Universität Wien, Fakultät für Technische Chemie, 2012.

[79] Vogel, D., Budinska, Z., Spiel, C., Schlögl, R., and Suchorski, Y. "Silicon oxide surface segregation in CO oxidation on Pd: an in situ PEEM, MS and XPS study." *Catalysis letters* 143.3 (2013): 235-240.

[80] Seah, M. P., and Lea, C. "Surface segregation and its relation to grain boundary segregation." *Philosophical Magazine* 31.3 (1975): 627-645.

[81] White, C. L., Padgett, R. A., Liu, C. T., and Yalisove, S. M. "Surface and grain boundary segregation in relation to intergranular fracture: Boron and sulfur in Ni_3Al." *Scripta Metallurgica* 18.12 (1984): 1417-1420.

[82] Baker, T. N. "Role of zirconium in microalloyed steels: a review." *Materials Science and Technology* 31.3 (2015): 265-294.

[83] WebCrossSections – VUO. Atomic calculation of photoionization cross-sections and asymmetry parameters (retrieved: October 17th, 2017): https://vuo.elettra.eu/services/elements/WebElements.html

[84] Cocke, D. L., and Owens, M. S. "XPS evidence for facile formation of surface zirconium carbides from zirconium oxide overlayer decomposition and surface carbon." *Applied Surface Science* 31.4 (1988): 471-476.

[85] Schlich, H. (MaTecK GmbH). "Über die Möglichkeiten der Herkunft von Kohlenstoff-verunreinigungen in $Pt_3Zr(0001)$", telephone conversation, September 7th, 2017.